

## **Photovoltaic Power System**

# **Photovoltaic Power System**

Modeling, Design, and Control

*Weidong Xiao*

University of Sydney  
Australia

**WILEY**

This edition first published 2017  
© 2017 John Wiley & Sons Ltd

All rights reserved. No part of this publication may be reproduced, stored in a retrieval system, or transmitted, in any form or by any means, electronic, mechanical, photocopying, recording or otherwise, except as permitted by law. Advice on how to obtain permission to reuse material from this title is available at <http://www.wiley.com/go/permissions>.

The right of Weidong Xiao to be identified as the author of this work has been asserted in accordance with law.

*Registered Office(s)*

John Wiley & Sons, Inc., 111 River Street, Hoboken, NJ 07030, USA

John Wiley & Sons Ltd, The Atrium, Southern Gate, Chichester, West Sussex, PO19 8SQ, UK

*Editorial Office*

The Atrium, Southern Gate, Chichester, West Sussex, PO19 8SQ, UK

For details of our global editorial offices, customer services, and more information about Wiley products visit us at [www.wiley.com](http://www.wiley.com).

Wiley also publishes its books in a variety of electronic formats and by print-on-demand. Some content that appears in standard print versions of this book may not be available in other formats.

*Limit of Liability/Disclaimer of Warranty*

While the publisher and authors have used their best efforts in preparing this work, they make no representations or warranties with respect to the accuracy or completeness of the contents of this work and specifically disclaim all warranties, including without limitation any implied warranties of merchantability or fitness for a particular purpose. No warranty may be created or extended by sales representatives, written sales materials or promotional statements for this work. The fact that an organization, website, or product is referred to in this work as a citation and/or potential source of further information does not mean that the publisher and authors endorse the information or services the organization, website, or product may provide or recommendations it may make. This work is sold with the understanding that the publisher is not engaged in rendering professional services. The advice and strategies contained herein may not be suitable for your situation. You should consult with a specialist where appropriate. Further, readers should be aware that websites listed in this work may have changed or disappeared between when this work was written and when it is read. Neither the publisher nor authors shall be liable for any loss of profit or any other commercial damages, including but not limited to special, incidental, consequential, or other damages.

*Library of Congress Cataloging-in-Publication Data*

Names: Xiao, Weidong, 1969- author.

Title: Photovoltaic power system : modeling, design, and control / Weidong Xiao.

Description: Hoboken, NJ : John Wiley & Sons, 2017. | Includes bibliographical references and index.

Identifiers: LCCN 2016056659 (print) | LCCN 2017001056 (ebook) | ISBN 9781119280347 (cloth) | ISBN 9781119280361 (pdf) | ISBN 9781119280323 (epub)

Subjects: LCSH: Photovoltaic power systems.

Classification: LCC TK1087 .X56 2017 (print) | LCC TK1087 (ebook) | DDC 621.31/244–dc23

LC record available at <https://lccn.loc.gov/2016056659>

Cover Design: Wiley

Cover Images: (Background) © Alessandro2802/Gettyimages; (Circles: Top right corner to bottom left corner) © chapin31/Gettyimages; © PaulPaladin/Gettyimages; Courtesy of author; © Dwight Smith/Shutterstock

Set in 10/12pt WarnockPro by SPI Global, Chennai, India

*This book is dedicated to my son, William, and daughter, Emily, with deep love.*

## Contents

**Preface** *xiii*

**Acknowledgments** *xvii*

**About the companion website** *xix*

<b>1</b>	<b>Introduction</b>	<b>1</b>
1.1	Cell, Module, Panel, String, Subarray, and Array	2
1.2	Blocking Diode	5
1.3	Photovoltaic Cell Materials and Efficiency	6
1.4	Test Conditions	7
1.5	PV Module Test	8
1.6	PV Output Characteristics	9
1.7	PV Array Simulator	12
1.8	Power Interfaces	13
1.9	Standalone Systems	13
1.10	AC Grid-connected Systems	18
1.11	DC Grid and Microgrid Connections	19
1.12	Building-integrated Photovoltaics	21
1.13	Other Solar Power Systems	22
1.14	Sun Trackers	23
	Problems	24
	References	24
<b>2</b>	<b>Classification of Photovoltaic Power Systems</b>	<b>25</b>
2.1	Background	25
2.2	CMPPT Systems	26
2.2.1	Power Loss due to PV Array Mismatch	29
2.2.2	Communication and Data Acquisition for CMPPT Systems	32
2.3	DMPPT Systems at PV String Level	36
2.4	DMPPT Systems at PV Module Level	37
2.4.1	Module-integrated Parallel Inverters	37
2.4.2	Module-integrated Parallel Converters	39
2.4.3	Module-integrated Series Converters	40
2.4.4	Module-integrated Differential Power Processors	40
2.4.5	Module-integrated Series Inverters	41
2.5	DMPPT Systems at PV Submodule Level	42

2.5.1	Submodule-integrated Series Converters	42
2.5.2	Submodule-integrated Differential Power Processors	43
2.5.3	Isolated-port Differential Power Processors	44
2.6	DMPPT Systems at PV Cell Level	44
2.7	Summary	45
	Problems	46
	References	46
<b>3</b>	<b>Safety Standards, Guidance and Regulation</b>	<b>49</b>
3.1	Certification of PV Modules	49
3.2	Interconnection Standards	51
3.3	System Integration to Low-voltage Networks	55
3.3.1	Grounded Systems	55
3.3.2	DC Ground Fault Protection	56
3.3.3	Voltage Specification	56
3.3.4	Circuit Sizing and Current	58
3.3.5	Cable Selection	58
3.3.6	Connectors and Disconnects	59
3.3.7	Grid Interconnections through Power Distribution Panels	59
3.3.8	Marking	60
3.4	System Integration to Medium-voltage Network	60
3.4.1	Active Power Throttling	61
3.4.2	Fault Ride-through	61
3.4.3	Reactive Power Support	62
3.5	Summary	63
	Problems	63
	References	64
<b>4</b>	<b>PV Output Characteristics and Mathematical Models</b>	<b>65</b>
4.1	Ideal Single-diode Model	68
4.1.1	Product Specification	68
4.1.2	Parameter Identification at Standard Test Conditions	69
4.1.3	Variation with Irradiance and Temperature	71
4.2	Model Accuracy and Performance Indices	75
4.3	Simplified Single-diode Models	78
4.3.1	Parameter Identification: Part One	79
4.3.2	Parameter Identification: Part Two	81
4.3.3	Variation with Irradiance and Temperature	87
4.4	Model Selection from the Simplified Single-diode Models	88
4.5	Complete Single-diode Model	91
4.6	Model Aggregation and Terminal Output Configuration	92
4.7	Polynomial Curve Fitting	95
4.8	Summary	99
	Problems	100
	References	101

<b>5</b>	<b>Power Conditioning</b>	<i>103</i>
5.1	PV-side Converters	<i>104</i>
5.1.1	PV Module for Case Study	<i>105</i>
5.1.2	Buck Converter	<i>105</i>
5.1.3	Full-bridge Isolated Transformer DC/DC Converter	<i>110</i>
5.1.4	Boost Converter	<i>115</i>
5.1.5	Tapped-inductor Boost Topology	<i>119</i>
5.1.6	Buck-Boost Converter	<i>122</i>
5.1.7	Flyback Converter	<i>126</i>
5.2	Battery-side Converter for DC/DC Stage	<i>130</i>
5.2.1	Introduction to Dual Active Bridges	<i>130</i>
5.2.2	Discharge Operation	<i>131</i>
5.2.3	Charging Operation	<i>135</i>
5.2.4	Zero Voltage Switching	<i>139</i>
5.3	DC Link	<i>142</i>
5.3.1	DC Link for Single-phase Grid Interconnection	<i>143</i>
5.3.2	DC Link for Three-phase Grid Interconnections	<i>145</i>
5.4	Grid-side Converter for DC/AC Stage	<i>147</i>
5.4.1	DC to Single-phase AC Grid	<i>147</i>
5.4.2	DC to Three-phase AC Grid	<i>151</i>
5.4.3	Reactive Power	<i>153</i>
5.5	Grid Link	<i>154</i>
5.5.1	L-type for Single-phase Grid Connections	<i>154</i>
5.5.2	L-type for Three-phase Grid Interconnections	<i>155</i>
5.5.3	LCL-type Filters	<i>157</i>
5.5.4	LC-type Filters	<i>160</i>
5.6	Loss Analysis	<i>160</i>
5.6.1	Conduction Loss	<i>161</i>
5.6.2	High-frequency Loss	<i>163</i>
5.7	Conversion Efficiency	<i>165</i>
5.8	Wide Band-gap Devices for Future Power Conversion	<i>165</i>
5.9	Summary	<i>167</i>
	Problems	<i>169</i>
	References	<i>171</i>
<b>6</b>	<b>Dynamic Modeling</b>	<i>173</i>
6.1	State-space Averaging	<i>173</i>
6.2	Linearization	<i>174</i>
6.3	Dynamics of PV Link	<i>175</i>
6.3.1	Linearization of PV Output Characteristics	<i>175</i>
6.3.2	Buck Converter as the PV-link Power Interface	<i>176</i>
6.3.3	Full-bridge Transformer Isolated DC/DC as the PV-link Power Interface	<i>180</i>
6.3.4	Boost Converter as the PV-link Power Interface	<i>182</i>

6.3.5	Tapped-inductor Topology as the PV-link Power Interface	184
6.3.6	Buck-boost Converter as the PV-link Power Interface	186
6.3.7	Flyback Converter as the PV-link power Interface	188
6.4	Dynamics of DC Bus Voltage Interfaced with Dual Active Bridge	189
6.5	Dynamics of DC Link for AC Grid Connection	192
6.5.1	Single-phase Connection	192
6.5.2	Three-phase Connection	194
6.6	Summary	195
	Problems	196
	References	197
<b>7</b>	<b>Voltage Regulation</b>	199
7.1	Structure of Voltage Regulation in Grid-connected PV Systems	199
7.2	Affine Parameterization	201
7.3	PID-type Controllers	202
7.4	Desired Performance in Closed Loop	205
7.5	Relative Stability	206
7.6	Robustness	208
7.7	Feedforward Control	209
7.8	Voltage Regulation in PV Links	210
7.8.1	Boost Converter for PV Links	210
7.8.2	Tapped-inductor Topology for PV Links	213
7.8.3	Buck Converter as the PV-link Power Interface	214
7.8.4	Buck-boost Converter as the PV-link Power Interface	216
7.8.5	Flyback Converter as the PV-link Converter	218
7.9	Bus Voltage Regulation for DC Microgrids	220
7.10	DC-link Voltage Regulation for AC Grid Interconnections	221
7.10.1	Single-phase Grid Interconnection	222
7.10.2	Three-phase Grid Interconnection	226
7.11	Sensor, Transducer, and Signal Conditioning	227
7.12	Anti-windup	230
7.13	Digital Control	236
7.13.1	Continuous Time and Discrete Time	240
7.13.2	Digital Redesign	240
7.13.3	Time Delay due to Digital Conversion and Process	243
7.14	Summary	245
	Problems	246
	References	247
<b>8</b>	<b>Maximum Power Point Tracking</b>	249
8.1	Background	249
8.2	Heuristic Search	252
8.3	Extreme-value Searching	255
8.4	Sampling Frequency and Perturbation Size	257
8.5	Case Study	258
8.6	Start-stop Mechanism for HC-based MPPT	261
8.7	Adaptive Step Size Based on the Steepest Descent	264

8.8	Centered Differentiation	267
8.9	Real-time System Identification	270
8.9.1	Recursive Least Squares Method	270
8.9.2	Newton–Raphson Method for MPP Determination	272
8.9.3	Forgetting Factor	272
8.10	Extremum Seeking	273
8.11	Multiple Power Peaks and Global MPPT	276
8.12	Performance Evaluation of MPPT	277
8.12.1	Review of Indoor Test Environment	277
8.12.2	Review of Outdoor Test Environments	278
8.12.3	Recommended Test Benches for MPPT Evaluation	279
8.12.4	Statistical Paired Differential Evaluation	280
8.13	Summary	281
	Problems	283
	References	284
<b>9</b>	<b>Battery Storage and Standalone System Design</b>	<b>285</b>
9.1	Batteries	287
9.1.1	Battery Types	288
9.1.2	Battery Terminology	291
9.1.3	Charging Methods	292
9.1.4	Battery Mismatches and Balancing Methods	295
9.1.5	Battery Characteristics and Modeling	300
9.1.6	Battery Selection	308
9.2	Integrating Battery-charge Control with MPPT	308
9.3	Design of Standalone PV Systems	309
9.3.1	Systems without Significant Energy Storage	309
9.3.2	Systems with Significant Energy Storage	311
9.4	Equivalent Circuit for Simulation and Case Study	316
9.5	Simulation Model to Integrate Battery-charging with MPPT	317
9.6	Simulation Study of Standalone Systems	318
9.6.1	Simulation of PV Array	318
9.6.2	Short-term Simulation	319
9.6.3	Medium-term Simulation	321
9.6.4	Long-term Simulations	325
9.6.5	Very-long-term Simulations	328
9.7	Summary	329
	Problems	331
	References	332
<b>10</b>	<b>System Design and Integration of Grid-connected Systems</b>	<b>333</b>
10.1	System Integration of Single-phase Grid-connected System	335
10.1.1	Distributed Maximum Power Point Tracking at String Level	335
10.1.2	Distributed Maximum Power Point Tracking at PV Module Level	337
10.2	Design Example of Three-phase Grid-connected System	340
10.3	System Simulation and Concept Proof	343
10.3.1	Modeling and Simulation of PV String	344

10.3.2	Modeling and Simulation of DC/DC Stage	345
10.3.3	Modeling and Simulation of DC/AC Stage	349
10.3.4	Overall System Integration and Simulation	351
10.4	Simulation Efficiency for Conventional Grid-connected PV Systems	351
10.4.1	Averaging Technique for Switching-mode Converters	353
10.4.2	Overall System Integration and Simulation	354
10.4.3	Long-term Simulation	357
10.5	Grid-connected System Simulation Based on Module Integrated Parallel Inverters	359
10.5.1	Averaged Model for Module-integrated Parallel Inverters	359
10.5.2	Overall System Integration and Simulation	362
10.6	Summary	365
	Problems	366
	References	366
	<b>Index</b>	<b>367</b>

## Preface

Photovoltaic (PV) power engineering has attracted significant attention in recent years. This book sets out to fulfil an important need in academia and industry for a comprehensive resource covering modeling, design, simulation, and control of PV power systems. Initially developed to support teaching senior-undergraduate and graduate courses, the work also covers practical design issues, that make it useful for industry practitioners seeking to master the subject through self-study and training. The book provides a smooth transition from fundamental knowledge to advanced subjects of interest to academics and to those working on system improvements in industry. A fundamental knowledge of power electronics and linear control theory is required to benefit fully from this book.

This comprehensive treatment covers fundamental and advanced subjects in technologies, power electronics, and control engineering for PV power systems. Throughout, the description of PV power systems follows a clear framework for each section.

The book is divided into ten chapters. The interrelationship of the chapters is illustrated in Figure 1. The step-by-step introduction of the individual system components and controls for PV power systems is covered in Chapters 4–8. With the support of the system classification and the safety guidelines, which are discussed in Chapters 2 and 3, respectively, the overall system integrations for standalone systems and grid-tied systems are set out in Chapters 9 and 10.

Chapter 1 provides a brief introduction to solar power systems. This includes the clarification of vocabulary which proves integral to the remainder of the book.

Chapters 2 and 3 provide comprehensive classifications of PV power system configurations, in particular grid-tied systems, approached according to the level at which the MPPT is applied, MPPT techniques, power-conditioning topologies, and technologies for battery balancing. The reader is assisted, using clear definitions, to develop an understanding of the latest systems and directions of research and development, which later informs research directions for PV power systems. Reader understanding of relevant safety standards, guidance, and regulations is developed to prevent researchers deviating from standard practice in industry. A system of reference is provided for safe practice in engineering and design. Though the codes and guidelines cited are implemented in the USA and Europe, they are universally applicable and allow all readers to practice PV power engineering in a safe manner. These chapters also cover the certification of PV modules, the safety standards of power interfaces, the system requirements for grid interconnection, and the important means of protection. The main conversion units are the PV-side converters, battery-side converters, and grid-side converters. The

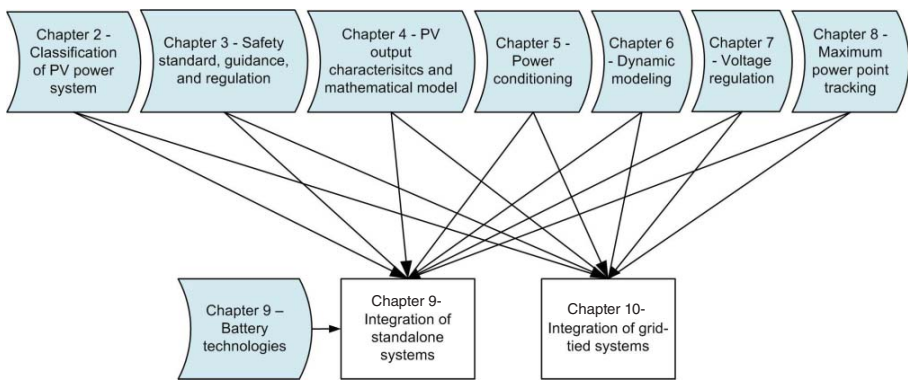


Figure 1 Organization and interconnection of Chapters 2 to 10.

interconnection of the conversion units are the PV link, DC link, and grid link. The PV generation section is divided into the PV source circuits and PV output circuits. Two types of modeling are demonstrated for the reader. Firstly, simulation models that represent a practical system and prove the design concept are discussed in Chapters 4 and 5. Secondly, mathematical models are developed to illustrate the system dynamics used for controller synthesis. Model development and verification are covered in Chapter 6.

Chapter 4 discusses PV output characteristics and mathematical models for simulation and analysis. It builds upon an understanding of PV product datasheets and provides a straightforward approach to building a mathematical model for simulation purposes. When model accuracy becomes the priority, an advanced approach is also provided. The tradeoff between model simplicity and accuracy is extensively considered, discussed, and demonstrated by practical examples.

Chapter 5 provides the information necessary to specify, design, simulate, and evaluate power-conditioning circuits and accessories for PV power applications. The main conversion units are PV-side converters, battery-side converters, and grid-side converters. The important interconnections are the PV link, DC link, and grid link. The description provided comprehensively covers application to all PV power systems. The chapter covers system design, steady-state analysis, and simulation verification. Current modulation for AC grid interconnection is introduced and simulated for design verification. This book places emphasis on computer-aided analysis, design, and evaluation. For universality, all included simulation models are built using the fundamental blocks of Simulink. The analysis reveals the fundamental system dynamics for the purpose of both time-domain simulation and control synthesis. Although provided with software such as Simscape Power Systems, written for power electronics and power systems, this is not used due to the aim to demonstrate the simulation principle and focus on fundamental implementations instead. The control system design, analysis and evaluations are based on the functions of Matlab and Matlab version R2010b. Simulink is used to demonstrate all simulation cases; the same or higher versions of this software can be used to duplicate simulation results or develop results further. Most chapters present practical examples in order to demonstrate designs and verify them, which are presented in case studies. Photographs, diagrams, flowcharts, graphs, equations, and tables are included to provide clear explanations of technical subject matter. Readers can then duplicate results through computer-aided design and analysis, leading to the development and evaluation of new systems.

Chapter 6 focuses on dynamic modeling of PV power systems. The mathematical modeling starts with the state-space averaging, followed by linearization. Dynamic models are developed for the voltage signals at the PV and DC links and the variety of converter topologies is also considered. The dynamics of the developed mathematical models are verified through simulation and comparison. One section is given over to modeling the dynamics of dual active bridges when used as the battery power interface.

Chapter 7 concerns the application of linear control theory. The chapter discusses evaluations of relative stability and system robustness. Voltage regulation for the PV and DC links is introduced and analyzed in depth. Examples and simulations are used to demonstrate the effectiveness of proposed approaches and methodology. Based on the system model, advanced control techniques, such as Affine parameterization, anti-windup, and feedforward implementation, are introduced. The implementation of sensing and digital control is briefly discussed at the end of the chapter.

Chapter 8 focuses on MPPT, which is important and unique to PV power systems. A comprehensive overview is provided, and MPPT algorithms are classified and discussed. The chapter introduces a simple algorithm and develops to consider advanced techniques to improve tracking performance. The simulation and implementation of MPPT techniques are also discussed in this chapter.

Chapter 9 discusses the integration of standalone PV power systems. The chapter enables readers to understand the latest progress and choose suitable battery types for standalone applications through the introduction and comparison of battery characteristics. This proceeds onto a discussion of battery characteristics and models and how they relate to system design and analysis. A new classification is proposed to avoid confusion seen in the earlier literature and provide a clear framework for understanding the methodologies used for battery balancing. A method to integrate the MPPT function with the battery cycle charge is proposed. Examples are given to demonstrate the effectiveness of modeling, design, control, and simulation. Simulation models for the controller and power interface are developed at different levels: short term, medium term, long term, and very long term. A simulation of eight-hour system operation is created, demonstrating the state of MPPT, battery voltage regulation, and variation of state of charge corresponding to solar irradiance and cell temperature.

The final chapter, Chapter 10, addresses the integration of grid-tied PV power systems, including two small-scale single-phase interconnections and one utility-level three-phase system. Examples are given demonstrating the effectiveness of the design, integration, control, and simulation with additional consideration for safety protection. The simulation study is divided into two parts: a short-term simulation that aims to capture the fast transient response of switching dynamics and grid disturbances, and a long-term simulation that illustrates the system operation in response to environmental conditions.

## Technical Support

One advantage of this book is that all modeling and simulation for the case studies is based on the basic functions of Simulink and Matlab. The modeling and simulation approach is based on system dynamics, which helps readers to understand the fundamental principle behind various simulation tools. The construction of output models, power interfaces and control, and standalone and grid-tied systems are illustrated in detail. Version R2010b or higher of Matlab and Simulink can be used to duplicate the results or to develop new studies. Other software tools are unnecessary.

University of Sydney  
Australia

Weidong Xiao

# 1

## Introduction

The photovoltaic (PV) effect is the generation of DC electricity from light. Alexandre Edmond Becquerel, a French experimental physicist, discovered the effect in 1839. More recently, scientists have discovered that certain materials, such as silicon, can produce a strong PV effect. In the 1950s, Bell Labs of the USA produced PV cells for space activities. This can be considered as the beginning of the PV power industry. The high cost of PV materials mostly prevented applications elsewhere.

Over the past 20 years, the PV power industry has experienced significant growth. PV power generation has become more and more common. The capacity of PV systems ranges from milliwatts for portable devices such as calculators, to gigawatts for power plants connected to the electricity grid. A grid-connected PV power system can be economically installed, and can be rated as low as just a few hundred watts. The advantages of PV power systems that have led to their rapid growth are:

- green, renewable
- reliability and long lifetime
- advanced manufacturing process
- static, so noise-free operations
- improving efficiency
- decreasing prices
- flexibility of construction
- highly modular nature
- availability of government support and incentives.

Using the latest technologies, the manufacturing of crystalline-based PV cells consumes significant amounts of energy, which prevents further cost reductions. The levelized cost of electricity generated using solar PVs is still high in comparison with conventional generation resources, such as coal, natural gas, and wind, according to a technical report published by the US Department of Energy's National Renewable Energy Laboratory (Stark et al. 2015). The report was based on a study of the USA, Germany, and China. Several large-scale PV power systems were announced in 2016 and projected significantly lower costs, but these must be treated as special cases. The project feasibility and system reliability need to be carefully evaluated until the projects are successfully delivered. It is clear that the price of PV products mostly reflects their quality and reliability. High-quality, certified PV products are usually more expensive than non-certified ones. It is unrealistic to judge a PV power system only on the installation cost since reliable and long-lifetime operations are always expected.

**Table 1.1** Price schedule of feed-in tariffs in Ontario, Canada.

Type	System capacity (kW)	Price (\$/kWh)*
Rooftop	$\leq 10$	0.294
	10–100	0.242
	100–500	0.225
Non-rooftop	$\leq 10$	0.214
	10–500	0.209

\*Canadian dollars.

The feed-in tariff (FIT) is the major driver of the boom in PV power all over the world. The regulatory incentives are different from country to country, but all are designed to accelerate investment in PV-related technologies. One FIT example can be found on the website of the Ontario Power Authority, Canada. Parts of the FIT price schedule are shown in Table 1.1, which covers projects under 500 kW in capacity. It shows that the government contributes significant funds for PV system installations since the listed price is higher than the charge for residential consumption. It should be noted that the listed price is based on the 2016 schedule. Like FITs in most other countries, it is always subject to change. Another disadvantage of PV power systems lies in their low power density, which limits their use mainly to static applications rather than vehicles. Motor vehicles are usually considered as one of the major contributors to air pollution.

## 1.1 Cell, Module, Panel, String, Subarray, and Array

A PV cell, also commonly called a solar cell, is the fundamental component of a PV power system. A crystalline-based solar cell features a p-n junction, as shown in Figure 1.1. The manufacturing process includes melting, doping, metallization and texturing. The positive and negative sides of the junction form the DC voltage and supply electricity when a load is connected. However, the voltage of a single p-n junction cell is less than 1 V, which is low for most practical applications. Moreover, it is mechanically fragile, and must be laminated and protected for practical use.

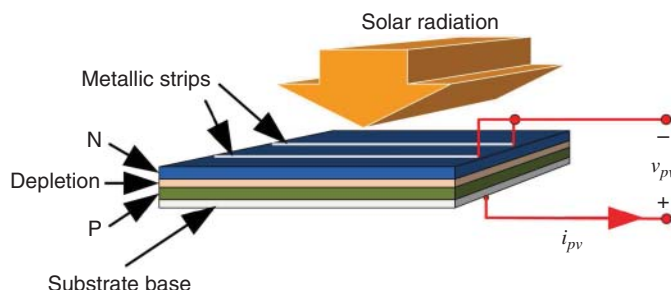


**Figure 1.1** Typical crystalline PV cell construction.

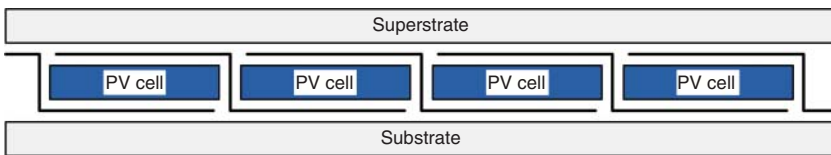


**Figure 1.2** Lamination of PV module.

To end users, the basic unit is the PV module or solar panel, which can produce higher voltages and more power than a single cell. A PV module consists of cells that are interconnected and laminated together. The old PV panel was usually designed to match the nominal voltage of batteries, since standalone systems were the beginning of the PV industry. For example, traditional 36-cell PV modules used to be popular for direct charging of batteries with a nominal voltage of 12 V. Nowadays, with the increasing numbers of grid-connected systems and the advances in power-conditioning devices, the number of cells in each PV module is no longer limited to matching the nominal voltages of batteries or loads. The manufacturers are more concerned with cost-effective solutions and supply all different sizes of solar panels: usually incorporating 48, 54, 60, or 72 cells. Solar cables and connectors are usually integrated with the module for straightforward interconnection and installation.

To form a PV panel, crystalline-based PV cells are sandwiched by the superstrate and substrate for protection, as illustrated in Figure 1.2. Tempered glass is commonly used as the superstrate, supporting the module lamination and protecting the fragile cells. Glass also has the same ratio of thermal expansion as a crystalline PV cell, since both are made of silicon. Furthermore, tempered glass is strong and has good transparency, with about 94% light transmission. The glass surface is also textured to reduce light reflections. Metal conductors connect the PV cells from the surface to the bottom for series interconnection. The cells are also protected by an encapsulant, which is a material that surrounds the PV cells between the superstrate and substrate.

Figure 1.3 shows a standard PV module and its internal electrical configuration. It consists of 72 cells in series connection. The cells are divided into three groups, which are termed the submodules. Each submodule includes one bypass diode in parallel connection with 24 interconnected solar cells. The bypass diodes are standard components that are integrated in the crystalline-based PV module. The implementation prevents the destructive effects of hot spots, should there be unbalanced generation among the series-connected cells. The overall electrical connection is configured inside the junction box, which is commonly located at the back of the PV panel. The output cable always indicates the polarity of the positive and negative terminals.

Attention should be given to AC PV modules, often simply called AC modules. Just the same as standard PV modules, an AC module is an environmentally protected unit consisting of interconnected solar cells, junction box, superstrate, substrate, electrical interconnections, and other lamination components. However, the module includes an inverter inside the junction box to produce AC power at the output terminal. The concept of an AC module is the same as the microinverter solution, which converts DC to AC at the PV module level. However, the difference is that the microinverter is an independent unit that is electrically connected to the PV module instead of being fully integrated. Microinverters belong to the class of module-integrated parallel inverters (MIPIs), which will be discussed in Section 2.4.1.

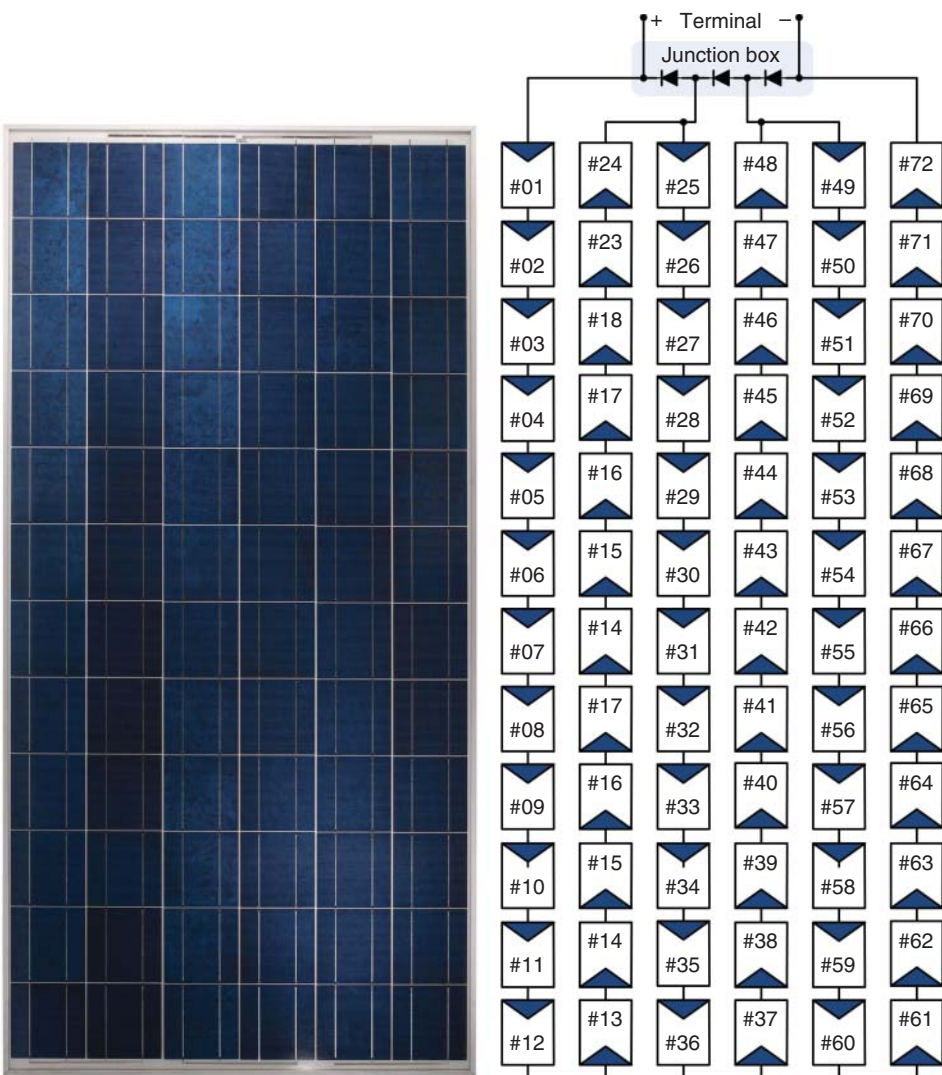


**Figure 1.3** 72-cell PV module: left, appearance; right, configuration.

It is very important to use the correct terms to describe PV generators: cell, module, panel, string, subarray, and array. Figure 1.4 illustrates how the power capacity is built up from cell level to array level. PV power systems are commonly assembled by configuration of PV modules in series and/or in parallel. The series connection of solar modules in order to stack up the output voltage is commonly referred to as a “string.” The parallel connections of PV strings forms an array, in which the power capacity can be built up to the levels of hundreds, thousands, or even millions of watts. In large-scale PV power systems, an array is divided into multiple subarrays.

A PV array can be monopolar or bipolar. A monopolar array or subarray is a typical DC circuit that has two conductors in the output circuit, with positive (+)

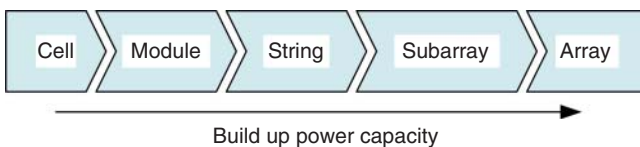
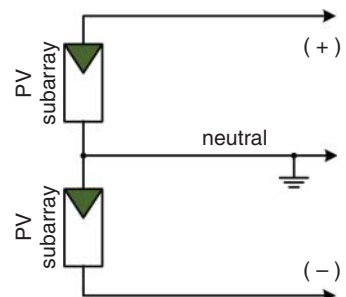


**Figure 1.4** PV power capacity built from cell to array.

**Figure 1.5** Bipolar PV array formed from two monopolar subarrays.



and negative (−) polarities. A bipolar PV array includes a neutral point, as shown in Figure 1.5, and is formed from two monopolar subarrays. Ideally, the two monopolar subarrays should be identical in power and voltage levels. The neutral point is grounded at a central point in the interconnected system. A company called AE Solar Energy used to be the major producer of utility-interaction inverters, which were designed for the bipolar array configuration and large-scale PV power systems. The inverter accommodates the output of the bipolar PV array and is rated at up to  $\pm 600$  V.

## 1.2 Blocking Diode

PV components are direct current sources, so the reverse flow of current into the PV source circuit should be prevented. Blocking diodes can be used, installed in series with the PV output string in order to block reverse currents. They are often referred to as “string diodes.” To distinguish them from the bypass diode, Figure 1.6 illustrates a typical PV source circuit with the integration of both bypass and blocking diodes, denoted  $D_{bp}$  and  $D_{bl}$ , respectively. The bypass diodes are standard components that are commonly integrated inside the junction boxes of PV modules, as shown in Figure 1.3. The blocking diodes are parts of the overall PV source circuit, as shown in Figure 1.6, and are optionally implemented when required.

Blocking diodes have been widely used for direct battery-charging applications due to their advantages of effectiveness, safety, reliability, and because they are maintenance-free. However, their disadvantage is a forward voltage drop that results in significant power losses in the PV source circuit. For example, the forward voltage of a typical 600-V/12-A rated diode is about 1 V. Considering that the PV string current is 7 A, each blocking diode introduces about 7 W of conduction loss, which generates heat and creates a hot spot. Furthermore, the failure of a blocking diode will cause a complete loss of the protection function and might lead to the failure of the entire string. The latest PV systems are developed for high efficiency and tend to avoid use of blocking diodes. Since all PV modules show a certain level of tolerance of reverse

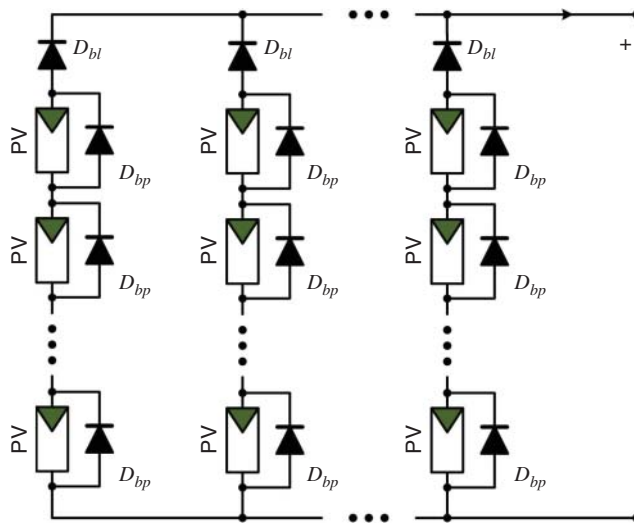


**Figure 1.6** PV circuit with bypass diodes and blocking diodes.

current, manufacturers always provide the upper limit of reverse current that causes no damage to the PV product. Fuses and DC circuit breakers have been recently used in series connection with the individual PV string in order to protect the circuit and stop reverse current up to the maximum limit. The power losses are significantly lower than those caused by blocking diodes.

### 1.3 Photovoltaic Cell Materials and Efficiency

The PV effect can happen in many materials that absorb light and turn a portion of the energy into electricity. Solar cells are made of materials that are designed and formulated to produce strong PV effect. This can be measured by the conversion efficiency of the irradiance to electrical power. If a solar cell is claimed as being 15% efficient, it indicates that the electric power output of a  $1 \text{ m}^2$  cell receiving  $1000 \text{ W/m}^2$  irradiance at  $25^\circ\text{C}$  would be 150 W. Common PV cells are made of mono-crystalline silicon, multi-crystalline silicon, thin films, organic materials, and so on. It should be noted that mono-crystalline and multi-crystalline silicon are also referred to as single-crystalline and poly-crystalline silicon. The crystal growth process during manufacture is behind the formation of the two different types of crystalline-based solar cells. The Czochralski and Siemens processes are commonly used for making PV materials. The process followed includes doping, metallization, and texturing in order to construct solar cells.

The counterparts of crystalline silicon cells are thin-film cells. The common ones are summarized in Table 1.2. One of the most successful companies in the thin-film PV industry is First Solar, which uses cadmium telluride ( $\text{CdTe}$ ) technologies. Even though the efficiency of  $\text{CdTe}$ -based products is generally lower than that of crystalline silicon cells, the technology has significantly lower material and manufacturing costs.

Organic solar cells are made of thin layers of organic materials. These technologies are under development and are rarely applicable for high power systems.

**Table 1.2** Common PV materials.

Composition	Acronym
Mono-crystalline silicon or single-crystalline silicon	Mono-c-Si
Multi-crystalline silicon or poly-crystalline silicon	Poly-c-Si
Cadmium telluride	CdTe
Copper indium gallium selenide	CIGS
Amorphous silicon	a-Si

The efficiency of single junction cells is usually lower than 20% due to physical limits and technical constraints. Multi-junction cells have been invented in order to increase conversion efficiency. These are made up of multiple p-n junctions, which allows absorption of multiple light wavelengths through multiple layers. Efficiencies of over 30% have been reported. Their high price limits their application to aerospace or concentrated PV (CPV) systems, where high power density is particularly desirable. CPV is a technology that focuses sunlight using lenses or mirrors. The implementation minimizes the usage of PV material, which was significantly more expensive 20 years ago. The solar concentration ratio is commonly measured as the number of “suns,” where the one-sun condition represents non-concentrated light. With the decreasing cost of PV materials, CPV is no longer as attractive as previously. Due to the specialist nature of multi-junction cells and CPV, the technology will not be further discussed in this book.

## 1.4 Test Conditions

Photovoltaics are inherently an intermittent energy resource since the electricity production depends on the instantaneous environmental conditions. The output power not only stops at night, but also varies significantly through the day and the season. As an example, Figure 1.7 shows a PV panel's power output, as measured in Vancouver, Canada. Broken clouds caused dramatic variations in the PV power output over the first 2.5 h. The output became significantly low during the last 40 min due to cloud coverage. Therefore, the intermittent nature of PV power production should be always considered when planning either standalone or grid-connected PV power systems.

The irradiance is the density of radiation incident on a given surface. It is usually expressed in units of watts per square meter ( $\text{W}/\text{m}^2$ ). The PV cell temperature also plays an important role in determining the output. Defined in IEC 60904, the standard test conditions (STC) correspond to a solar irradiance of  $1000 \text{ W}/\text{m}^2$ , a device temperature of  $25^\circ\text{C}$ , with a reference solar spectral irradiance of air mass 1.5 (AM1.5). The standard is commonly applied to evaluate power capacities and conversion efficiencies of PV cells or modules. The rating of PV power systems is usually based on the accumulation of the PV module capacity at STC. The International Electrotechnical Commission (IEC) is the international standards and conformity assessment body for all fields of electrotechnology. The standards relevant to PV products will be discussed in Chapter 3.

According to IEC 61215, PV performance can also be measured at the nominal operating cell temperature (NOCT), which is defined as the equilibrium mean of solar cell

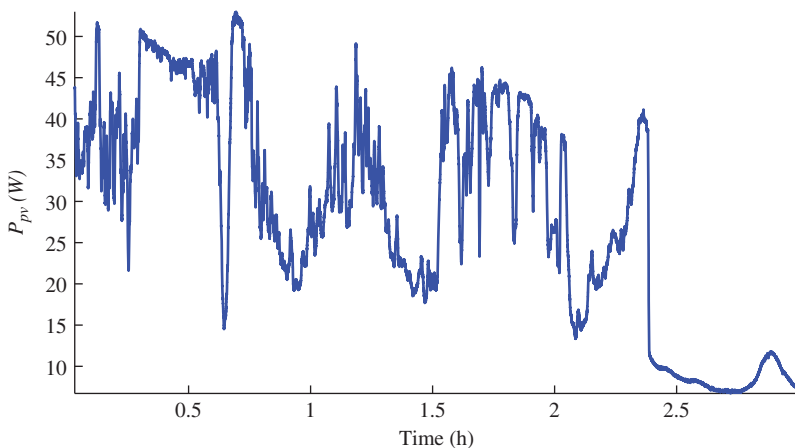


**Figure 1.7** PV module 3-h output, as measured on 16 June 2006.

**Table 1.3** SRE for measurement of NOCT.

Term	Value
Tilt angle	45° from the horizontal
Total irradiance	800 W/m <sup>2</sup>
Ambient temperature	45°C
Wind speed	1 ms <sup>-1</sup>

junction temperature within an open-rack mounted module in the standard reference environment (SRE), as shown in Table 1.3. Measured at STC and/or NOCT, the values of open-circuit voltage, short-circuit current, and power output of PV cells or modules define the product specifications and performance indices.

It is sometimes confusing to distinguish the terms of solar irradiance, insolation, and radiation, since all are used to describe the sunlight strength. Solar radiation is a general term that refers to the electromagnetic nature of sunlight, which is the radiant energy emitted from the sun. The total radiation on a surface includes the direct radiation from the sun, radiation diffused by the atmosphere, and radiation reflected by other objects. Insolation represents the quantity of solar radiation energy received on a surface of a certain size during a certain amount of time. The units can be kWh/m<sup>2</sup> or Wh/m<sup>2</sup>. The strength of radiation is commonly measured by the level of irradiance, of which the unit is kW/m<sup>2</sup> or W/m<sup>2</sup>. The term “irradiance” is the instant measure of light density, and will be used in the rest of this book.

## 1.5 PV Module Test

PV products are usually tested indoors using simulated resources since the outdoor environment is generally hard to control. A fully controlled environment can provide the



**Figure 1.8** Laboratory for PV module testing.

standard test conditions, variable irradiance levels, and regulated ambient temperatures. Calibration is also easier indoors than outdoors. A laboratory system for PV module testing is shown in Figure 1.8. It has a dark chamber, a solar simulator, a computer, and a measurement system. The system is located in the Masdar Institute of Science and Technology, Abu Dhabi, UAE.

The dark chamber is designed to mount the light box and PV module for testing. The inside temperature of the dark chamber can be set at a desired level. The solar simulator is a controllable light source that mimics sunlight, with the same or a very similar spectrum, and can be regulated to give different irradiance levels. The laboratory setup can be calibrated for STC with the reference of AM1.5. The light is usually pulsed over a short period to avoid the significant temperature rises that are commonly caused by long-term light exposures. The measurement system includes an electronic load that can be controlled to trace the output (open circuit or short circuit). A high-speed data acquisition system is also included to record data from the PV module output.

## 1.6 PV Output Characteristics

The output characteristics of PV cells or modules are commonly represented by the current–voltage ( $I$ – $V$ ) and power–voltage ( $P$ – $V$ ) curves. In some special cases, the voltage–current ( $V$ – $I$ ) and power–current ( $P$ – $I$ ) curves are also used to represent the PV output characteristics. Generally, they are transferable from one to another. Figure 1.9 shows typical  $I$ – $V$  and  $P$ – $V$  curves for a PV cell output. The normalized curves can also be used to represent the outputs of PV modules, strings, and arrays when all the solar cells are tested under uniform conditions. The curves show the three important points and four important values, as described in Table 1.4. The data are usually presented for STC, which is considered as the nominal rating.

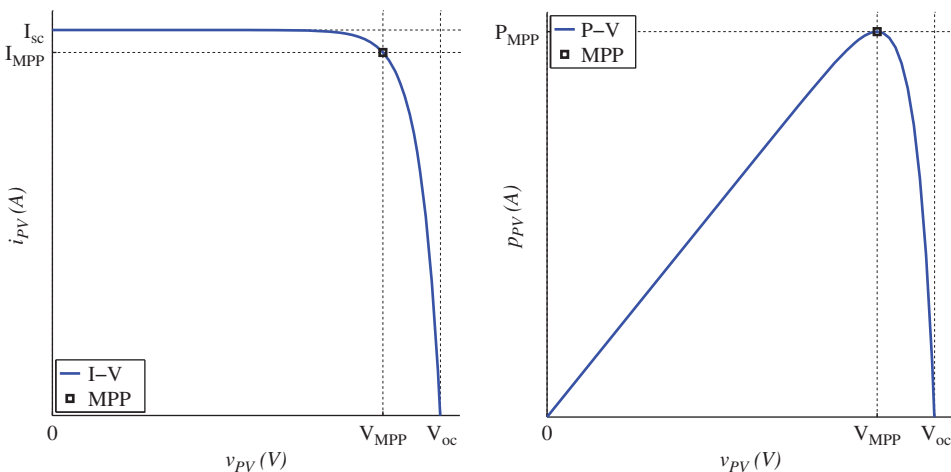


**Figure 1.9** PV output characteristics: left, normalized I–V curve; right, normalized P–V curve.

**Table 1.4** Four important values representing PV output characteristics.

Symbol	Description
$V_{OC}$	The open-circuit voltage, measured when the PV output terminal is open-circuit showing zero current.
$I_{SC}$	The short-circuit current, measured when the PV generator terminal is short-circuited.
$I_{MPP}$	The current measured at the MPP.
$V_{MPP}$	The voltage at the MPP.

The  $P_{MPP}$  is the highest power level for a certain environmental condition, and is calculated as  $P_{MPP} = V_{MPP} \times I_{MPP}$ .

The P–V curve clearly shows the maximum power point (MPP), which represents the highest power output ( $P_{MPP}$ ) that the PV generator can produce under certain environmental conditions. The MPP is located in the “knee” area of the I–V curve, and is represented by the current ( $I_{MPP}$ ) and voltage ( $V_{MPP}$ ), as shown in Figure 1.9. The open-circuit voltage,  $V_{OC}$  is the highest voltage level of the PV generator under a given test condition. The short-circuit current,  $I_{SC}$ , is the highest current level of the PV generator under the test condition. The power output is zero at either open-circuit or short-circuit conditions.

It is usually safe to connect PV generator terminals in short circuit since the output current is always limited by the short-circuit level, which depends on the instantaneous environmental conditions, particularly the irradiance. Short circuits can be used for safety protection when any electrical shock happens. It should be noted that the values of  $V_{OC}$ ,  $I_{SC}$ ,  $I_{MPP}$ , and  $V_{MPP}$  vary with environmental conditions. As a result, maximum

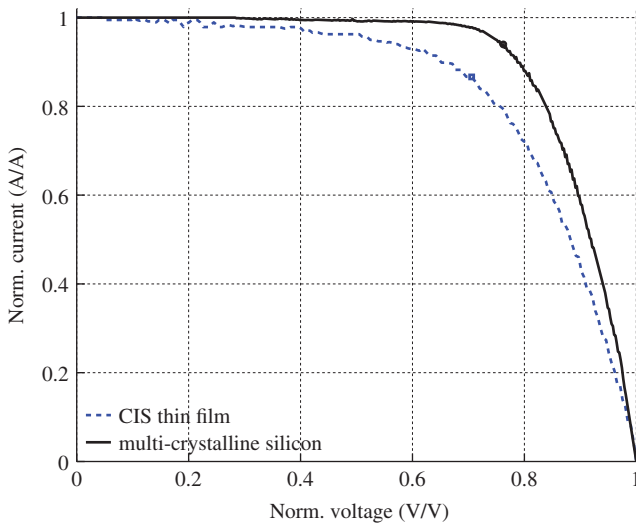


**Figure 1.10** Normalized I-V curve to represent the PV generator outputs and the difference in fill factor. CIS, copper indium diselenide.

power point tracking (MPPT) is required to locate the instantaneous MPP depending on the solar irradiance, cell temperature, or other uncertainties.

The shape of the I-V and P-V curves also depends on the cell technology and manufacturing process used. Figure 1.10 shows the measured I-V curves from two different PV modules: models ST10 and BP350, made of copper indium diselenide and multi-crystalline materials, respectively. The I-V curve of the ST10 model looks gentler than that of the BP350. The ratios of MPP voltages are 71.59% and 76.24% of the open-circuit voltage for the ST10 and BP350 respectively. The MPP currents are 86.63% and 93.96% of the short-circuit currents, for the ST10 and BP350, respectively.

The fill factor (FF) is a term that is used to describe the shape of the PV output. Its value is calculated as:

$$FF = \frac{I_{MPP} \times V_{MPP}}{I_{SC} \times V_{OC}} \quad (1.1)$$

The FF has been used as an indicator in PV material research since the ideal PV cell has a rectangular shaped I-V curve, with  $FF = 1$ . PV material research has tried to push achievable FF values higher, but it is not a significant measure for practical PV power applications since the performance of PV cells is evaluated on many other measures too, such as cost effectiveness and reliability. The FF values of crystalline-based PV cells are generally higher than those of thin-film devices.

The FF should be considered when optimizing the MPPT parameters since it corresponds to the difference in the PV output curves. The values of FF for the ST10 and BP350 modules are 0.62 and 0.66, respectively. It should be noted that the value of FF depends on the testing conditions: irradiance and temperature and so on. For a fair comparison among various PV materials, the FF values should be evaluated at STC.

## 1.7 PV Array Simulator

Outdoor evaluation of PV systems enables behavior of real PV arrays to be examined in natural sunlight. However, the outdoor environment is commonly considered difficult because the solar irradiance and ambient temperature are not controllable (Xiao et al. 2013). To perform a fair comparison of PV systems, simulators are commonly used.

Researchers tend to use controllable light and power sources to simulate the sunlight and PV generator outputs, respectively. A PV array simulator is a DC power supply, the output of which mimics PV output characteristics. It should not be confused with a solar or sun simulator, which is the artificial light source that was introduced in Section 1.5. It is common to use solar simulators to test PV outputs at the cell and module levels, but they are impractical at string and array levels.

The PV array simulator can be used for indoor testing of power interfaces developed for PV applications. The output is programmable, to give specific values of the open-circuit voltage, short-circuit current, the MPP, and the corresponding I–V curves. The level of solar irradiance and the cell temperature can also be predefined and programmed to simulate environmental variations.

PV array simulators have been developed in the kilowatt power range for simulating PV strings and arrays. Examples include the products manufactured by Chroma ATE Inc. Others are only at the hundreds-of-watts level, and are used to simulate the output of PV modules. One popular set of models is the E4350 and E4360 series produced by Agilent Technologies. An E4350B model is shown in Figure 1.11. The output ratings are given as:

- maximum output power: 480 W
- maximum output voltage to simulate the open-circuit voltage: 65 V
- maximum output current to simulate the short-circuit current: 8 A
- peak-to-peak voltage ripple: 125 mV.

One key feature of a PV array simulator is the accuracy with which it simulates the I–V curve and represents the open-circuit voltage, short-circuit current, and the MPP. Another important measure, often neglected by users, is the speed of dynamic



**Figure 1.11** Agilent 4350B PV array simulator.

response: the time in transition from one steady state to another. A real PV module or array is formed by semiconductors and shows a significantly high dynamic bandwidth. This can be explained by noting that the I–V output curve responds immediately whenever the load condition changes. However, it is impossible for a switching-mode power supply to mimic the same response. They are constrained in their response time or dynamic bandwidth.

It has been reported that a PV array simulator is too slow to test high-speed MPPT performance. For example, according to the product manual, the settling time of the E4350B is 25 ms. It is impossible to test an MPPT algorithm with a tracking speed of more than 40 Hz. However, a lot of MPPT algorithms and corresponding power-conditioning circuits have been developed for significantly higher speeds.

Another drawback results from the well-known disadvantages of switching-mode power supplies: self-resonance, output waveform ripples, and noise. Conventional DC power supplies show the tradeoff between the filter size and dynamic response. The filter can be sized with significant inductance and capacitance to mitigate ripples. However, the approach lowers the speed of the dynamic response. As a result, for the latest technologies, it is recommended that a PV array simulator be used for proof of concept. However, for accurate comparison of PV system performance, including both dynamics and steady-state performance, the suitability of PV array simulators should be carefully considered. It should be kept in mind that the PV array simulator is an imperfect electronic device and that it can interact with electronic power converters during tests.

## 1.8 Power Interfaces

In some cases, the PV generator is directly coupled to the load without any power interface. The majority of PV power systems are equipped with power-conditioning circuits for the interfaces between the generators and loads. A converter is the equipment that changes electrical voltage levels or waveforms.

Switching-mode power converters have high conversion efficiency and compact size, and are commonly used for PV power interfaces, battery power interfaces, and grid power interfaces. In power electronics, hundreds of converter topologies have been developed. Table 1.5 lists the DC/DC topologies that are commonly used for power interfaces on the PV side and battery side.

Table 1.6 lists the converter topologies that are commonly used for DC-to-AC conversion. They are also known as inverters, and change not only the voltage level but also the waveform. The input is from the DC source – PV generators or batteries – and the output can be connected to the AC grid or an AC load. The analysis, design, simulation, dynamic modeling, and control of the topologies are explained in Chapters 5–7.

## 1.9 Standalone Systems

Standalone PV systems supply power to local loads, and so are independent of the grid distribution network. Their history can be traced back to the 1950s, when PV technology was widely used for space power supplies. Solar radiation is more intense

**Table 1.5** Converters used for DC/DC power interfaces.

Topology	Isolation	Description
Boost converter	No	Ratio of DC output voltage to DC input voltage not less than 1.
Buck converter	No	Ratio of DC output voltage to DC input voltage not larger than 1.
Full-bridge isolated buck converter	Yes	When the winding turn ratio of the transformer is reset to 1:1, it produces the DC output voltage lower in magnitude than the DC input voltage.
Buck–boost converter	No	The voltage conversion ratio is flexible: higher, lower, or equal to 1. However, the input and output port do not share a common ground point.
Flyback converter	Yes	When the winding turn ratio of the transformer is reset to 1:1, the analysis can be based on the principle of the buck–boost converter.
Tapped inductor converter	No	The operation follows the principle used for the boost topology except for the tapping connection of the inductor. Potential for high step-up conversion ratio of voltage.
Dual active bridge	Yes	A bidirectional DC/DC converter that can be used as the battery power interface to support DC grids or DC links.

**Table 1.6** Converters for DC/AC power interfaces.

Topoloty	Description
H-bridge inverter	Conversion from DC to single phase AC.
Voltage source inverter (VSI)	Conversion from DC to three-phase AC, controlled by AC voltage regulation.
Current source inverter (CSI)	Based on the same circuit as VSI, and used for DC to three-phase AC conversion, but controlled by AC current regulation.

in space because it is not attenuated by the atmosphere and not blocked by clouds. The outer atmosphere is considered an ideal environment for solar PV power generation. However, their recent application has mostly been on Earth. The major applications of standalone systems include satellites, spacecraft, space stations, remote homes, villages, street lights, communication sites, water pumps, and vehicles. Nowadays, these systems are mainly installed in areas where grid connections are unavailable. Grid-connected PV systems have clear advantages for massive solar power production since the utility grid is a significant energy buffer that can accommodate the intermittency of solar power generation.

Standalone PV systems can supply either DC, AC, or both, depending on the load requirement. In some applications, PV generators can supply loads directly or through power interfaces without significant energy storage. Power-conditioning equipment might be needed for voltage conversion in directly coupled systems. The majority of

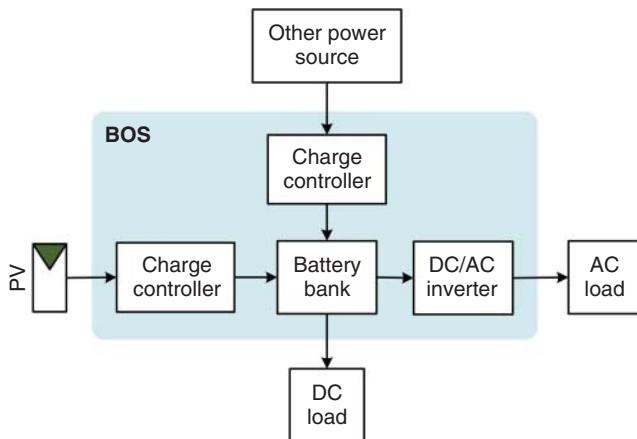


**Figure 1.12** Typical standalone system configuration, with PV generator and energy storage. BOS, balance of system.

applications require energy storage, because of the intermittent nature of PV power generation.

Hybrid systems take power from wind turbines, fuel cells or conventional engine-based generators, as well as solar power, as shown in Figure 1.12. Without other resources, a PV-battery system is not a hybrid system, because the energy storage system is an energy buffer, but not another electrical production source. The balance of system (BOS) consists of all equipment between the power sources and the loads. Charge controllers are commonly required to charge the battery bank. Filters, means of disconnection, and protection devices are also important components of the BOS, but they are not illustrated in Figure 1.12.

The DC/AC voltage source inverter (VSI) produces AC waveforms from DC sources. The majority of AC loads are supplied with a sine wave AC source. Some take square waves or modified square waves, allowing simple and low-cost topologies to be used in the VSI. The waveforms are illustrated in Figure 1.13, based on a frequency of 50 Hz. The

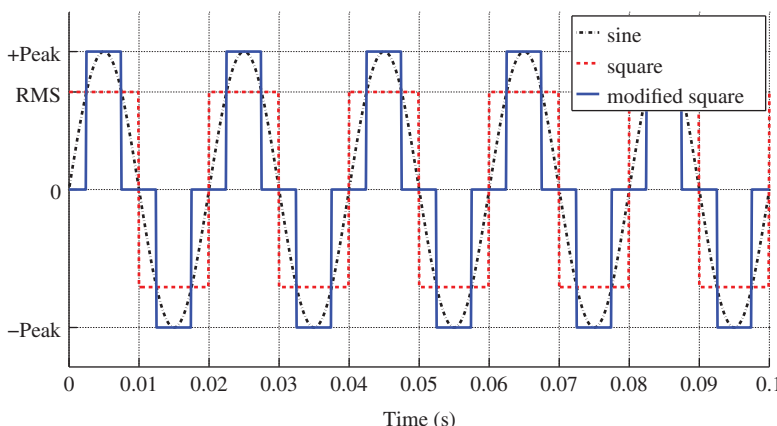


**Figure 1.13** Typical waveforms output by voltage source inverter.

total harmonic distortion of the square waveform is 48.3%. It should be noted that the pure sine-wave output requirement for standalone PV systems is no longer as demanding as before, because most modern devices tend to use DC supplies and are more tolerant of differing power supplies. However, in certain environments, noise and electromagnetic interference might be concerns where the AC output does not have a pure sinusoidal waveform.

The most impressive PV standalone system is Solar Impulse 2, a lightweight airplane solely powered by solar energy. Starting from Abu Dhabi on 9 March 2015, it completed the first entirely solar-powered flight around the world. The distance of 40 000 km is considered as the longest solo solar flight ever achieved. The historic voyage took more than 27 months, with the plane touching down again in Abu Dhabi on 26 July 2016. The flight record is summarized in Table 1.7.

A Swiss team initialized the ambitious idea of developing an aircraft purely powered by solar energy with battery support. The mission aimed to promote clean technologies. The plane was powered by 17 000 solar cells built into the body and wings. The longest and the most difficult non-stop flight took 5 days (118 h) and 7212 km from Nagoya, Japan to Honolulu, USA. To date, this is a world record for an uninterrupted flight. It was achieved by the pilot, Andre Borschberg. A photo taken in March 2015 when the Solar Impulse 2 was stationed in Abu Dhabi, is shown in Figure 1.14.

From certain points of view, the aircraft should be classified as a motorized glider. The wingspan is 73 m, which is bigger than that of a Boeing 747 jumbo jet. However,

**Table 1.7** Record of Solar Impulse journey.

Leg	From	To	Distance (km)	Start date	Total (h)	Average speed (km/h)
1	<u>Abu Dhabi</u> , UAE	Muscat, Oman	772	3/09/15	13	34
2	Muscat, Oman	Ahmedabad, India	1468	3/10/15	15	97
3	Ahmedabad, India	Varanasi, India	1170	3/18/15	13	89
4	Varanasi, India	Mandalay, Myanmar	1536	3/19/15	13	104
5	Mandalay, Myanmar	Chongqing, China	1450	3/30/15	20	71
6	Chongqing, China	Nanjing, China	1241	4/21/15	17	71
7	Nanjing, China	Nagoya, Japan	2852	5/30/15	44	65
8	Nagoya, Japan	Hawaii, USA	7212	6/28/15	118	61
9	Hawaii, USA	San Francisco, USA	4086	4/21/16	62	65
10	San Francisco, USA	Phoenix, USA	1113	5/02/16	16	70
11	Phoenix, USA	Tulsa, USA	1570	5/12/16	18	86
12	Tulsa, USA	Dayton, USA	1113	5/21/16	16.6	67
13	Dayton, USA	Lehigh valley, USA	1044	5/25/16	16.8	62
14	Lehigh valley, USA	New York, USA	265	6/11/16	4.7	57
15	New York, USA	Seville, Spain	6765	6/20/16	71	95
16	Seville, Spain	Cairo, Egypt	3745	7/11/16	48.8	77
17	Cairo, Egypt	<u>Abu Dhabi</u> , UAE	2694	7/24/16	48.6	55

Source: [www.solarimpulse.com](http://www.solarimpulse.com).



**Figure 1.14** Solar Impulse 2.

the plane can host only one pilot and weights approximately the same as a family car. From Table 1.7, the flight speed varies from 34 km/h to 104 km/h, and the average speed is about 70 km/h, slower than the majority of vehicles traveling on express highways. It usually takes less than 5 h to drive a car from Abu Dhabi to Muscat and less than one hour for commercial flights. However, Table 1.7 shows that Solar Impulse 2 took 13 h. Furthermore, the solar-powered aircraft is very sensitive and vulnerable to weather conditions because of its lightness: it weighs only 2300 kg. The onboard battery bank was seriously damaged during the 7212-km flight from Nagoya to Hawaii. The damage caused significant delays.

There is no doubt that Solar Impulse inspired the world towards the use of clean technologies and renewable energy. People around the world admire the courage and the effort of the founders and pilots in promoting solar energy for aviation. However, the technical data show that Solar Impulse aircraft might be a bad application of PV technology. The current power density of PV materials is generally too low to serve as the sole power source for either ground vehicles or aircraft. Due to size constraints, transport vehicles generally demand high power density by weight and volume, which rules out current PV technologies. However, this cannot stop the PV power generation being used as a secondary power source in hybrid systems for transportation. For example, PV power might be used to reduce fuel consumption in ground vehicles or to enable unmanned aerial vehicles to stay longer in the sky.

Recently, another standalone system that does not integrate with battery storage has become popular. PV power is used as an ancillary source for isolated electric networks based on fossil-fueled generation. The aim is fuel saving in remote places where the fuel cost is high and fossil-fueled generation causes air pollution. It is also a cost-effective solution because no batteries are used.

Without a significant energy buffer, system integration can be a challenge when PV power penetration is more than 25%. However, high penetration can achieve high fuel

savings. Since the load fluctuations might produce significant disturbances, control and coordination of wind and PV power interfaces becomes critical to maintaining grid frequency and voltage. Communication is generally required to optimally coordinate the operations of the generators. Utility-scale examples can be found at [www.sma.de](http://www.sma.de), in the shape of PV–diesel hybrid systems. Battery storage is optional, and not mandatory in such systems. Current battery technologies are expensive, when the short lifespans and the operating-environment constraints are considered.

## 1.10 AC Grid-connected Systems

One drawback of a standalone system is that the PV array is usually oversized, so as to accommodate the worst-case scenarios in terms of solar power generation. Solar energy is wasted if the generated power cannot be stored or consumed. Recently, an increasing number of systems have been connected to the AC electric distribution network. The electrical production and distribution network – the grid – is a utility system, which is external to and not controlled by the PV system. Such systems are also called interactive systems or grid-connected systems, and can be operated for full-time maximum power injection. Figure 1.15 shows three examples of grid-connected systems, with and without battery storage. The key component in grid-connected PV systems is the utility-interactive inverter, which performs the DC/AC conversion and the required interconnection functions.

A simple grid-connected system, mainly used for small-scale applications, is illustrated in Figure 1.15a. Local loads can be supplied through the grid interconnection.

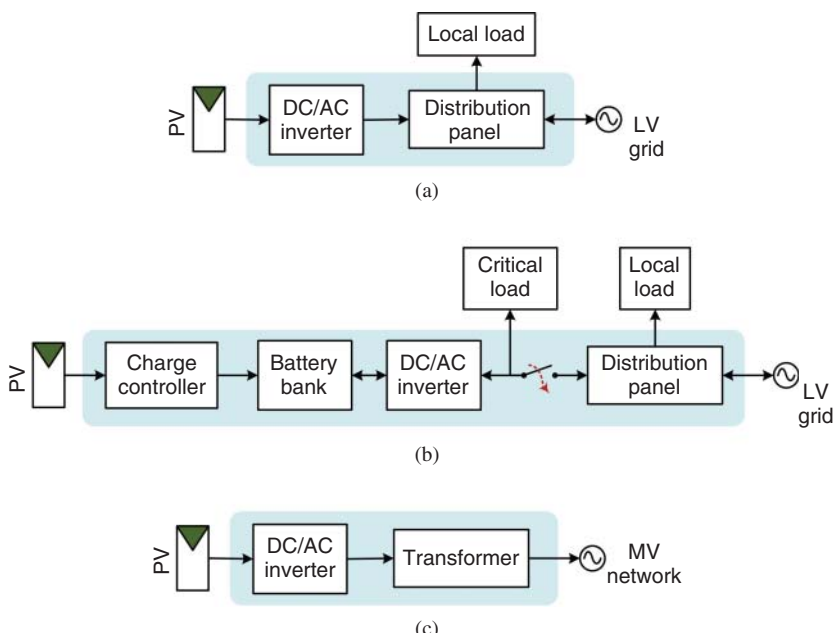


**Figure 1.15** Grid-connected PV power systems with PV generators and inverters: (a) simple system; (b) grid-connected system with battery storage; (c) PV power plant.

## 4

### PV Output Characteristics and Mathematical Models

I-V and P-V curves are commonly used to illustrate the outputs of PV cells, modules, strings, or arrays, as discussed in Section 1.6. Computer simulation is an important tool to reproduce the behavior of PV power systems in response to various environmental conditions and load disturbances. A computational model can be developed to recreate the PV generator output under variations in irradiance and temperature. There are various modeling approaches that have been presented in literature to represent PV output characteristics.

Doping creates an interface between two types of semiconductor material – p-type and n-type – inside a single crystal of a semiconductor. These p-n junctions are the elementary units of most semiconductor electronic devices: diodes, transistors, and integrated circuits. A crystalline-based PV cell is also constructed from a large area of silicon p-n junction, so a diode model is naturally used to represent the output characteristics of crystalline-based solar cells.

A model to represent crystalline-based PV cells is usually formed from the equivalent circuits. These models are usually categorized into two main types: single-diode models (SDMs) and double-diode models (DDMs), and their equivalent circuits are shown in Figures 4.1 and 4.2, respectively.

An ideal model for PV cells should have a current source in parallel with a diode. However, due to various non-ideal factors, the equivalent circuit of the standard SDM also includes one shunt resistor and one series resistor, as illustrated in Figure 4.1. In this book, the model is defined as the complete single diode model (CSDM) in order to distinguish it from other simplified single-diode models (SSDMs). The current–voltage characteristics according to the equivalent circuit are expressed as

$$i_{pv} = i_{ph} - i_d - \frac{v_d}{R_h} \quad (4.1)$$

The I-V characteristics of the p-n junction diode is nonlinear, and it can be represented in exponential form:

$$i_d = i_s \left[ e^{\left( \frac{q v_d}{k T_c A_n} \right)} - 1 \right] \quad (4.2)$$

where  $v_d$  is equal to

$$v_d = v_{pv} + i_{pv} R_s \quad (4.3)$$

This is based on the theory of Shockley (1949). The symbol  $T_c$  is the absolute temperature of the p-n junction. The ideality factor of the diode,  $A_n$ , is a measure of how closely

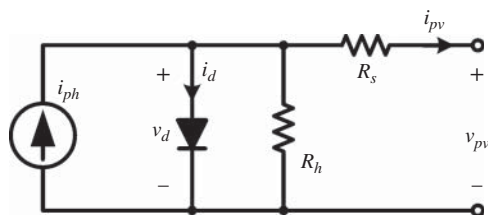


**Figure 4.1** Equivalent circuit of single-diode model.

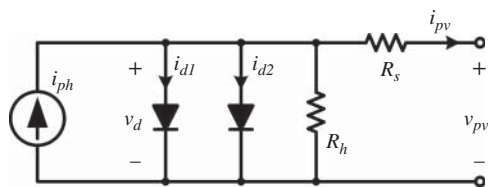


**Figure 4.2** Equivalent circuit of double-diode model.

the diode follows the ideal diode equation, which is defined as  $A_n = 1$ . The value of  $A_n$  typically ranges from 1 to 2. Values of the p-n junction constants, model parameters, and variables are listed in Tables 4.1–4.3, because they are frequently used in the chapter. To represent the relation of  $v_{pv}$  and  $i_{pv}$ , or the I–V curve, five unknown parameters should be identified to give the CSDM:  $i_{ph}$ ,  $i_s$ ,  $A_n$ ,  $R_s$ , and  $R_h$ . Thus, the model is sometimes referred to as the five-parameter model.

The DDM includes one current source, two diodes, and shunt and series resistances, as shown in Figure 4.2. The output current of the DDM is expressed as

$$i_{pv} = i_{ph} - i_{d1} - i_{d2} - \frac{v_d}{R_h} \quad (4.4)$$

where the currents in the two diodes can be expressed as:

$$i_{d1} = i_{s1} \left[ e^{\left( \frac{qv_d}{kT_c A_{n1}} \right)} - 1 \right] \quad (4.5)$$

$$i_{d2} = i_{s2} \left[ e^{\left( \frac{qv_d}{kT_c A_{n2}} \right)} - 1 \right] \quad (4.6)$$

and where the diode voltage is

$$v_d = v_{pv} + i_{pv} R_s \quad (4.7)$$

**Table 4.1** PV model coefficients.

Symbols	Term definition	Value
$E_{STC}$	Irradiance at STC*	1000 W/m <sup>2</sup>
$k$	Boltzmann constant	$1.38 \times 10^{-23}$ J/K
$q$	Charge	$1.6 \times 10^{-19}$ C
$T_{CS}$	PV cell temperature at STC*	298°K
$V_{TCS}$	Thermal voltage of p-n junction at STC*	25.7 mV

\*Standard test conditions (STC): 1000 W/m<sup>2</sup>, AM1.5 standard reference spectrum, and 298 K (or 25°C).

**Table 4.2** PV model parameters and constants.

Symbols	Definition	Unit
$\alpha_T$	Temperature coefficient on PV current	(A/A)/K
$\beta_T$	Temperature coefficient on PV voltage	(V/V)/K
$\gamma_T$	Irradiance coefficient on PV power	(W/W)·m <sup>2</sup> /W
$\nu_T$	Irradiance coefficient on PV voltage	(V/V)·m <sup>2</sup> /W
$A_n$	Diode ideality factor in the SDM	n/a
$A_{n1}$	Diode ideality factor 1 in the double-diode model	n/a
$A_{n2}$	Diode ideality factor 2 in the double-diode model	n/a
$I_{MS}$	PV current at the maximum power point (MPP) at the STC	A
$I_{ph}$	PV photon current at the STC	A
$I_{SCS}$	PV short-circuit current at the STC	A
$I_{SS}$	PV short-circuit current at the STC	A
$P_{MPP}$	PV power at the maximum power point (MPP) at the STC	W
$R_s$	Series resistance	$\Omega$
$R_h$	Shunt resistance	$\Omega$
$V_{MS}$	PV voltage at the maximum power point at the STC	V
$V_{OCs}$	PV open-circuit voltage at the STC	V

**Table 4.3** PV model variables.

Symbols	Definition	Unit
$E_a$	Solar irradiance	W/m <sup>2</sup>
$I_M$	Instant MPP current	A
$i_{ph}$	PV photon current	A
$i_{pv}$	PV cell output current	A
$i_d$	Diode current	A
$i_s$	Diode reverse-bias saturation current	A
$T_C$	PV cell temperature	K
$v_d$	Diode voltage	V
$V_M$	Instant MPP voltage	V
$v_{OC}$	PV open-circuit voltage	V
$v_{pv}$	PV cell terminal voltage	V
$v_t$	Thermal voltage of p–n junction	V

Seven unknown parameters must be identified in the DDM:  $i_{ph}$ ,  $i_{s1}$ ,  $i_{s2}$ ,  $A_1$ ,  $A_2$ ,  $R_s$ , and  $R_h$ . The model coefficients and variables are as set out in Tables 4.1–4.3. The DDM is commonly considered to be a more comprehensive model of PV cell output characteristics than the SDM. Two more tuning parameters appear in the model than in the SDM, in order to accurately reproduce the output characteristics of PV cells. However, the model is not commonly used due to its complexity (Huang et al. 2016;

Mahmoud et al. 2013). The model in (4.4) includes two independent terms for diode current, which increases the complexity for parameter identification and computer simulation. Improper tuning of the parameters can prevent the claimed advantage of accuracy being achieved. Parameter identification for the DDM is also very sensitive to initial conditions (Romero-Cadaval et al. 2013).

Due to the complexity of the DDM, the SDM is normally used for simulating PV power systems, because it offers a reasonable trade-off between simplicity and accuracy. For this reason, the DDM will not be further discussed.

## 4.1 Ideal Single-diode Model

Based on the p-n junction structure for both PV cell and diode, the ideal single-diode model (ISDM) is a current source in parallel with a diode, as shown in Figure 4.3. It can be considered the simplest SDM. In comparison with the CSDM shown in Figure 4.1, the series resistance and shunt resistance are removed. The mathematical expressions are therefore:

$$i_{pv} = i_{ph} - i_s \underbrace{\left[ e^{\left( \frac{qv_{pv}}{kT_c A_n} \right)} - 1 \right]}_{i_d} \quad (4.8)$$

Without the resistances, three model parameters must be identified in the modeling process: the photon current ( $i_{ph}$ ), the diode reverse bias saturation current ( $i_s$ ), and the diode ideality factor ( $A_n$ ). Three independent constraints are required to identify the three unknown parameters in (4.8).

### 4.1.1 Product Specification

A common source for identifying values for the PV model parameters is the product datasheets provided by PV cell or module manufacturers. The modeling process is to match the PV output characteristics with these data, which are prepared at STC. Table 4.4 illustrates one such specification. All data refer to the multi-crystalline solar cell, IM156B3, which is manufactured by MOTECH Industrial Inc. To avoid any confusion, it should be noted that the datasheet was downloaded in 2014 showing the version of October 2012. It might not be consistent with the latest data since the manufacturer often releases new product versions. The data that are useful for PV cell modeling and simulation include the STC values of the short-circuit current  $I_{SCS}$ , open-circuit voltage  $V_{OCS}$ , the operating voltage and current at the maximum power point (MPP) ( $V_{MS}, I_{MS}$ ), the temperature coefficients ( $\alpha_T, \beta_T$ , and  $\gamma_T$ ), and the correction factors for irradiation on the electrical outputs. The symbols  $\alpha_T$ ,  $\beta_T$ , and  $\gamma_T$  are the

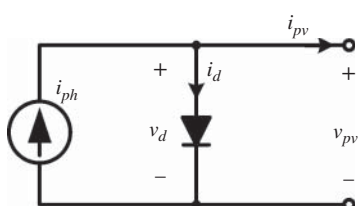


**Figure 4.3** Equivalent circuits of the ideal single-diode model.

**Table 4.4** Sample solar cell data.

Basic information					
Manufacturer	Model	Cell material	Dimensions		
MOTECH	IM156B3-164	Multi-crystalline	156 × 156 ± 0.5 mm		
Electrical performance at STC					
Efficiency	$P_{MPP}$	$I_{MS}$	$V_{MS}$	$I_{SCS}$	$V_{OCS}$
16.4 %	3.99 W	7.85 A	0.509 V	8.38 A	0.614 V
Temperature coefficients					
$\alpha_T$ (%/°C)	$\beta_T$ (%/°C)	$\gamma_T$ (%/°C)			
0.06	-0.33	-0.40			
Correction factors for irradiance					
$E_a$ (W/m <sup>2</sup> )	Voltage correction (V/V)		Current correction (A/A)		
1000	1.000		1.000		
800	0.989		0.798		
600	0.972		0.597		
200	0.911		0.192		

All symbols shown above refer to Tables 4.2 and 4.3.

temperature coefficients for the correction of the PV cell output current, voltage, and power, respectively. Parameter identification is performed at the PV cell level since the cell is the fundamental unit for construction of modules and arrays.

#### 4.1.2 Parameter Identification at Standard Test Conditions

ISDM parameters are initially determined at STC since the data are available from the product datasheet. For the case study, the modeling uses the data in Table 4.4.

When the terminal of the equivalent circuit, as shown in Figure 4.3, is shorted, the diode current,  $i_d$ , is equal to zero. The value of the photon current,  $i_{ph}$ , is equal to the short-circuit current,  $I_{SCS}$ , which is available from the product datasheet. Thus the photon current,  $i_{ph}$  becomes known at STC. Two unknowns remain in the ISDM to represent the diode.

When the terminal of the equivalent circuit, as shown in Figure 4.3, is opened, the output current of the PV cell,  $i_{pv}$ , is equal to zero. The value of the diode current,  $i_d$ , becomes equal to the photon current,  $i_{ph}$ , which is the  $I_{SCS}$  at STC. This can be expressed as in (4.9), which includes two unknown parameters of  $I_{SS}$  and  $A_n$ :

$$I_{SCS} = I_{SS} \left[ e^{\left( \frac{V_{OCS}}{V_{TCS} A_n} \right)} - 1 \right] \quad (4.9)$$

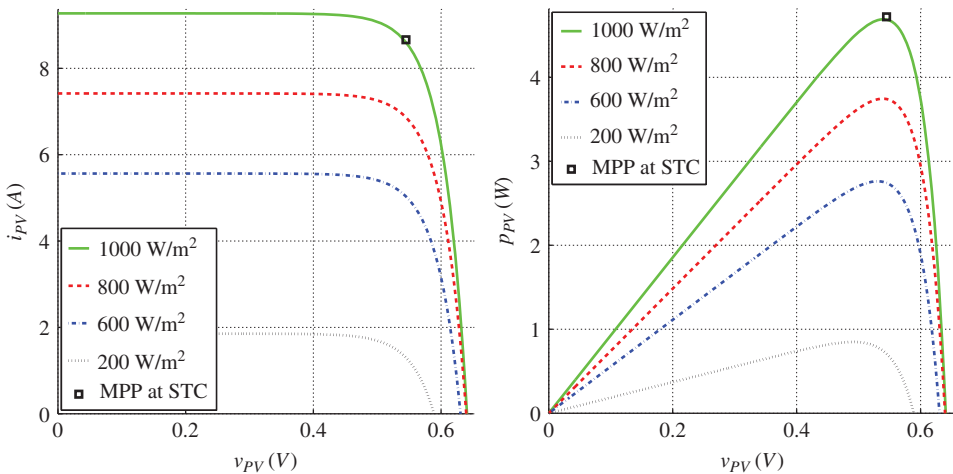


**Figure 4.21** I–V curve of the JAC-M6SR-3 cell modeled with constant temperature ( $25^{\circ}\text{C}$ ) and variable irradiance.

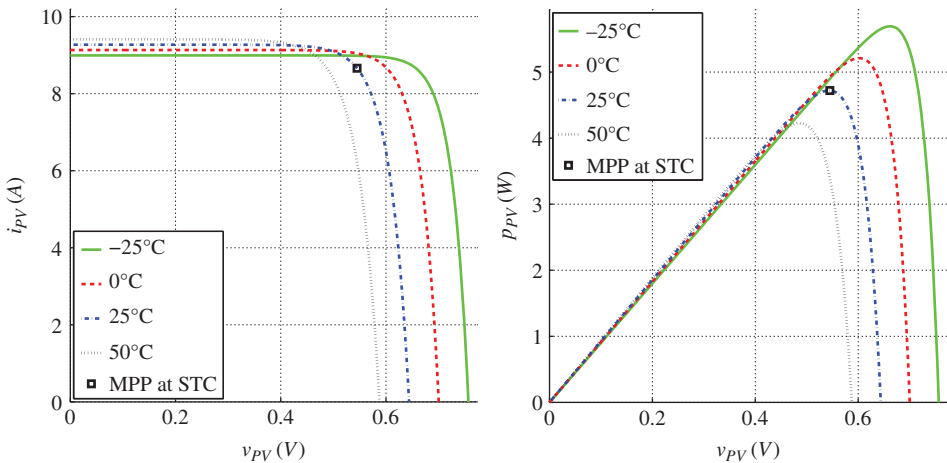


**Figure 4.22** I–V curve of JAC-M6SR-3 cell modeled with constant irradiance ( $1000 \text{ W/m}^2$ ) and variable temperature.

modeling process ultimately selected SSDM2 to achieve zero deviation at the MPP. For the JAC-M6SR-3 cell, the process stops at SSDM1 since the model parameters are physically meaningful. The SSDM1 output for JAC-M6SR-3 with changes in solar irradiance and temperature are shown in Figures 4.21 and 4.22, respectively. If the values of  $D_{MPP}$  are insignificant, the ISDM can be adopted for both cell examples.

## 4.5 Complete Single-diode Model

Most product datasheets provide the I–V and even the P–V curve in low-resolution figures, which serve as a basic reference for the output characteristics. The low

## 5

### Power Conditioning

Power conditioning is required to interface the PV source circuit for power processing. The key functional blocks of a typical two-stage conversion system for AC grid interconnection is shown in Figure 5.1.

The PV link is the interface between the PV source circuit and the PV-side converter (PVSC). It provides a filtering function to maintain a steady voltage at the link. The PVSC is a DC/DC power interface, the input of which is coupled to the PV link and is usually controlled by the maximum power point tracking (MPPT) algorithm so that maximum energy harvesting is achieved. Throughout the book, it is occasionally referred to the “PV-side power interface.” The grid link is the interface between the grid and the grid-side converter (GSC). It provides a filtering function to guarantee the power quality required by the grid. A transformer can be implemented at this stage for the purpose of galvanic isolation and voltage conversion. The GSC is the power interface between the DC link and the AC grid link. It converts DC to AC for grid interconnection. The DC link is commonly formed by capacitors, which maintain a steady DC-link voltage between the two conversion stages.

In systems with single-stage conversion, one centralized power converter is used, as shown in Figure 5.2. Thanks to the simplicity of its configuration, the system gives higher efficiency and lower costs than a two-stage-conversion system. To avoid confusion, the DC/AC converter for single-stage conversion is considered the GSC. The PV link is merged with the DC link, as shown in Figure 5.2. The design and analysis of the GSC in single-stage conversion systems is generally the same as in two-stage conversion systems.

Shown in Figure 1.16 and described in Section 1.11, a DC microgrid is composed of the power interfaces for energy storage units. Bidirectional DC/DC converters are usually required to interface batteries with a DC bus. Therefore, one section in this chapter is about the battery-side converters (BSCs) that are required for the charge and discharge operations of battery storage units.

The inductance and capacitance parameters in the following design examples are theoretically sized and based on the ideal converter system. They are considered as minimal values for proof of concept and simulation. They are also the reference and the starting point for practical designs in which all constraints are considered. When all the parameters are re-tuned to meet all requirements, they can be again used for simulation to prove the upgraded design concept. The modeling and simulations in this chapter are based on the basic functions of Simulink rather than circuit-based modeling methods, such as Simscape Power Systems.

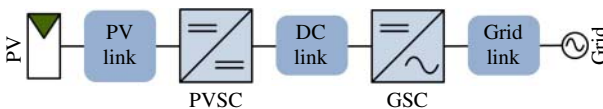


**Figure 5.1** Block diagram of a grid-connected PV system with two-stage power conversion. PVSC, PV-side converter; GSC, grid-side converter.

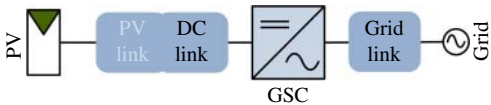


**Figure 5.2** Block diagram of grid-connected PV system with single-stage power conversion. GSC, grid-side converter.

## 5.1 PV-side Converters

The PVSC is the DC/DC power-conditioning circuit, the input of which is connected to the PV link. In standalone systems, the PVSC can be used as the power interface to charge batteries or supply power to local loads. The common DC/DC topologies used for PVSCs can include buck, boost, buck-boost, flyback, tapped-inductor, and full-bridge isolated DC/DC converters. It is important to design a topology that gives maximum power yield, without increasing the circuit complexity. Figure 5.3 illustrates the procedure that is recommended to design, simulate, and evaluate the PVSC in order

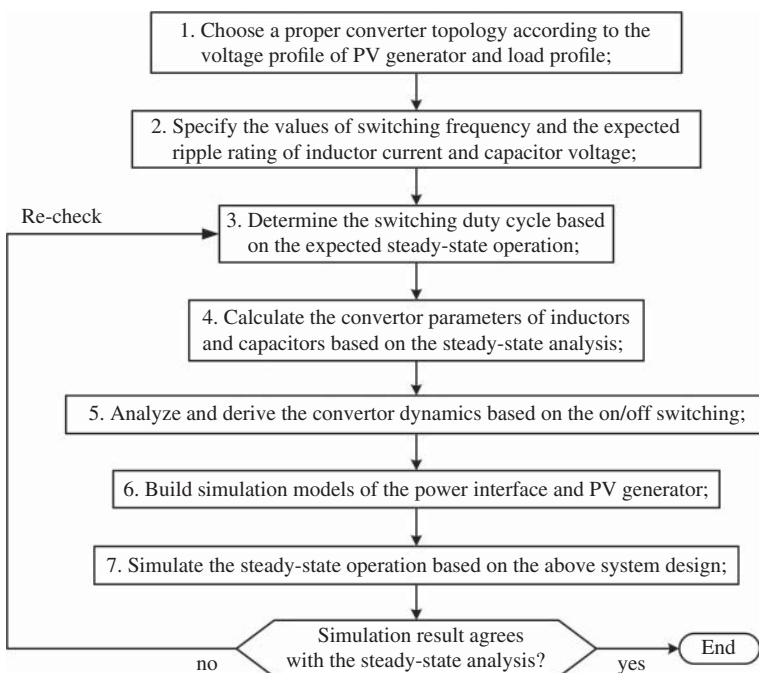


**Figure 5.3** Recommended procedure to design, simulate, and evaluate PV-side power interface.

to meet the system specification and give the correct performance rating. The procedure follows the sequence of

- topology selection
- specification
- steady-state analysis
- design
- simulation modeling
- simulation evaluation.

Simulation is an effective tool and widely used to prove the design concepts of PVSCs and the effectiveness of models.

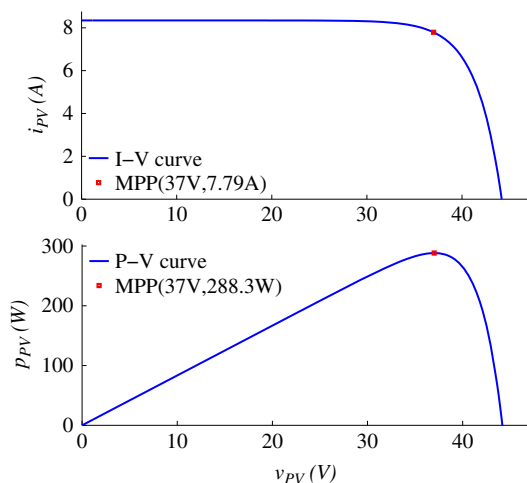
### 5.1.1 PV Module for Case Study

In the following study, one specific PV module is used to demonstrate PVSC design and simulation. Its electrical characteristics at STC are shown in Figure 5.4. The PV module is constructed from 72 multi-crystalline cells and is used for demonstration purposes only. The simulation model is based on the ISDM that is introduced in Section 4.1. The short-circuit current and open-circuit voltage are 8.34 A and 44.17 V respectively. The maximum power point (MPP) is at (37.0 V, 7.79 A). The peak power is 288.3 W, as indicated in the plot.

### 5.1.2 Buck Converter

A buck converter circuit, as shown in Figure 5.5, can be used for the PVSC. The converter is controlled by pulse width modulation (PWM), of which the switching duty cycle is the control-input variable. A step-down topology should be considered if the converter-output voltage is never higher than the PV terminal voltage ( $v_{pv}$ ) at the MPP,  $V_{MPP}$ , when the normal voltage variation of both sides has been considered. The condition can be expressed as:  $V_{O(max)} \leq V_{MPP(min)}$ . The lowest value of the PV terminal voltage at the MPP,  $V_{MPP(min)}$ , can be estimated from the highest ambient temperature

**Figure 5.4** I–V and P–V curves of PV module output.



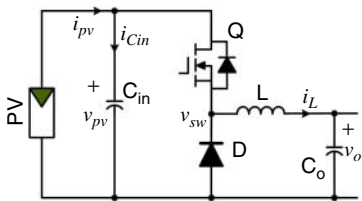


Figure 5.5 Buck converter used for PV power interface.

and the minimum irradiance for the converter to operate. The highest value of the output voltage,  $V_{O(max)}$ , can be determined from the load profile. For battery-charging applications, the battery voltage becomes the converter-output voltage,  $v_o$ , which varies from the cut-off voltage at 0% state of charge (SOC) to the highest level: the open-circuit voltage at 100% SOC. In this case, the value of  $V_{O(max)}$  is equivalent to the open-circuit voltage of the battery at 100% SOC.

One additional concern of the buck topology is that the input current is always pulsing or “chopped,” so significant input capacitance is required to smooth the PV-link voltage. This generally affects the dynamics of the PV-link voltage and causes significant ripple in the capacitor current,  $i_{Cin}$ . The output current is smooth in the buck topology because the inductor appears on the output side.

At STC and the predefined switching frequency,  $f_{sw}$ , the inductor ripple current and ripple voltage at the PV link should be specified by the peak-to-peak values,  $\Delta I_L$  and  $\Delta V_{PV}$ , respectively. Steady-state analysis can determine the duty cycle at the nominal load operating condition. At STC, the PV source circuit should be operated at the MPP, which is represented by  $V_{MPP}$  and  $I_{MPP}$ . The duty cycle can be calculated from:

$$D_o = \frac{V_{O-NOM}}{V_{MPP}} \quad (5.1)$$

with the assumption that the converter is operated in continuous conduction mode (CCM). The symbol  $V_{O-NOM}$  represents the nominal output voltage, which can be specified from the load profile. The value of the inductance,  $L$ , and the capacitance,  $C_{in}$ , can be calculated from (5.2) and (5.3), respectively.

$$L = \frac{V_{O-NOM}(1 - D_o)}{\Delta I_L f_{sw}} \quad (5.2)$$

$$C_{in} = \frac{I_{MPP}(1 - D_o)}{\Delta V_{PV} f_{sw}} \quad (5.3)$$

In this system, the capacitor  $C_{in}$  represents the PV link between the PV source circuit and the PVSC.

It should be noted that the thermal characteristics should be evaluated and considered for capacitor selection. Significant current ripple can be expected for filtering the pulsing current at the input side of the buck converter. Each capacitor is constrained by the allowable ripple current. The intrinsic equivalent series resistance (ESR) results in power loss when significant ripple current is conducted. High temperature is related to the early failure of capacitors. To evaluate the power loss and estimate the core temperature, the RMS value of the ripple current in  $i_{Cin}$  should be determined (see discussion in Section 5.6). In general, thermal analysis is considered as one of the most important aspects of the selection of capacitors and the design of power electronics.

When switch Q is “on,” the system dynamics can be represented as in (5.4) and (5.5).

$$i_L = \frac{1}{L} \int (v_{pv} - v_o) dt \quad (5.4)$$

$$v_{pv} = \frac{1}{C_{in}} \int (i_{pv} - i_L) dt \quad (5.5)$$

When Q is “off,” the system dynamics are as in (5.6) and (5.7).

$$i_L = \frac{1}{L} \int (-v_o) dt \quad (5.6)$$

$$v_{pv} = \frac{1}{C_{in}} \int i_{pv} dt \quad (5.7)$$

From the on/off states and the integral operation, a simulation model can be built by Simulink, as shown in Figure 5.6a. The model is based on the ideal buck converter, in which loss is not considered. Two single-pole–double-throw (SPDT) switches are utilized in the Simulink model for the switching between the on-state, (5.4) and (5.5), and the off-state, (5.6) and (5.7). The model includes three inputs:

- the pulse width modulation (PWM) command signal for the switches
- the output voltage determined by the load condition ( $v_o$ )
- the PV output current ( $i_{pv}$ ).

It outputs two signals: the inductor current ( $i_L$ ) and the PV-link voltage ( $v_{pv}$ ). The dynamic interaction is simulated by the integral operation, which is defined by (5.4)–(5.7). The saturation signs are shown in the Simulink blocks for integration, which constrains the inductor current ( $i_L$ ) and the PV-link voltage ( $v_{pv}$ ) to be always positive. All components can be packed together to form a single block to represent the buck converter, as shown in Figure 5.6b. The correspondence of the PV-link voltage ( $v_{pv}$ )

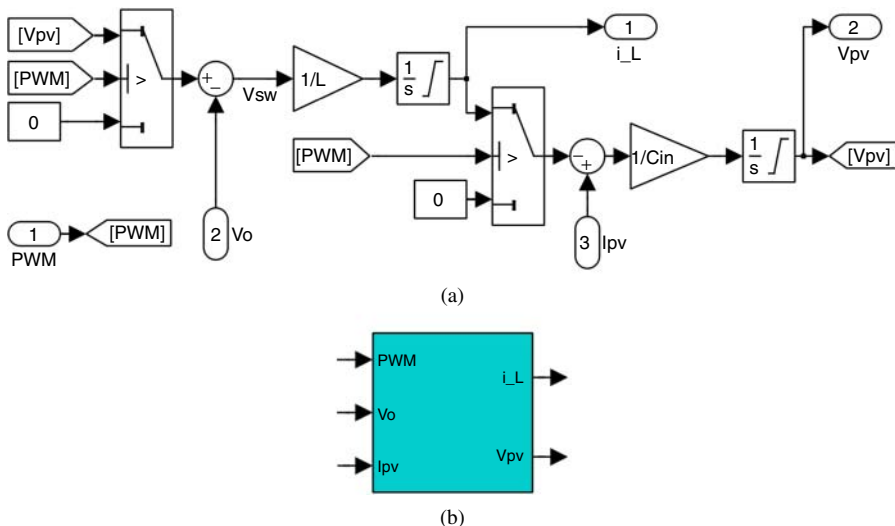


**Figure 5.6** Simulink model of buck converter used for PV power interface: (a) model composition; (b) integrated block.

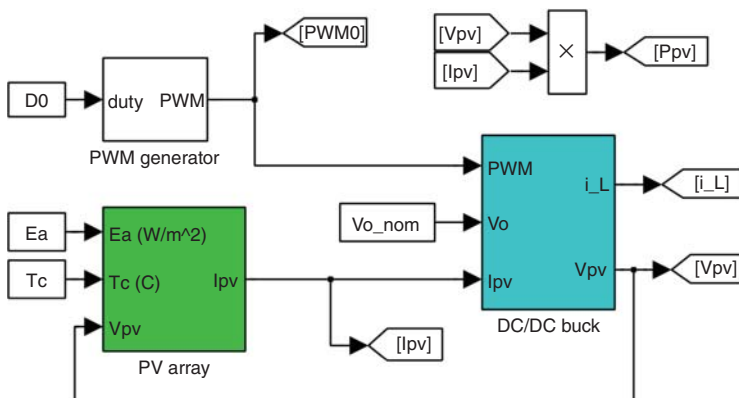


Figure 5.7 Simulink system using the buck converter for PV-side converter.

and the PV output current ( $i_{pv}$ ) should follow the PV source circuit model discussed in Chapter 4 and shown in Figure 4.25. The steady-state analysis and design can be simulated and verified using the Simulink model.

An example is given of charging a battery module with a nominal voltage of 24 V. The open-circuit voltage is 28 V when the battery module is fully charged. The power source is the PV module that was introduced in Section 5.1.1. Since the  $V_{MPP}$  is significantly higher than 28 V, a buck converter is selected for the power conditioning. The switching frequency is designed to be 50 kHz; the peak-to-peak ripple voltage of the PV module is specified as 0.2 V; and the peak-to-peak ripple of the inductor current is specified as 1 A. Based on the nominal battery voltage (24 V) and the STC of the PV module, the nominal duty cycle of the PWM can be calculated as 64.9% according to (5.1). Then the values of  $L$  and  $C_{in}$  can be calculated as 167  $\mu$ H and 272  $\mu$ F, by following (5.2) and (5.3), respectively. The system simulation model, as shown in Figure 5.7, is constructed together with the blocks of the PV module and the PWM generator.

The simulation result is shown in Figure 5.8, including the waveforms of  $i_L$ ,  $v_{pv}$ ,  $i_{pv}$ , and  $p_{pv}$ . When PWM signals are applied to the converter with its nominal duty cycle of 64.9%, the value of  $v_{pv}$  drops from the open-circuit voltage, 44.17 V, to the value of  $V_{MPP}$ , which is 37.0 V at the steady state. The signal of  $i_{pv}$  increases from zero to the value of  $I_{MPP}$ , which is 7.79 A at the steady state. The PV power ( $p_{pv}$ ) reaches the value of the MPP with the corresponding voltage and current, the same as the rating shown in Figure 5.8.

Figure 5.9 provides a zoom-in look at the waveform that was presented in Figure 5.8. The peak-to-peak ripple of the inductor current is measured as 1 A, corresponding to the specification. The peak-to-peak ripple of the PV-link voltage is also measured to match the specified value of 0.2 V. The fixed step-size of the numerical solver is chosen as 20 ns, which indicates that the simulation resolution is 1000 sampling points in each PWM switching cycle. The MPP is 288.3 W, the same as the PV module specification. The simulation verifies the system design and demonstrates the model's performance in the steady state. The same sizing and design principles can be applied to cases with different electrical ratings from the example.

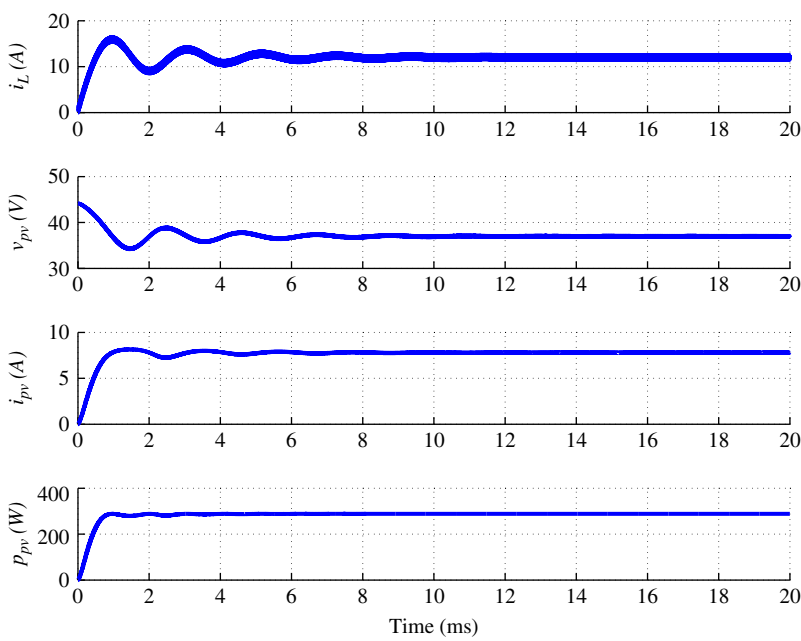


**Figure 5.8** Simulated waveforms of the PV power charger in the steady state.

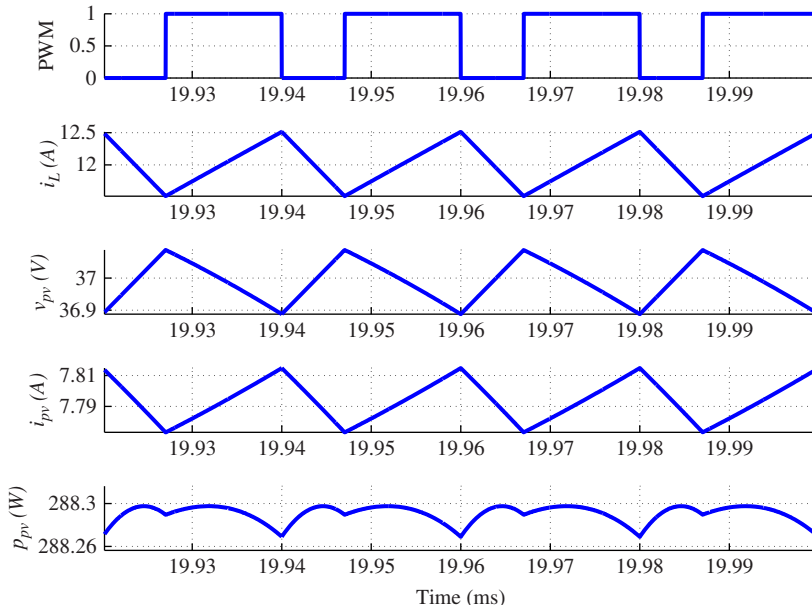


**Figure 5.9** Simulated waveforms of the PV power charger in the steady state.

changing magnetic fields. Loss of winding can be caused by the skin and proximity effects because of the applied frequency. In general, high-frequency losses should be considered when selecting the correct magnetic core material and designing the winding configuration. It is challenging to derive an accurate model for high-frequency losses due to the complexity of core materials and the difficulties of parameter identification. However, high-frequency loss can be evaluated through experimental tests in combination with the conduction loss. The temperature of the magnetic core and winding is an indicator for loss analysis.

## 5.7 Conversion Efficiency

The conversion efficiency is considered the most important measure of PV power interfaces. It is the ratio in percentage terms of the input to output power. A converter efficiency is not uniformly distributed at all power levels. Conventionally, peak efficiency is used as the performance index, because it represents the optimal operating point for the best conversion efficiency. However, the operation of PV power systems depends on the environmental conditions. The efficiency at a single operating condition will not be the best index to represent performance. Therefore, weighted values are introduced to evaluate the conversion efficiency of PV power interfaces.

The European efficiency and CEC efficiency measures are commonly applied and are expressed in (5.123) and (5.124), respectively.

$$\eta_{eu} = 0.03 \times \eta_{5\%} + 0.06 \times \eta_{10\%} + 0.13 \times \eta_{20\%} + 0.10 \times \eta_{30\%} \\ + 0.48 \times \eta_{50\%} + 0.20 \times \eta_{100\%} \quad (5.123)$$

$$\eta_{cec} = 0.04 \times \eta_{10\%} + 0.05 \times \eta_{20\%} + 0.12 \times \eta_{30\%} + 0.21 \times \eta_{50\%} \\ + 0.53 \times \eta_{75\%} + 0.05 \times \eta_{100\%} \quad (5.124)$$

The term “CEC” refers to the California Energy Commission. The coefficients indicate the importance of the efficiency of each level, based on assumptions about how often the PV converter will function at that level. The weighted values correspond to the climate in central Europe and California, USA. The symbol  $\eta_{x\%}$  represents the efficiency tested at  $x$  percent of the rated power level. The symbol  $\eta_{100\%}$  refers to the efficiency value at the rated power level.

Comparing the two performance indices, the European measure gives more weight at 50% of the inverter power rating, meanwhile, the CEC measure gives more at 70% of the conversion capacity. This reflects that the solar resource in California is greater than in central Europe.

## 5.8 Wide Band-gap Devices for Future Power Conversion

In general, the conversion efficiency in PV power systems has been pushed to a higher level than in other power electronic applications. The DC/AC converters that are applied at the string and array levels for grid connections have reached 97% or even higher efficiency. The DC/DC converters used for PV-side power interfaces are usually more than 98% efficient. MIPIs have relatively lower conversion efficiencies of between

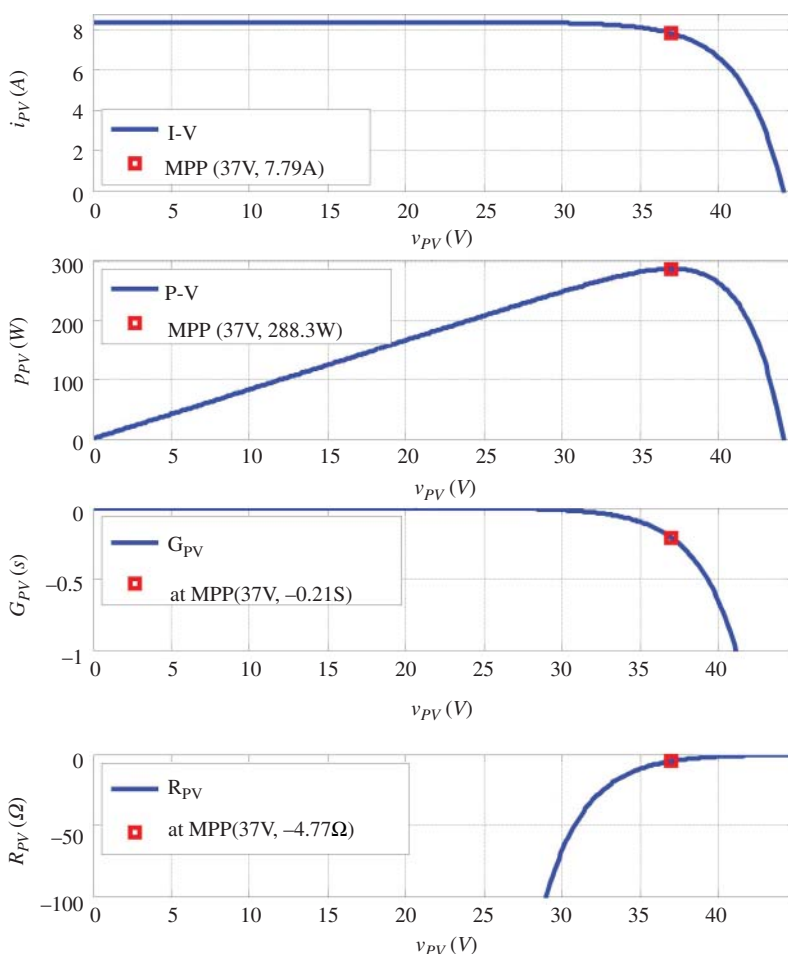


**Figure 6.1** Electrical characteristics of the PV module showing dynamic conductance and resistance.

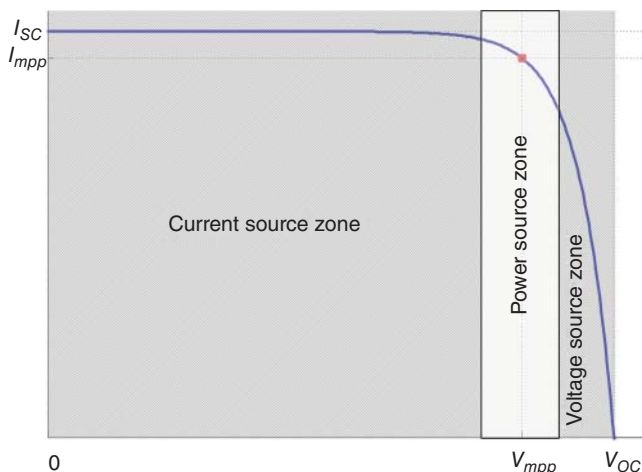


**Figure 6.2** Three-zone definition based on I-V curve.

# 8

## Maximum Power Point Tracking

The output of PV cells is limited by the current, voltage, and power. In a steady state of solar irradiance and cell temperature, there is a single operating point where the output of the voltage and current results in the maximum power output. The maximum power point (MPP) is occasionally called the “peak power point” (PPP) or “optimal operating point” (OOP) in the literature (Xiao et al. 2006). When the power is plotted against voltage (a P–V plot), the peak power point can be easily recognized, as shown in Figure 1.9.

In most PV power systems, a control algorithm called maximum power point tracking (MPPT) is used to take full advantage of the available solar energy (Xiao et al. 2011). The algorithm is occasionally called “peak power tracking.” The term MPPT is used in this book. The real-time operation is to control the PV-side power interface so that the operating characteristics of the load and the PV array always match each other at the MPP. The control objective is to maximize the power output for highest solar energy harvesting at any given instant.

This chapter introduces the MPPT techniques and provides background knowledge about recent developments. Simulations are used to demonstrate the operations that are widely used for practical implementation.

### 8.1 Background

The principle behind MPPT is the conductance or resistance match between the PV generator output and the load condition, as illustrated in Figure 8.1. In grid-connected systems, the load condition is not as straightforward as in standalone systems, but it can be equivalent to the active power level extracted from the PV generation. The plot shows that the MPP of the PV cell is located at 0.54 V and 8.2 A. When a load rated at 15.2 S in conductance or  $66\text{ m}\Omega$  in resistance is connected, the maximum power generation is achieved, which is 4.43 W. Any deviation from the ideal load resistance of  $66\text{ m}\Omega$ , such as an applied load resistance of  $0.1\text{ }\Omega$  or  $0.05\text{ }\Omega$  makes the PV cell output deviate from the MPP and produce less power, as illustrated in Figure 8.1.

The majority of loads require either constant voltage or current. When they are directly coupled with the PV generator, the load impedance cannot always be adjusted for the purpose of MPPT. However, when a power interface is connected between the load and PV generator, the load conductance or the impedance at the PV generator terminals can be varied through power conversion. The evolution is demonstrated in Figure 8.2, where a power interface is used between the PV generator and the

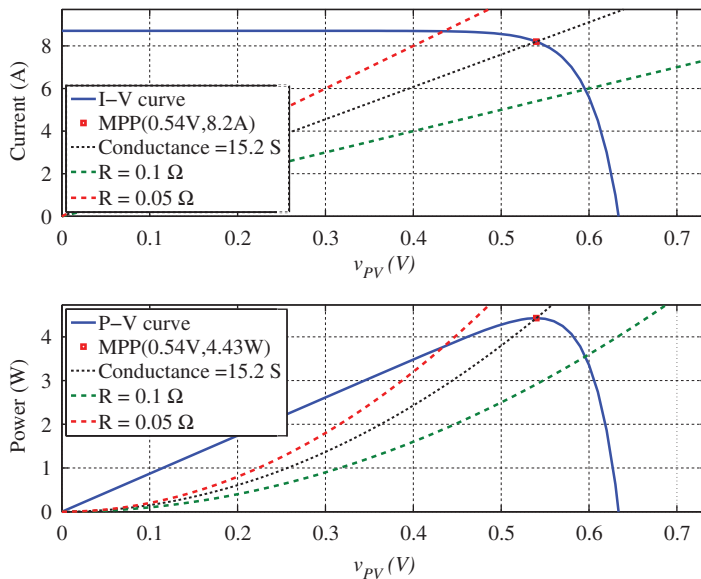


**Figure 8.1** Conductance match for maximum power point tracking: top, based on I–V curve; bottom, based on P–V curve.

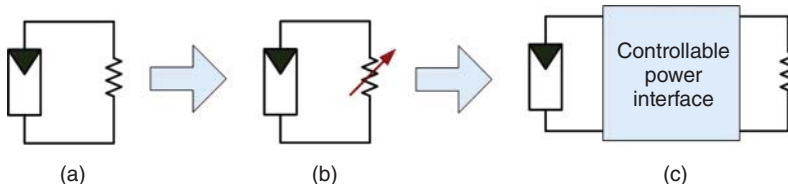


**Figure 8.2** Evolution of maximum power point tracking: (a) direct resistor match; (b) variable load match; (c) controllable power interface.

resistive load. The power converter can change the input I–V characteristics from the input to the output and give the equivalent resistance to match the MPP at the PV output terminal. This is the fundamental approach in the latest MPPT technologies.

As discussed in Section 4.1.3, the solar irradiance and cell temperature affect the MPP significantly, as illustrated in Figures 4.8 and 4.9. Dynamic tracking is required to follow unpredictable changes of environmental conditions, particularly the solar irradiance. The cell temperature usually varies with slower dynamics than the irradiance.

The diversity of materials used makes the I–V characteristics different from one PV to another, as illustrated in Figure 1.10. The fill factor (FF) is one way to describe the PV output characteristics; this was introduced in Section 1.6. It is well known that the FF values of crystalline-based PV cells are higher than those of thin-film devices. This fact should be considered to optimally specify the MPPT parameters for different PV output characteristics.

Furthermore, switching-mode power converters are widely used as the power interfaces for PV power generation. As demonstrated in Section 5.1, switching ripples at the PV output terminals make dynamic tracking difficult and reduce tracking efficiency

**Table 8.1** Loss analysis of switching-ripple voltage at the PV output terminals.

Percentage voltage ripple (%)	1.0	2.0	5.0	10.0
Percentage power loss (%)	0.03	0.11	0.70	2.99

(Xiao 2007). The power losses caused by ripple voltage in one specific crystalline-based PV module are summarized in Table 8.1. The values can be used as a reference to design the PV-side converter and the control algorithm that will prevent either significant power losses or MPPT malfunctions due to the appearance of voltage ripple. The measurement of voltage and current should be carefully designed since the value difference between the upper and lower peaks in opposite directions can result in significant errors in the measured data.

An MPPT algorithm must generally measure or estimate the PV power output and its variations. For the highest power output, the tracking function is to determine the optimal reference, which can be used as the command or reference to control the power interface. The direct command for switching-mode power converters is either the PWM duty cycle or the phase-shift angle. The reference for the MPPT operation that represents the PV output characteristics can be either the PV-link voltage or current.

The PV-link voltage is considered the most effective reference for MPPT (Xiao et al. 2007b). A feedback loop is required to regulate the PV-link voltage to follow the reference value for the highest power output. An implementation was investigated in Section 7.8 and shown as the block diagrams in Figures 7.1 and 7.2.

It is important to design a proper MPPT algorithm for the power interface in order to achieve the most effective solar energy harvesting. Various techniques have been proposed for the MPPT algorithm (Xiao 2007; Xiao et al. 2011):

- linear approximation
- heuristic search
- extreme value search
- sliding mode
- extremum-seeking control
- real-time identification
- particle swarm optimization (PSO)
- dividing rectangles (DIRECT) algorithm
- intelligent control.

The linear approximation method tries to derive a fixed percentage between the MPP and other measurable signals, such as the open-circuit voltage and short-circuit current. The linear approximation method generally leads to a simple and inexpensive implementation. They are also designed to avoid the problems caused by trial-and-error approaches, commonly referred to as “heuristic search.” Some studies have indicated that the optimal operating voltage of a PV module is always very close to a fixed percentage of the open-circuit voltage. MPPT can be achieved by using the open-circuit voltage to predict the optimal operating condition. Similarly, studies have also shown that the optimal operating current can be predicted as a fixed percentage of the short-circuit current. However, the method of linear approximation will not be discussed further

since it has been proven to be inaccurate due to the variation of PV materials and aging and temperature effects (Xiao 2007).

## 8.2 Heuristic Search

For MPPT, heuristic search is one of the most well-known algorithms thanks to its simplicity and effectiveness. The heuristic search method normally refers to the hill climbing (HC) algorithm, which is an optimization technique. The idea can be simply understood as follows: the top of a hill can be identified if the direction of movement is always up. The algorithm can be used for MPPT since the P–V curve of PV output is hill-shaped. For MPPT, an iteration is applied to change the system operating condition and then sense if the change produces increasing power output (up the hill). If so, the next increment is made in the same direction. In principle, repeating this operation will eventually lead to a maximum, which is the MPP.

The search can also be based on either the P–I curve or the curve of power versus switching duty cycle (P–D), since switching-mode converters are widely used as the PV power interface (Xiao and Dunford 2004b). The switching duty cycle is the control variable used for the majority of PV-side converters, as discussed in Section 5.1. The implementation of the HC algorithm for MPPT is illustrated in Figure 8.3.

The symbol  $x$  is the control reference, which can be either the voltage or current of the PV link, or the switching duty cycle if the P–D curve is used for the tracking. The symbol  $\Delta x$  is a constant reflecting the incremental value. The subscripts “new” and “old” are used to represent the recent and historical values of the PV output power and the control variable  $x$ . At the end of each MPPT cycle, the latest reference,  $x_{new}$ , is output for control.

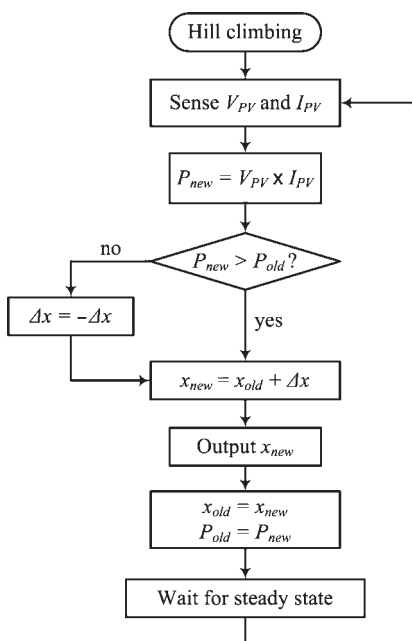


**Figure 8.3** Hill climbing algorithm for maximum power point tracking.

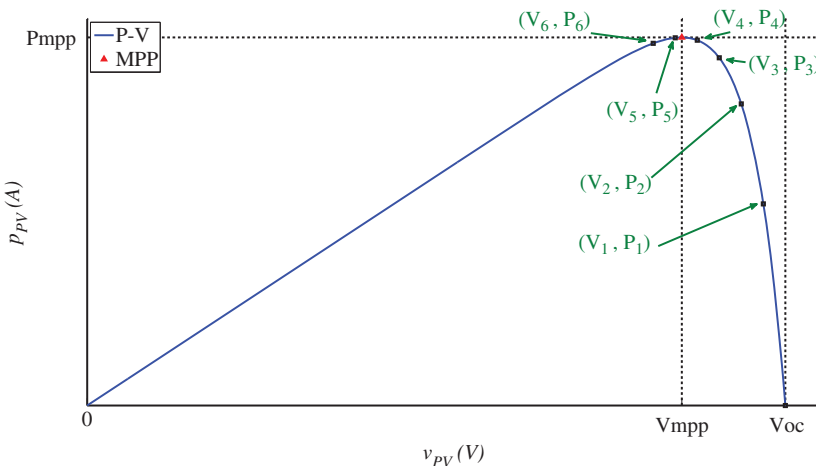


**Figure 8.4** Hill climbing based on the P–V curve.

Special attention is given to the “wait for steady state” step at the end of the MPPT loop. When a perturbation is applied, the controller should wait until the system responds and enters a steady state and then make the next measurement. This is important to avoid any misleading information during transient stages, which would cause a malfunction of the MPPT algorithm. The waiting time can be specified in the tracking frequency. The value should be determined according to the system dynamics. The system-dynamics analysis for PV-link voltage regulation was described in Chapters 6 and 7. The tracking time should always be longer than the settling time of the voltage-regulation loop so as to guarantee a stable MPPT operation.

Figure 8.4 illustrates a normalized P–V curve used to demonstrate the HC operation. The initial operation point is commonly referred to the open-circuit condition,  $V_{oc}$ , which shows no power output. When the HC algorithm starts, the new operating point ( $V_1, P_1$ ) is recognized by the MPPT algorithm. The next direction of movement is decided by the corresponding change of power level. Since the new operating point ( $V_1, P_1$ ) makes the PV modules output more power than the previous one, a relocation to ( $V_2, P_2$ ) is made by continuing in the same direction. This continues until the movement from ( $V_5, P_5$ ) to ( $V_6, P_6$ ), when the MPPT algorithm senses a reduction of the output power by comparing the values of  $P_5$  and  $P_6$ . The next direction for the operating point is to move back to ( $V_5, P_5$ ), and then ( $V_4, P_4$ ). This process continues until the operating point moves backwards and forwards around the MPP ( $V_5, P_5$ ). The illustration shows that the HC-based MPPT is capable of finding the local MPP and regulating the system around it.

In the example in Section 5.1.4, the boost topology is used as the PV-side converter (PVSC). At STC, the MPP is the operating condition when the switching duty cycle is 22.9%. The variation of the duty cycle can change the PV power output, as illustrated in Figure 8.5. The hill-shaped P–D curve suits the operation of HC-based MPPT. Following the MPPT procedure, as set out in Figure 8.3, the continuous perturbation of the duty cycle with observation of the power-change direction can identify the MPP, which is at (22.9%,  $P_{mpp}$ ). The simulation is based on the switching-mode power converter, and

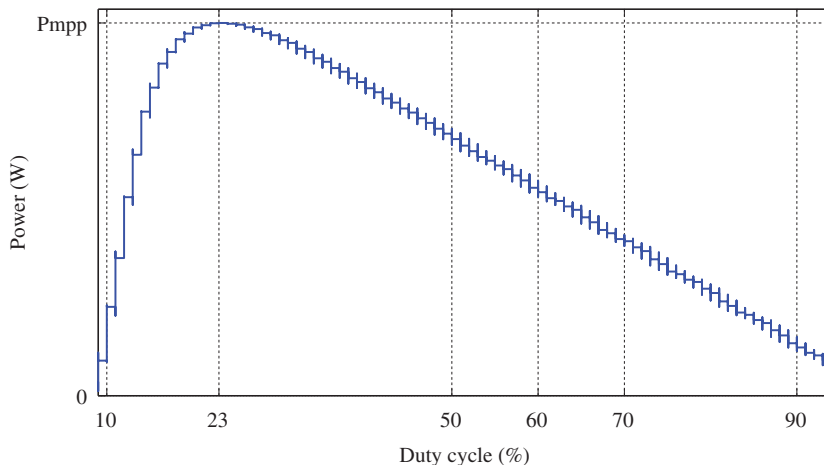


**Figure 8.5** Hill climbing based on the P–D curve.

the overshoot and undershoot are noticeable in the recorded curves, caused by the step changes of the duty cycle.

In the steady state, the tracking accuracy of HC-based MPPT is determined by the step size,  $\Delta x$ . The smaller the step size, the higher accuracy in the steady state, since the final oscillation is close to the true MPP, as marked in Figure 8.4. On the contrary, a high value of  $\Delta x$  indicates a fast tracking process, since fewer steps are required to reach the area near the MPP. Continuous perturbation and observation is generally a robust and effective way to locate the MPP in real-time, regardless of any variations of solar irradiance and cell temperature.

HC-based MPPT is commonly referred to as the method of perturbation and observation (P&O), and it is frequently discussed in the MPPT literature. It should be noted that the principle of P&O is the same as the HC algorithm; P&O is simply a dedicated term used for the MPPT algorithm in PV power systems. The HC algorithm is a generic optimal algorithm, with uses in fields other than MPPT. A perturbation is always required to run heuristic search algorithms, such as HC or P&O. The two terms are equivalent. In the following sections, only HC-based MPPT is referred to, so as to avoid confusion.

A Simulink model can be built to simulate HC-based MPPT, as shown in Figure 8.6. It can be implemented by following the flowchart in Figure 8.3. The latest measured power level  $P_{new}$  is compared with the previous measurement  $P_{old}$  to determine the sign of the next perturbation. The perturbation amplitude is implemented in the unit delay block, indicated by  $delta\text{-}x$ . The sign of  $delta\text{-}x$  is always determined by the comparison between  $P_{new}$  and  $P_{old}$ . The MPPT output is shown as  $X_{new}$  and can be either increased or decreased from the previous value,  $X_{old}$ . The tracking frequency is implemented in the three unit delay blocks using the settling of the sample time. Special attention is given that the sampling time of the unit delay blocks matches the MPPT tracking speed, which is specified by the system dynamic analysis. The sampling time for MPPT should not be confused with the sampling time for the overall system simulation.

Continuous oscillation around the MPP is an intrinsic problem of the standard HC-based MPPT algorithm (Xiao and Dunford 2004b). If the incremental step is low, it takes a long time to find the MPP initially or after a change in environmental conditions.

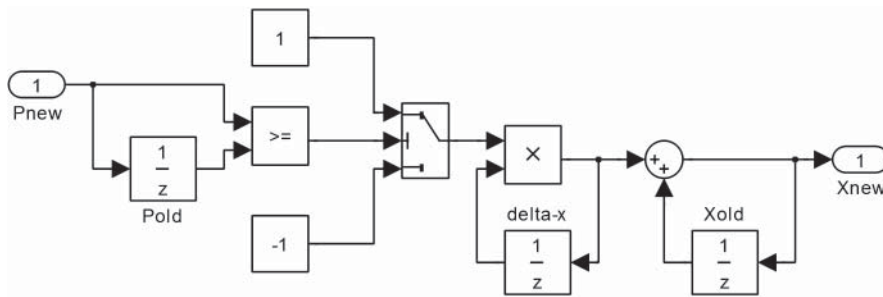


**Figure 8.6** Simulink model of the hill-climbing-based maximum power point tracking.

However, if a high value of  $\Delta x$  is used, the power fluctuation is significant around the MPP and results in energy waste, as detailed in Table 8.1. The tradeoff between tracking accuracy and speed should always be considered when a fixed value of  $\Delta x$  is used for HC-based MPPT.

### 8.3 Extreme-value Searching

One development of MPPT is based on the extreme value theorem (EVT), according to which the extremum, either maximum or minimum, occurs at a critical point, as expressed in (8.1). The critical point  $x_0$  is the local extremum found from  $y(x_0)$ , where  $y$  is a function of  $x$ . The critical point can be continuously tracked and updated to follow (8.1).

$$\left. \frac{dy(x)}{dx} \right|_{x=x_0} = 0 \quad (8.1)$$

For the PV output, the power reaches a local peak if the condition is satisfied by (8.2), which assumes that  $p_{pv}$  is a function of  $v_{pv}$ . Based on the EVT, an MPPT algorithm can be developed.

$$\left. \frac{dp_{pv}(v_{pv})}{dv_{pv}} \right|_{v_{pv}=V_{mpp}} = 0 \quad (8.2)$$

As discussed in Chapter 4, the function  $p_{pv}$  with respect to  $v_{pv}$  can be established. However, the coefficients of the function are constant only when the environmental conditions in terms of solar irradiance and cell temperature are steady. In the real world, the function is time-variant due to environment variations. Furthermore, the mathematical model coefficients of the PV cell are difficult to identify in real time.

One approach uses a numerical approach – the Euler method – to approximate the operation of the extreme value search. The approximation approach does not require a mathematical model to represent the PV output characteristics. The truncation error should be considered in the numeral differentiation, as pointed out by Xiao et al. (2007a). Therefore, the numerical differentiation can be expressed by (8.3) and (8.4), which are based on the forward Euler and backward Euler methods, respectively.

$$\left. \frac{dp_{pv}}{dv_{pv}} \right|_{V_{k-1}} = \frac{P_k - P_{k-1}}{\Delta V_k} + O(\Delta V^2) \quad (8.3)$$

where  $\Delta V_k = V_k - V_{k-1}$ .

$$\frac{dp_{pv}}{dv_{pv}} \Big|_{V_k} = \frac{P_k - P_{k-1}}{\Delta V_k} + O(\Delta V^2) \quad (8.4)$$

The expressions are represented in discrete time, where  $P_k$  and  $P_{k-1}$  are the adjacent records of the measured power, and  $V_k$  and  $V_{k-1}$  are sequential values of the measured voltage. The local truncation error for the Euler methods is equal to  $O(\Delta V^2)$ , which stands for the order of  $\Delta V$ . The expressions in both (8.3) and (8.4) indicate first-order accuracy (Xiao et al. 2007a). The local truncation error is defined to represent how well the exact solution satisfies the numerical scheme. The capital O notation is used to characterize the residual term of a truncated infinite series in mathematics. According to (8.3) and (8.4), the MPP is considered to be tracked if the condition of (8.5) is satisfied when the value of the truncation error is insignificant and  $P_k \approx P_{k-1}$ .

$$\frac{P_k - P_{k-1}}{\Delta V_k} + O(\Delta V^2) = 0 \quad (8.5)$$

Another MPPT algorithm that is frequently discussed in literature, and which is based on the EVT, is the incremental conductance method (IncCond). Its mathematical expression is

$$\frac{dp_{pv}}{dv_{pv}} = \frac{d(v_{pv})i_{pv}}{dv_{pv}} = i_{pv} + v_{pv} \frac{di_{pv}}{dv_{pv}} = 0 \quad (8.6)$$

where the differentiation is changed from  $dp/dv$  to  $di/dv$  since  $p = v \times i$ . The numerical approximation based on the Euler method is

$$I_k + V_k \frac{(I_k - I_{k-1})}{\Delta V} + O(\Delta V^2) = I_k + V_k \frac{\Delta I_k}{\Delta V_k} + O(\Delta V^2) \approx 0 \quad (8.7)$$

The IncCond method is established according to the equilibrium and is expressed as

$$-\frac{I_k}{V_k} \approx \frac{\Delta I_k}{\Delta V_k} \quad (8.8)$$

The flowchart of the IncCond algorithm is illustrated in Figure 8.7. When the condition

$$-\frac{I_k}{V_k} < \frac{\Delta I_k}{\Delta V_k} \quad (8.9)$$

is met, the current operating point is expected to be on the left-hand side of the MPP in the I–V curve. An increase of  $v_{pv}$  should be executed in order to approach the MPP. This is equivalent to the condition,  $dp/dv > 0$ . On the other hand, the algorithm sends a command to decrease  $v_{pv}$  when the equivalent condition,  $dp/dv < 0$  is detected. The perturbation that is caused by the reference change can be stopped if the equilibrium in (8.8) is satisfied according to the IncCond algorithm. This indicates that the MPP has been successfully located and that the perturbation should be stopped. This aims to eliminate a steady-state oscillation around the MPP, which is an intrinsic problem of using the HC-based MPPT algorithm.

However, there are still oscillations under stable environmental conditions when the IncCond algorithm is applied. The condition in (8.2) is seldom satisfied in practical

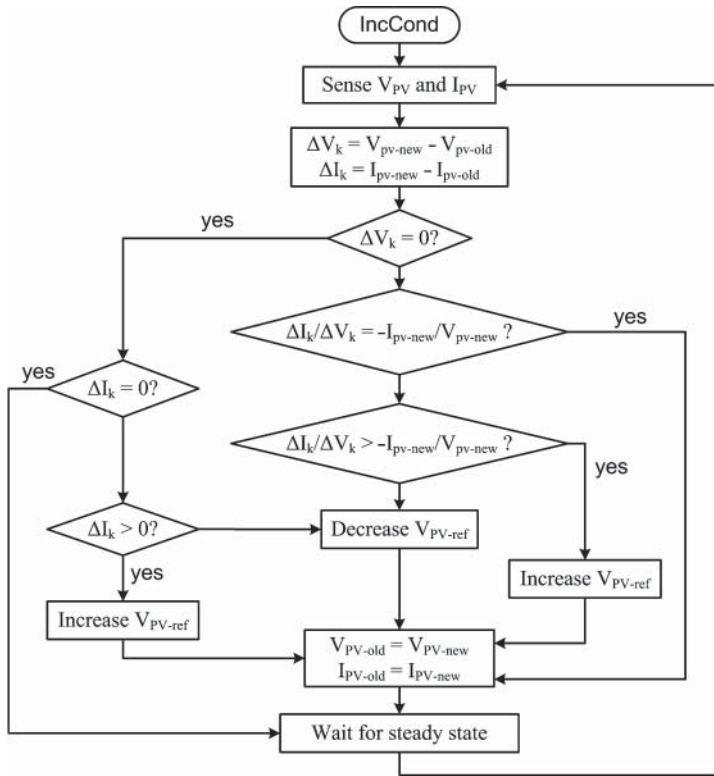


Figure 8.7 Flowchart for extreme value searching.

PV systems. The numerical approximation of the maximum power condition rarely matches the true MPP, which is represented in the continuous time by  $dP_{pv}/dv_{pv} = 0$ .

This issue, as explained by Xiao et al. (2007a), is caused by the numerical approximation. According to (8.3) and (8.4), the local truncation error of a numerical derivation is always present in Euler methods. Section 8.8 will introduce one approach for reducing the truncation error in order to improve the EVT-based MPPT algorithm.

## 8.4 Sampling Frequency and Perturbation Size

It should be noted that the MPPT implementation for both HC and EVT is based on digital control in discrete time. The flowcharts of the HC and IncCond, as shown in Figures 8.3 and 8.7, respectively, always update the control reference and indicate the waiting time for the system entering the next steady state. Therefore, one important parameter to execute the MPPT is the perturbation frequency, which is denoted as  $f_{mppt}$ . When the dynamic model is derived at the PV link, the value of  $f_{mppt}$  can be determined from the settling time of each step response. For example, if the P–D curve is used for the tracking, the dynamic model developed in Section 5.1 should be used to evaluate the settling time. If the P–V curve is applied, the system dynamics is considered using the voltage regulation loop, as described in Sections 6.3 and 7.8.

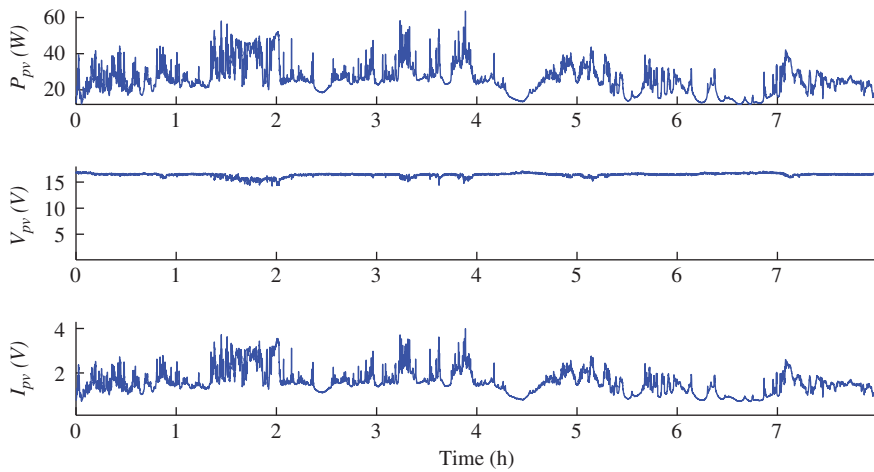


**Figure 8.8** Waveforms of PV power ( $P_{pv}$ ), voltage ( $V_{pv}$ ), and current ( $I_{pv}$ ) measured on 9 July 2006.

The perturbation size should be determined with consideration of the ripples that are caused by the switching-mode power interface. For practical applications, the signal-to-noise ratio (SNR) should be considered to avoid any misleading information for the MPPT operation. The noise and ripples in the measured signal can cause malfunctions of MPPT algorithms. The tradeoff of the tracking speed in transient states and the accuracy in steady states should also be considered.

Determining the optimal step size becomes even more difficult if weather variation patterns are considered. Figure 8.8 shows the waveform of the measured power, voltage, and current of a specific circumstance. The eight-hour test was performed in Vancouver, Canada. It is noticeable that the PV power level varies dramatically over a daily period and causes significantly fast dynamics for the MPPT algorithm. For the best energy harvesting under any specific weather conditions, the dynamic performance of MPPT should be emphasized more than the steady state. Large perturbations are expected, which allows for fast tracking of changes of the MPP.

Based on the same PV power system, Figure 8.9 shows a different example, which is a good sunny day. The PV generating power increases smoothly in the morning and decreases slowly in the afternoon. The environmental conditions become predictable. This is commonly considered as an ideal condition for energy harvesting, and the MPPT algorithm shows good performance in the steady state. Some dry areas, such as the Arabian Gulf countries, show similar patterns year round. Comparing the case studies shown in Figure 8.8 and 8.9, a single optimal value of the perturbation size is difficult to choose due to the tradeoff of the tracking speed and accuracy and the regional differences (Du et al. 2015).

## 8.5 Case Study

The buck converter used for the PV-side power interface was designed in Section 5.1.2, dynamically modeled in Section 6.3.2, and its control was described in Section 7.8.3. This example is based on the same system parameters, and will reveal the approaches

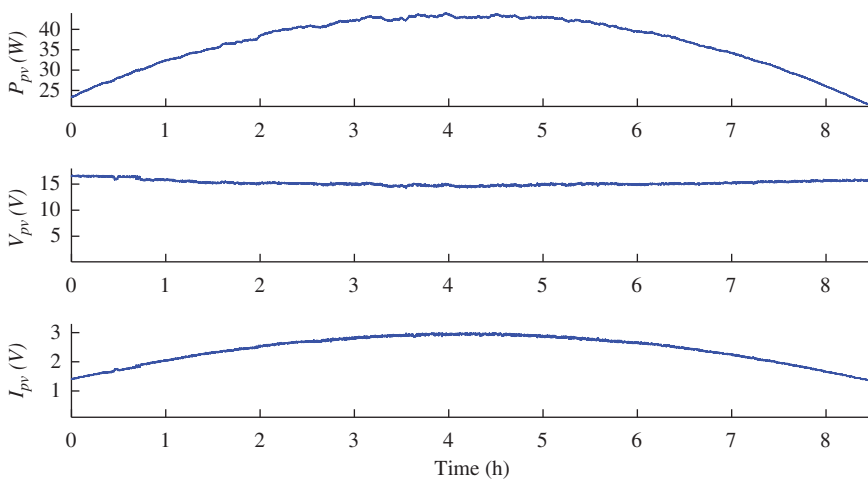


**Figure 8.9** Waveforms of PV power ( $P_{pv}$ ), voltage ( $V_{pv}$ ), and current ( $I_{pv}$ ) measured on 24 June 2006.

**Table 8.2** Dynamic analysis of the buck converter used for the PV-side power interface.

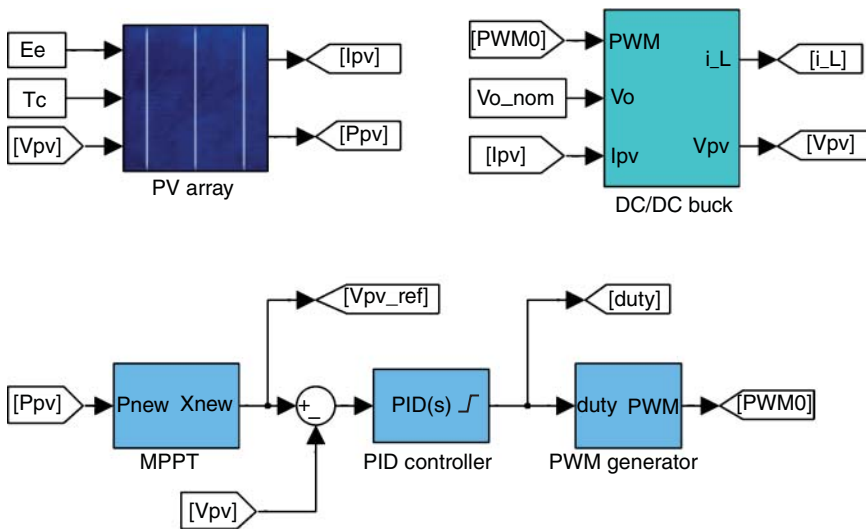
Configuration	Overshoot	Settling	Description in	Illustration
Original plant for P–D MPPT	69%	9.6 ms	Section 6.3.2	Figure 6.4
Closed-loop for P–V MPPT	$\approx 0$	1.7 ms	Section 7.8.3	Figure 7.15

to system design, modeling, and control. According to the control diagram, as shown in Figure 7.1, an MPPT block needs to be implemented. Therefore, the system dynamics should be analyzed before the design of the MPPT. The important information about the original dynamics and the closed-loop performance are summarized in Table 8.2. For this case study, the MPPT operation is based on the HC algorithm.

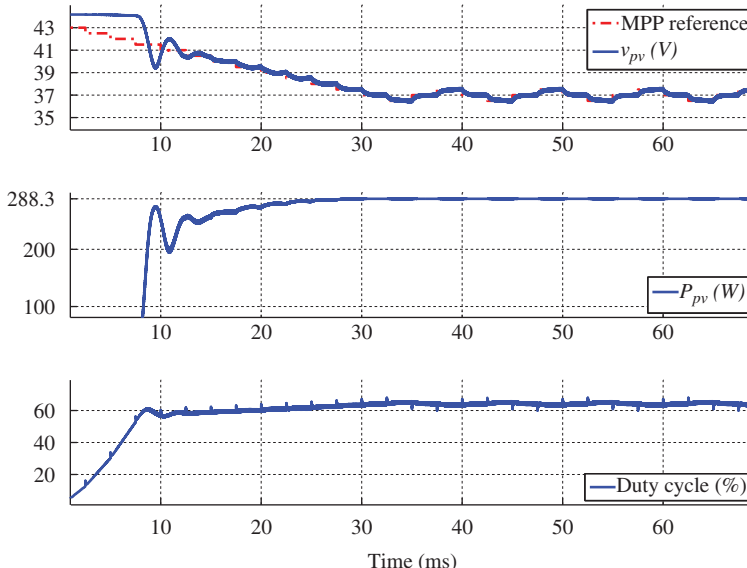
Without the voltage regulation loop, HC-based MPPT can be operated with the P–D curve, which shows the MPP with respect to the switching duty cycle. The minimal perturbation time can be determined from the settling time, which is estimated as 9.6 ms. When the voltage regulation loop is implemented, the system response is improved, with a settling time of 1.7 ms. The minimal perturbation time, which is the response of  $P_{pv}$  to a change of  $v_{pv}$ , can be selected from the settling time. With a voltage regulation loop, HC-based MPPT can operate five times faster than without.

Figure 8.10 illustrates the overall simulation model, including the blocks for the PV array and DC/DC buck converter. The control functions are the PWM signal generator, the MPPT function, and the PID controller for PV-link voltage regulation. The MPPT algorithm evaluates the power variation and decides the reference for the PV-link voltage. The voltage regulation loop follows commands in order to stay at the MPP regardless of variations of irradiance and temperature.

The MPPT sampling frequency is 400 Hz according to the settling time when the voltage regulation loop is implemented. The simulation sampling frequency 50 MHz, of which one thousand samples are filled for each switching cycle. It should not be confused by the MPPT sampling frequency.



**Figure 8.10** Simulink model of the buck converter used for PV-side power interface with MPPT.



**Figure 8.11** Simulation result of the buck converter used for PV-side power interface with MPPT.

The simulation result is shown in Figure 8.11, and includes the MPPT reference signal that is generated by the MPPT algorithm. The voltage regulation loop follows the commands to reach the MPP. After the transient stage, about 34 ms, the HC-based MPPT algorithm continues the perturbation process and maintains the operating point around the MPP. The peak power is 288.3 W. This is shown in the power waveform and agrees with the PV module specification, as shown in Figure 5.4. The switching duty cycle is the direct control variable for the DC/DC buck converter, and is also shown in Figure 8.11.

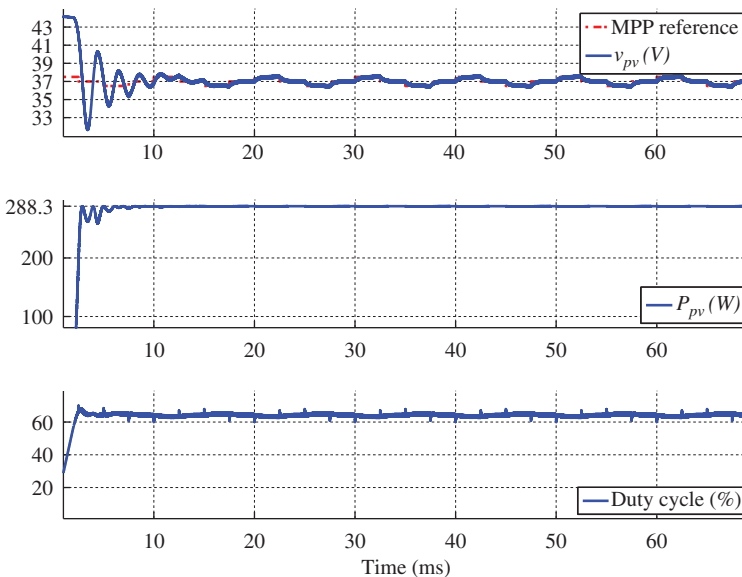


**Figure 8.12** Simulation result of the buck converter used for PV-side power interface with MPPT.

The case study demonstrates the HC-based MPPT function and shows the effectiveness of the proposed design, modeling, control, and simulation approaches.

For the regulation for the PV output voltage, the initial position of the MPP can be estimated from the open-circuit voltage, as discussed at the beginning of Chapter 7. In this case, the initial value can be set to be 38 V, which is equivalent to 85% of the open-circuit voltage. The simulation result with the implementation of the initial value is illustrated in Figure 8.12. This shows the steady state is reached for the MPP at 16 ms, in contrast to the 34 ms in Figure 8.11. This shows that an effective way to avoid long tracking times at the initial stage and demonstrates the advantage of using the voltage control loop. The PV-link voltage is a useful reference for MPPT and other purposes, since it does not vary significantly with the irradiance.

## 8.6 Start-stop Mechanism for HC-based MPPT

One drawback of HC-based MPPT is the intrinsic oscillation at the steady state, which causes energy waste. Even though the incremental conductance method is based on the extremum search theorem, it cannot completely stop oscillations in the steady state due to the truncated error of the numerical differentiation, as described in Section 8.3. One proposed solution is the start-stop mechanism (Khan and Xiao 2016). A three-point oscillation pattern can be identified in the steady state when the MPP is found, as shown in Figures 8.11 and 8.12. A detailed view of three-point oscillation is given in Figure 8.13. This includes the waveform of  $v_{pv}$  in a time series together with the P–V curve. The HC-based algorithm directs the operating point alternately to the three points, a, b, and c, which causes the steady oscillation.

The simple idea proposed is to stop the active tracking when the three-point oscillation pattern is identified. Two operation modes are defined: one is called

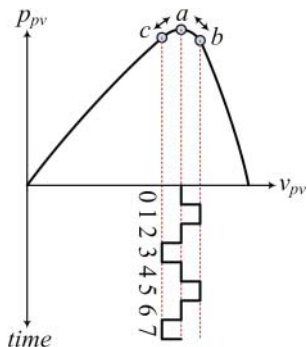


Figure 8.13 Three-point oscillation caused by HC-based MPPT.

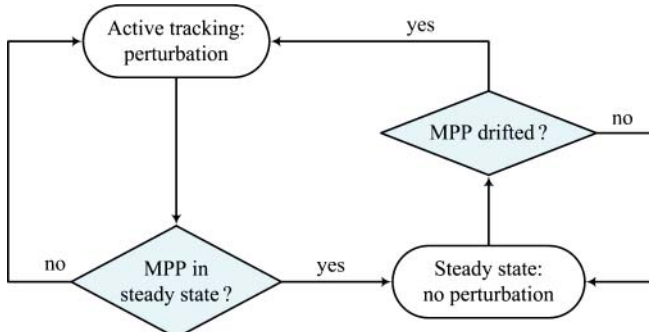


Figure 8.14 Flowchart of the start-stop mechanism for hill-climbing operation.

“active tracking” and the other is the “steady state,” as shown in Figure 8.14. The HC algorithm represents the active tracking mode, comparing the power variation and the perturbation direction. The steady-state operating mode stops the perturbation and maintains a constant reference for system regulation. PV-link voltage regulation is commonly used to maintain the steady state. The system status is continuously evaluated to detect if the MPP has changed, something that is commonly caused by a variation of environmental conditions. When this is confirmed, active tracking is reactivated until a new steady-state MPP is identified.

The oscillation pattern can be recognized when the perturbation is around the MPP. The perturbation direction changes every two cycles. This phenomenon can be expressed as

$$\Delta V_k = -\Delta V_{k-2} \quad (8.10)$$

where the perturbation step of the HC algorithm is defined as  $\Delta V_k$ , where the  $k$  shows the data sequence in discrete time.

Figure 8.13 illustrates that the step sign is positive at the moment 1, but it is negative at moment 3. The sign is negative at moment 3, but it becomes positive at moment 5. The condition holds true repeatedly in the steady state and shows the three-point oscillation pattern. Therefore, the steady state around the MPP can be identified when three of four consecutive sampling cycles satisfy the condition of (8.10). For robust operation in a practical implementation, it is recommended to look at more than ten cycles before a stop decision is made.

When the perturbation is stopped, the system is controlled in the steady-state mode since the MPP has been found. The PV voltage is regulated to a constant value, which represents the MPP. The output power is continuously sensed and monitored during the steady-state operation. When the power level detected is different from the reference value, the MPP is considered to have drifted to a new value due to environmental variation. The active tracking via the HC algorithm should be activated again to find the new MPP. The start-stop mechanism formed in this way avoids the oscillation problem typical of the HC-based MPPT method.

To evaluate the effectiveness of the start-stop mechanism, a simulation based on the case discussed in Section 8.5 is conducted. A Simulink model is built to combine the start-stop mechanism with HC-based MPPT, as shown in Figure 8.15. Based on the measured power from the PV output, P&O can be conducted and compared with the historical value. The active tracking is implemented in the perturbation block, which is the standard format of the HC algorithm.

The start-stop mechanism estimates the condition and decides to pass the perturbation or stop it. When the steady state is detected, the perturbation signal is assigned to zero in order to stop the perturbation. Otherwise, it follows the output of the perturbation block. The signal shown as  $X_{new}$  is the control output from the MPPT block, which is updated from the historic value,  $X_{old}$ . The signal represents the PV output voltage reference for the voltage feedback loop when the P–V curve is used for MPPT. The signal can also be the direct control signal, the switching duty cycle for the power interface, when the P–D curve, as illustrated in Figure 8.5, is applied for MPPT.

Figure 8.16 illustrates the Simulink implementation of the start-stop mechanism. Its inputs are the perturbation signal from the perturbation block and the latest power measurement. The status symbol “mode,” commands active tracking if the value is 1. A value of 0 leads to the stop mode, which sets the signal  $\Delta_x$  to zero. The three-point pattern is detected by evaluating (8.10). When the three-point pattern is clearly recognized over a number of cycles, the stop mode commences and the value of PV output power is recorded as the benchmark. The cycle limit is implemented inside the relay block; it is assigned a value of 11 in this case study.

When the system enters the stop mode, the benchmark value is continuously compared with the new measurement of the PV output power. When the difference becomes significant, the mechanism is reset to pass the perturbation and perform active HC tracking. In this case study, the threshold is assigned a value of 3 W. In general, the start-stop mechanism performs the function of evaluation and decision as illustrated in Figures 8.14 and 8.15.

The simulation results are illustrated in Figure 8.17, which includes the waveforms of  $v_{pv}$ ,  $p_{pv}$ , and the switching duty cycle. When the three-point condition, as expressed

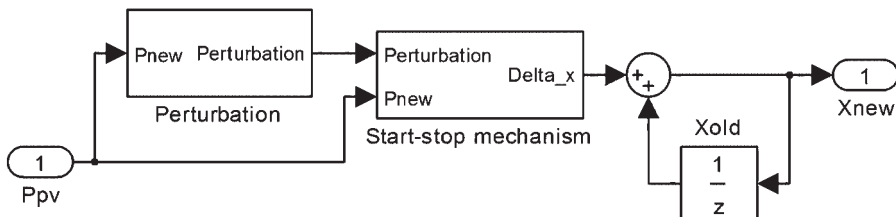


**Figure 8.15** Simulink model for integration of start-stop mechanism with HC-based MPPT.

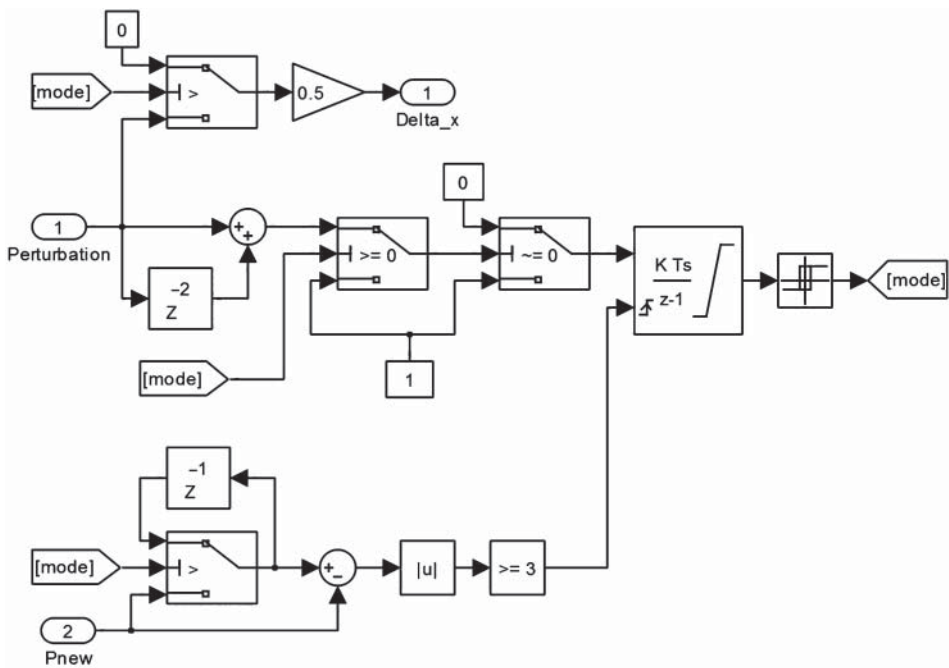


Figure 8.16 Simulink model of the start-stop mechanism.

in (8.10), is satisfied for 11 cycles consecutively, the perturbation is stopped from the MPPT block output, as shown at 33 ms. The voltage of the MPP is determined to be 37 V and is kept steady. A step change of the irradiance from  $1000 \text{ W/m}^2$  to  $500 \text{ W/m}^2$  is applied at 60 ms. The power variation triggers the active tracking mode to restart, the assumption being that the MPP has drifted to a new value. The active tracking locates the new MPP. After the condition of (8.10) is satisfied over 11 cycles, the perturbation operation is stopped again at 93 ms. The voltage of the new MPP is determined to be 36 V and is the system is then kept steady in this state. The start-stop mechanism has been proven to be a simple and effective way to avoid oscillations in the steady state and to improve the MPPT performance (Khan and Xiao 2016). The effectiveness and improvement can be demonstrated by comparing the simulation results in Figures 8.12 and 8.17.

## 8.7 Adaptive Step Size Based on the Steepest Descent

Another idea has been proposed to target the drawbacks of HC-based algorithms. This is called the adaptive HC method, and involves dynamic adjustment of the perturbation size (Xiao and Dunford 2004b). When there is an oscillation pattern during MPPT, it is ideal to make the perturbation size significant during the transient stage, but to assign it a low value when the steady state is reached for the MPP.

An optimization method can again be used to achieve the target. One algorithm is the steepest descent method, which is designed to find the nearest local minimum. The same principle can be applied to find the local maximum value – the MPP – when the gradient

Even though the mismatch condition prevents a centralized control system from delivering the highest amount of solar energy, significant research has been conducted to minimize the impact. The MPPT algorithm tries to find the optimal operating point, namely the global maximum power point (GMPP). For example, the case study in Section 2.2.1 shows two power peaks, one higher than the other under shading conditions. The highest point is considered the GMPP, giving the highest power output under the mismatch circumstance. Since partial shading is the main cause of such multi-peak phenomena, MPPT research mainly focuses on tracking the global peak instead of any local ones. The approach is commonly referred to as global maximum power point tracking (GMPPT).

Since MPPT algorithms are amenable optimization techniques, the particle swarm optimization (PSO) approach has been proposed for finding the GMPP under partial shading conditions. The method was originally developed in computer science, where it is treated as a multi-variable or multi-agent problem. For GMPPT, the PV array power is defined as the objective function. It is influenced by the voltage of the individual PV modules which are the agents. The agents share information with each other, leading to a unique peak in multidimensional space. Similar to the concept of hill climbing, the PSO can be considered an advanced iterative approach to manage all the agents so that they converge to the position corresponding to the global extremum. Although research has proven the effectiveness of PSO and other optimization techniques for GMPPT, practical implementation is difficult since it sensitive to the initial conditions and other settings. Considering the time-variant nature of PV power generation, practical applications are even more difficult since stability cannot always be proven under various disturbance conditions (Xiao et al. 2011).

## 8.12 Performance Evaluation of MPPT

The objective of the MPPT has been clearly defined as to extract the highest solar power output from each PV cell at any moment. An number of MPPT algorithms have been recently proposed to give performance superior to previous solutions. It is very important to develop a platform for fair comparison. However, comparisons are difficult since solar irradiance and ambient temperature are not controllable and not repeatable (Xiao et al. 2013).

### 8.12.1 Review of Indoor Test Environment

In the past, many MPPT algorithms were tested indoors. In general, with the controllable energy sources, the performance comparison of MPPT can be planned and scheduled to give a fair comparison. Based on previous studies (Xiao 2003; Xiao and Dunford 2004a), the indoor testing methods are summarized and described in the following.

#### 1) Computer simulation

- Always effective to quickly prove the design concept.
- Low cost and very flexible, allowing variation of environment, loads, and grid.
- Cannot be used to prove MPPT performance on its own.
- Should not be confused that the hardware-in-the-loop (HIL) techniques, which are considered a simulation approach, but include some real system components.

- HIL simulation output is sometimes considered an experimental result since the HIL platform can interface with analog signals for instruments such as oscilloscopes. It should be clearly noted that the HIL system is a simulation-based platform, not an experimental one.
- 2) PV array simulator
- Defined as a DC power supply which is programmable to simulate PV output characteristics (see Section 1.7).
  - Considered a moderate-cost and flexible solution for repeatable indoor tests of power-conditioning circuits and control algorithms.
  - The simulator can be flexibly programmed to represent different types of PV generators and different environmental variations.
  - The PV array simulator is a power electronic device.
  - It shares the same drawbacks as other switching-mode power supply systems, such as ripple in the current and voltage waveforms.
  - It might show self-resonance when connected to another power converter.
  - The output characteristics of PV arrays can change very quickly in response to variations in operating conditions.
  - The PV array simulator generally shows much slower responses than real PV material.
  - The constraint of dynamic response, which does not match real PV modules, should always be considered when it is used to validate fast MPPT algorithms.
- 3) Artificial light and temperature test chamber
- Fully controlled environment using artificial lights can provide variable irradiance levels and regulated ambient temperature for indoor testing and evaluation.
  - Could be one of the most expensive solutions since a solar simulator with accurate solar spectrum is generally expensive and limited to small scale.
  - Difficult to test a system with significant power capacity due to the high cost of artificial light and high power consumption.
  - Furthermore, it is also a high cost to maintain chamber at constant temperature for different tests since self-heating always happens when PV modules are exposed to light.

### 8.12.2 Review of Outdoor Test Environments

Outdoor evaluations have great advantages since the actual MPPT behavior can be examined using real PV arrays and natural sunlight in order to avoid unrealistic effects of artificial sunlight and power electronic simulators. Furthermore, an effective MPPT algorithm performs well in real-world weather conditions rather than any pre-assumed condition. However, the accurate measurement of solar irradiance and cell temperature is difficult. Some tests intentionally choose sunny days with the assumption that the weather pattern would be repeatable. In the past, many MPPT algorithms were tested outdoors. The methods used are outlined in the following list.

- 1) Periodical interrupt method
- Uses natural sunlight, which is better than artificial light.
  - Divides the testing period into small time pieces for different MPPT algorithms.
  - Usually stops one test and starts another with the assumption that the environmental condition is steady for all tests.

- Errors can be expected due to the time-variant patterns of irradiance and temperature.
  - Impossible to test fast MPPT dynamics in response to conditions such as moving clouds.
- 2) Day-by-day test based on single PV system
- Aims for a long-term test to evaluate the MPPT performance in response to different weather conditions.
  - A comprehensive statistical analysis is required to identify the MPPT performance, since the day-to-day weather conditions are not repeatable when the variation of both irradiance and temperature are considered.
  - The drawback lies in the long test period and the complication of statistics to prove that one MPPT algorithm is more effective than another.
- 3) Day-by-day testing on multiple parallel PV systems
- Based on at least two PV systems that are identical and installed in the same condition.
  - One can be used as the benchmark for the power output comparison.
  - The two systems should be calibrated under identical conditions in order to identify any mismatches between them due to non-ideal factors in the system components.
  - The test requires multi-day evaluation and statistical analysis to identify the performance of the MPPT since no two systems are exactly identical when component tolerances are considered.
  - The approach is considered the most comprehensive evaluation method since both systems are under the same operating conditions for a long-term test.
  - Both the MPPT dynamics and steady state can be revealed for the highest power generation.

By comparing the three testing methods in natural sunlight, it has been observed that the parallel PV system is the most effective testing platform for MPPT evaluation (Xiao et al. 2013).

### 8.12.3 Recommended Test Benches for MPPT Evaluation

Results for two different weather patterns have been reported by Xiao et al. (2013), as shown in Figures 8.8 and 8.9. A fair comparison of one day's performance of a PV system against another is impossible since the weather pattern is not repeatable day by day. The results will be inaccurate when one PV system is used to test MPPT performance on different days. Therefore, the following introduction is based on a parallel testing configuration, with two independent PV systems tested and evaluated simultaneously under the same operation conditions and in the same natural environment.

The first test bench system we will consider is recommended for evaluating the MPPT algorithms that are usually used in DC microgrids or two-stage conversion systems. The system diagram is shown in Figure 8.29. The system is formed by a programmable DC electronic load and parallel PV power systems. The MPPT algorithms are implemented to control the two DC/DC conversion units. One can be used as the benchmark; the other can be implemented with an advanced MPPT algorithm in order to prove its effectiveness. The voltage and current at the PV and DC links should be continuously measured and recorded by a data acquisition system to assess the long-term operation.

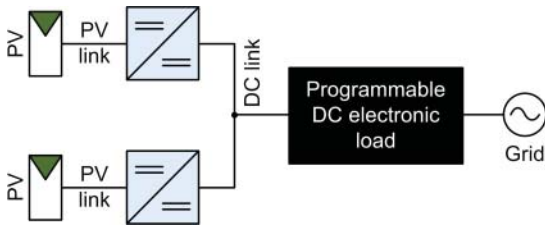


**Figure 8.29** Test bench system for evaluating MPPT in DC microgrids and two-stage conversion systems.

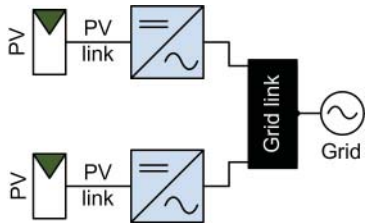


**Figure 8.30** Test bench system for evaluating MPPT in single-stage DC/AC conversion systems.

The programmable DC electronic load can create a DC link with constant voltage, which is shared by the two PV systems. It is flexible and can be programmed to have other functions, such as voltage disturbance. It should be noted that the majority of programmable DC electronic loads do not inject power into an AC grid. The grid connection is mainly for the ancillary power supply to control the load system. Depending on the application, the PV and DC/DC units can be as small as a single PV module or as large as a PV array. The PV string and array levels are important in testing the MPPT performance in response to partial shading or other mismatch conditions.

The second test bench system is used to evaluate MPPT algorithms for single-stage DC/AC conversion systems. The system diagram is shown in Figure 8.30. The system is connected to the grid directly. The test bench is especially important in testing MPPT performance for single-phase grid interconnections. The single-phase connection introduces significant double-line frequency ripples at the PV link, which limit the MPPT performance. The MPPT algorithms should be independently implemented in the two DC/AC conversion units. One can be used as the benchmark, and the other can implement an advanced MPPT algorithm for improved performance. The voltage and current at the PV link and grid link should also be recorded to enable day-by-day operation to be assessed.

#### 8.12.4 Statistical Paired Differential Evaluation

The test systems in Figures 8.29 and 8.30 are flexible enough to test MPPT performance over any time period, from several days to several years. The comparison assumes that the parallel systems are identical. However, all PV panel manufacturers state power output tolerances ranging from  $\pm 1\%$  to  $\pm 5\%$ . One example was discussed in Section 2.2.1 and illustrated in Figure 2.8. Even though the PV modules are the same model and were manufactured on the same date, the output characteristics are slightly different under identical test conditions. Furthermore, the components that form the DC/DC and DC/AC power converters are often non-ideal. The uncertainty in the parallel systems might therefore dominate the system output, defeating the attempt to make a meaningful performance comparison and leading to a wrong conclusion.

A calibration test should be always conducted using the same MPPT algorithm. The long-term output result reveals any differences between the two independent systems. In addition, the hardware systems can be alternated, swapping the control algorithms in order to minimize any initial mismatch effect. When a significant quantity of data has been collected, paired difference tests can be used to assess the significance of the difference between the two sets of data that are produced by the system power output (Xiao et al. 2013). The paired *t*-test is used to distinguish the performance of the MPPT algorithms. The *t*-statistic is expressed as

$$t = \frac{\overline{P}_1 - \overline{P}_2}{s_{\overline{P}_1 - \overline{P}_2}} \quad (8.32)$$

where  $\overline{P}_1$  and  $\overline{P}_2$  are the mean values of the two system power outputs. The  $s_{\overline{P}_1 - \overline{P}_2}$  is the standard error of the difference between the two datasets. The *t*-statistic has a zero-mean-normalized probability distribution function that is dependent on the number of points in the datasets.

Values of *t* that lie outside approximately two standard deviations of the mean (zero) are termed 95% confidence intervals, and are usually used in statistical inference as a measure of testing whether a certain parameter is significantly different from a certain hypothesized value. The correctness of the hypothesized value is called the null hypothesis. If the value of *t* obtained is significantly far from that value (formally outside 95% on the probability distribution), then the null hypothesis can be rejected, and it is safe to conclude that the experimentally obtained quantity is not equal to the hypothesized value with 95% confidence. The null hypothesis indicates that there is no difference between the power outputs obtained by the experimental test. It can be statistically stated as the difference between the two means being equal to zero. If the *t*-value obtained from (8.32) is significantly different from zero, then it can be inferred that the difference between the power outputs of the two methods is statistically significant.

The statistics toolbox of Matlab provides a function for the paired *t*-test. It is provided as the function *t-test(x, y)*, where *x* and *y* represent the random samples following a normal distribution. *x* and *y* must be vectors of the same length. The function can be used to conduct the *t*-test and assess the null hypothesis. If the result of the test returns 1, the *t-test* indicates a rejection of the null hypothesis at the 95% confidence level. A returned value of 0 indicates a failure to reject the null hypothesis at the 95% confidence level.

## 8.13 Summary

For MPPT, hill climbing (HC) methods are widely used. An alternative name for this approach is perturbation and observation (P&O). The standard algorithm generally involves a tradeoff between the tracking speed and the magnitude of steady-state oscillations. The selection of the perturbation size is considered a dilemma in balancing these requirements.

The incremental conductance method (IncCond) was developed to solve the problems of the HC-based MPPT approaches. It is based on the extremum value theorem (EVT), seeking to locate the local extremum value, either maximum or minimum.

The mathematical operation of differentiation is required. However, the function of the PV output power output is not exactly known to the controller since the parameters significantly change with environmental conditions. Instead, the IncCond operation relies on a numerical approximation of the differentiation, which introduces a truncated error. Therefore, experiments show that the oscillations in the steady state cannot be removed by the IncCond method. The truncated errors of the numerical approximation mean that the IncCond operation is not a significant advance on HC-based algorithms.

It is important to choose carefully the sampling frequency and perturbation size in HC-based or EVT-based MPPT algorithms. These parameters drive the response speed and steady-state performance. The sampling frequency can be determined by system dynamic analysis, ideas introduced in Sections 6.3 and 7.8 respectively. With a dedicated voltage-regulation loop for the PV link, the system dynamics can be improved, benefiting MPPT performance. The perturbation size should be determined through consideration of the ripple that is caused by the switching-mode power interface. For practical applications, the SNR should always be investigated to decide the size. Additionally, weather variation patterns must be considered on a case-by-case basis.

A start-stop mechanism can be integrated with a conventional HC-based MPPT algorithm, bringing the advantages of simplicity and effectiveness. It can give oscillation-free operation in the steady state since unnecessary perturbations can be avoided. When the MPP changes, active perturbations can be restarted to locate the new MPP. The implementation is relatively easy and straightforward and is an ideal complement to conventional HC-based MPPT algorithms.

The step size in active tracking can be adaptively adjusted to give fast tracking in transient conditions, and low steady-state errors. In theory, this is an ideal solution since many mathematical methods can be used to drive the adaptations. The common algorithms used are the steepest decent method and the Newton–Raphson method. However, practical implementations can be difficult because the mathematical model to represent the real-time PV output characteristics is missing. When making numerical approximations of the differentiation, truncated errors have been reported when using Euler methods. It turns out that the MPP cannot be fully represented when using a numerical assumption of  $\Delta P/\Delta V \approx 0$ .

Centered differentiation has been introduced to minimize truncated errors and improve the approximation accuracy of the condition  $dp/dv = 0$ . One additional measurement is required to perform centered differentiation. Improved performance has been reported when centered differentiation is integrated with the steepest descent algorithm and the dedicated start-stop mechanism. Overall, the implementation is more complicated than using only the HC algorithm and the simple start-stop mechanism.

The real-time identification method is another MPPT approach, which utilizes a mathematical model that is constructed using polynomial equations. The parameters are identified by recursive least squares (RLS) estimation in real time, so as to follow variations in operation conditions. The Newton–Raphson method is used as the numerical solver to find the PV-link voltage, which represents the MPP. The approach is model-based and does not require a numerical differentiation used in EVT-based algorithms or the perturbation in HC-based algorithms. However, practical implementation can be difficult due to the significant computation demand required for system identification. Furthermore, the stability of the RLS solution is another concern.

Extremum seeking (ES) control is another optimization approach for MPPT, which does not require prior knowledge of the system model. The standard method injects an sinusoidal excitation signal into the control loop in order to identify the extremum point. Its effectiveness was demonstrated by simulation in this chapter. Since switching-mode power converters are commonly used for PV systems, the ES algorithm can also utilize the switching ripple as the excitation signal. However, the implementation is not as straightforward as the HC and simple start-stop mechanisms. The tracking performance has not been shown to be significantly better than others.

In general, the MPPT algorithm is not as effective in dealing with PV mismatch conditions in CMPPT systems as in DMPPT systems, even though there has been significant research and many publications in the area. The complication of mismatch conditions in PV arrays creates a problem that is difficult to solve quickly for practical applications. Up to now, a DMPPT configuration has been the most effective way to minimize power degradation when there are mismatch conditions among PV cells.

Even though significant research has been published, many of the studies involved did not provide a fair comparison to demonstrate MPPT effectiveness. An outdoor test with natural sunlight is considered the ideal condition for evaluating MPPT effectiveness. However, a fair comparison of different MPPT methods is not easy outdoors. First, the true MPP is unknown when a PV system is in uninterrupted operation. The weather conditions – irradiance and temperature – are not repeatable. It is important to create a practical bench test system to evaluate MPPT performance under identical operating conditions.

A parallel testing system using two independent PV systems is highly recommended in this chapter. However, it is impossible to construct two truly identical systems when the difference between solar modules and other non-ideal factors in the power-conditioning circuits are considered. A pairwise difference comparison is introduced in order to statistically distinguish energy harvesting efficiency of two MPPT algorithms regardless of non-ideal factors. The pairwise *t*-test formula can be applied to filter out the effect of the difference in PV panel outputs, to enable accurate quantification of the statistical significance between two MPPT methods. The proposed method is considered as a systematic approach for both short-term and long-term side-by-side comparisons of MPPT performance using natural sunlight.

## Problems

- 8.1** Readers are encouraged to research other MPPT algorithms that have not been covered in this chapter. Compare them with the solutions presented in this book and provide comment about their pros and cons.
- 8.2** Use any available simulation tool, construct an MPPT block based on the HC algorithm.
- 8.3** Based on the developed MPPT model, implement the start-stop mechanism.
- 8.4** Based on an example, compare the performance with and without the start-stop mechanism. The comparison can be based on the produced energy within a predefined time period.

**9**

## Battery Storage and Standalone System Design

A standalone system supplies electric power independent of an electrical distribution network. Such systems can be generally classified into two categories: those with or without significant storage, as shown in Figure 9.1.

Systems without bulk energy storage can be direct-coupled, power-conditioned or hybrid, the configurations of which are shown in Figure 9.2. The diagrams provide a basic representation, but practical systems are more complex than shown.

Direct-coupled systems are the simplest PV applications, designed to match the PV output to the load, as shown in Figure 9.2a. They are commonly used for ventilation fans and water pumps for irrigation, and so on. In most systems, control circuits are implemented to switch on and off the connection depending on the voltage the PV output, which is an indicator of the available solar power. Such systems are incapable of accurate MPPT due to their lack of power conditioning.

All direct-coupled systems can be modified to incorporate a power-conditioning unit to enhance control. Such a system is shown in Figure 9.2b, with a power conditioner included between the PV generator and the load. Power conditioning is very effective for a PV system without significant energy storage. The MPPT function can be used to maximize the PV output regardless of environmental variations. The power interface can also be controlled to meet specific load requirements, such as a constant voltage supply.

A hybrid system usually uses a conventional engine-based generator in parallel with the PV power source. Both share the same distribution channel to the common load, as shown in Figure 9.2c. The DC/AC converter produces AC power from the PV source and supplies the load through the distribution network. The PV power contribution can reduce the power generation required from the generator, resulting in a fuel saving. The PV system is usually controlled through MPPT to yield the highest solar energy harvest.

Even though the diagram in Figure 9.2c shows only one motor generator, the system can be composed of multiple generation units in parallel connection. For the best fuel-saving performance, communication is generally required to coordinate the PV output with the engine-based generators. Coordination is important when the PV power penetration becomes significant, say more than 25%. When multiple motor generators are available in a standalone system, the system can be optimized to improve efficiency. For example, running two generators each at 50% of capacity is generally more fuel efficient than operating four, each at 25% of capacity. Using real-time measurements of the load condition and PV generation, the centralized coordinator can schedule the overall generation facilities in an economical way, so as to give the best performance in terms of system efficiency and fuel saving.

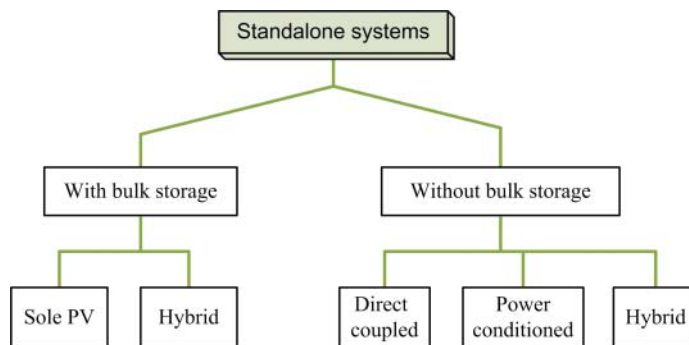


Figure 9.1 General classification of standalone PV systems.

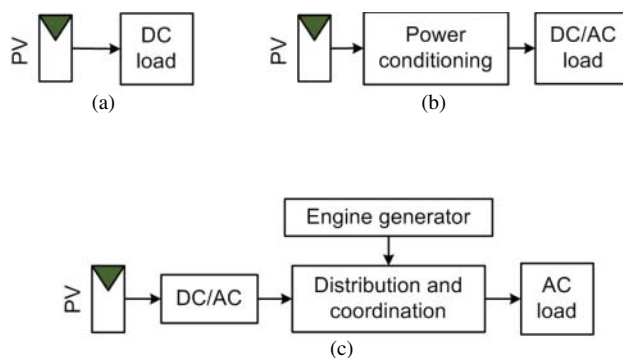


Figure 9.2 Standalone systems without bulk energy storage: (a) direct-coupled; (b) with power conditioning; (c) hybrid solution.

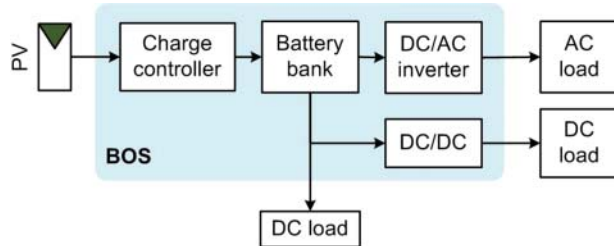
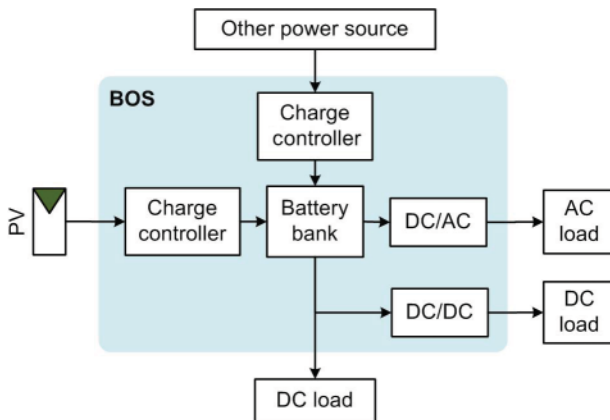


Figure 9.3 Standalone PV system with bulk energy storage.

A steady power supply is demanded by loads in the majority of standalone systems. As discussed in Section 1.9, bulk energy storage – mainly rechargeable batteries – is generally required to mitigate the intermittency of solar energy. Systems with bulk energy storage, can be divided into two groups: standalone PV and hybrid. These are shown in Figures 9.3 and 9.4, respectively. It should be noted that the diagrams are general representations, since practical systems may be more complex. Furthermore, overcurrent protection (OCP) is mandatory for any system with battery storage, even though no protection circuits are shown in the diagrams.



**Figure 9.4** Hybrid system including PV and bulk energy storage.

As shown in Figure 9.3, the battery charging cycles should be properly maintained by the charge controller with integration of MPPT to give the highest solar energy harvest. Any extra PV power bypasses the battery buffer and supplies the loads directly. The battery bank forms an unregulated DC bus since the voltage varies by up to  $\pm 20\%$  from the nominal voltage according to the state of charge. The unregulated bus can directly supply DC loads if they are insensitive to voltage variation. A DC/DC converter should be implemented to regulate the output voltage and supply the dedicated load if constant DC voltages at different levels are required. When AC loads are present, DC/AC conversion should be used to convert from the unregulated DC bus to AC.

A hybrid system involves use of additional power sources alongside the PV generator, as shown Figure 9.4. Additional power can come from wind turbines, fuel cells, or conventional engine-based generators. Such a system can balance the battery charge and the power from PV or other power sources since multiple charge controllers are included. The coordination can be achieved using a centralized controller or a distributed sharing algorithm implemented in each charge controller. PV power generation is expected to use MPPT to give the highest clean energy contribution. There is also an option for fuel-based power sources to bypass the battery and supply the load directly, although this configuration is not shown in Figure 9.4. A direct connection can minimize power losses in the conversion stages.

## 9.1 Batteries

A rechargeable battery is defined as an energy storage device that converts chemical energy into electrical energy and vice versa. People are tending to use more and more rechargeable batteries instead of the disposable counterparts due to cost savings and environmental concerns. Due to the bulk energy storage requirement in standalone PV systems, it is important to understand the different battery technologies and to select one accordingly. Battery cells are the basic electrochemical units that form a battery module and pack, as shown in Figure 9.5. A large battery power system is usually constructed from battery banks. When the battery system becomes more and more

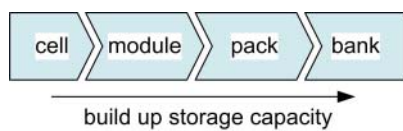


**Figure 9.5** Formation of battery power systems from cell to bank.

complicated and powerful, special attention should always be given to incorporate protection devices for safety purposes. For portable devices such as cell phones a single battery cell can be used.

It should be noted that all batteries exhibit self-discharge, the rate depending on the battery type and temperature. Furthermore, all batteries have a limited cycle life, their lifetime depending on the battery type, the conditions of charge and discharge, the temperature, and other conditions of use.

### 9.1.1 Battery Types

Common rechargeable batteries are based on lead, nickel, lithium, or sodium. It is important to understand the cell nominal voltage and characteristics and to select the correct type for the given application.

#### Lead-based batteries

Lead-based battery technology is mature and therefore low-cost and reliable. This is the main reason that lead-based batteries are still widely used for vehicles and back-up energy storage. They are often referred to as “lead-acid” batteries, because dilute sulfuric acid and lead are used for the electrolyte and plate, respectively. Table 9.1 summarizes the common terms and basic characteristics of lead-acid batteries. Two main categories can be considered: flooded and sealed. Because of their advantages of safety and low maintenance requirement, more and more applications are using sealed modules instead of the old flooded type. Sealed modules also include the VRLA, AGM, and gel types, which are described in the table.

The battery module, typically rated at either 12 V or 6 V, is built from lead-acid cells with a nominal voltage of 2 V. Lead-acid batteries can also be classified in another way:

**Table 9.1** Common lead-acid battery types.

Type	Description
Flooded	Old lead-acid technology with liquid electrolyte inside the cell. Regular maintenance is required by adding distilled water.
Sealed	Also called “maintenance-free” battery since the cell is sealed without water. Generally considered safer than flooded batteries.
Valve-regulated lead-acid (VRLA)	The battery module includes a valve for release of hydrogen and oxygen gasses during charging.
Absorbent glass mat (AGM)	The electrolyte is suspended in a special glass mat. High efficiency.
Gel	Contains a silica type gel to suspend the electrolyte. Does not tend to sulfate or degrade as easily as wet cells.

as starting or deep-cycle batteries. A starting battery is used to provide instant power, such as in a starter motor. Such a battery is also termed as the “cranking” type. For standalone PV systems, deep-cycle batteries are commonly used. These are built to provide continuous electric power, with high capacities and long cycle lives. The commercial term “solar batteries” often refers to deep-cycle batteries. Even though lead-acid batteries are still widely used in renewable energy systems, the following drawbacks lead to the use of other battery technologies:

- low energy capacity density per unit volume
- low energy capacity density per unit weight
- slow charge speed
- limited cycle life.

### Nickel-based batteries

The common types of nickel-based batteries are summarized in Table 9.2. Nickel–metal-hydride (NiMH) batteries were introduced in 1992 and are commonly used in low-cost consumer products (Powers 2000). The battery is composed of nickel hydroxide and a hydrogen-absorbing alloy. Most rechargeable NiMH batteries follow the American National Standards Institute (ANSI) standard, and are sized as A, AA, or AAA. A standard AA size cell typically has a capacity of 1800–2500 mAh. The cylindrical forms are available to replace primary batteries, which are not rechargeable. The hydrogen-absorbing alloy is capable of absorbing and releasing hydrogen at a higher density level than the cadmium compound used in nickel–cadmium (NiCd) batteries. One important application of NiMH technology is in the hybrid vehicle, the Toyota Prius. According to a report from the National Renewable Energy Laboratory of the USA (Kelly et al. 2002), the battery system is designed to have a nominal voltage of 273.6 V and a capacity of 6.5 Ah. The system includes 38 battery modules, each formed by six cells in series.

NiCd batteries used to be considered one of the most reliable battery technologies, and have been produced since 1980 (Powers 2000). They have been widely used in the space and aviation industries. For example, they have been used in the main and auxiliary power units in the Boeing 777 airliner. The Boeing 777 has one of the best safety records in aviation history, supporting claims for the reliability performance of NiCd batteries. The battery pack used has a nominal voltage of 24 V and a capacity of 16 Ah. It is formed from 20 NiCd cells and weights 48.5 kg.

The battery shares the same structure as its NiMH counterpart. NiCd batteries use nickel oxide as the cathode, a cadmium compound as the anode and potassium

**Table 9.2** Common nickel-based batteries.

Type	Description
Nickel–metal-hydride (NiMH)	The cell is rated at 1.2 V. The battery is composed of a positive plate containing nickel hydroxide as the positive electrode and a hydrogen-absorbing alloy as the negative electrode.
Nickel–cadmium (NiCd)	The cell voltage is rated at 1.2 V. The battery uses a nickel oxide and cadmium compound.

hydroxide solution as the electrolyte. They also use the ANSI standard AA and AAA sizes, but are no longer as widely available as their NiMH counterparts. They exhibit low voltage drop over the discharge period, but the energy density is no longer competitive with the latest battery technologies. Standard AA cells generally have capacities of 600–800 mAh, which is significantly lower than NiMH cells. Nickel-based batteries show a memory effect that tends to “remember” the previous operation cycle, so a relatively deeper charge/discharge cycle is required than for batteries without a memory effect. The self-discharge rate of nickel-based batteries is significantly higher than the latest lithium-based technologies.

### Lithium-based batteries

Lithium-based technologies have drawn significant attention and grown exponentially due to their significant advantages, such as high energy density per unit volume and per unit weight. The typical cell voltage rating is 3.6 V, which is generally higher than other types. The self-discharge rate is lower than that of NiMH batteries and there is no memory effect. Furthermore, high efficiencies can be demonstrated in fast charge and discharge. In a lithium-ion cell, the positive electrode is usually activated by cobalt acid lithium, while the negative electrode is activated by highly crystallized specialty carbon. The lithium cobalt oxide material is ionized and the ions move to the negative electrode. During discharge, the ions move to the positive electrode and turn into the original compound.

The advantages of lithium-ion batteries mean they are widely used for transportation fleets and portable electronic devices. Table 9.3 outlines two examples of lithium-ion batteries that have attracted much media coverage in recent years. Further information about these technologies and the latest updates can be sourced from the relevant websites at [www.boeing.com](http://www.boeing.com) and [www.chevrolet.com](http://www.chevrolet.com).

The Boeing 787 airliner uses lithium-ion batteries to replace their NiCd counterparts. This gives a significant improvement in terms of power capacity and high power over the Boeing 777. However, in the first year of service, the aircraft suffered a number of fire incidents resulting from the lithium-ion battery packs. As a result of the Boeing 787 incidents, in 2013, Airbus reverted to NiCd batteries for the newly developed A350 XWB.

The Chevrolet Volt is a plug-in hybrid vehicle and is an example of a lithium-ion battery application for ground transportation. The battery pack is rated at 16.5 kWh at a nominal voltage of 355.2 V. The capacity of the battery pack is not as high as other

**Table 9.3** Typical applications of lithium-ion batteries.

Applications	Battery pack specification
Boeing 787	Each battery unit is configured with 8 lithium-ion cells Nominal voltage of 32 V, 28.6 kg weight More powerful but lower weight and smaller size than NiCd counterpart
Chevy Volt	Battery pack weighs 197 kg, formed from 288 lithium-ion cells Nominal voltage 355.2 V and 16.5 kWh capacity Narrow cycle of charge and discharge (60% of total capacity) is used for day-to-day operation

electric vehicles because the vehicle is also equipped with an internal combustion engine which can drive an electric generator and provide charge if required. The system is designed for a light charge and discharge cycle in order to prolong the battery life cycle. It has generally received positive reviews thanks to the selection of an appropriate battery technology and the design of the battery management system.

Lithium-based technologies are the latest battery technology, with more and more applications emerging, including utility-scale storage. Safety precautions should be always taken; the high energy density is advantageous, but is potentially hazardous. Misuse and lack of protective measures may cause battery explosion or ignition.

One special technology is the sodium–sulfur (NaS) battery, which has several important advantages: high energy density, long cycle life, low-cost materials, and high efficiency. The Japanese company, NGK Insulator Inc, is the major manufacturer for this technology (Beaudin et al. 2010). According to the company's website at <https://www.ngk.co.jp>, an NaS battery cell uses sulfur as the positive electrode and sodium as the negative electrode. Beta alumina ceramic is used between the electrodes. During discharge, sodium ions are released from the negative electrode and are transferred through the solid electrolyte into the sulfur at the positive electrode. The battery charging is the reverse of the discharge process, with sodium forming in the negative electrode. High operating temperatures are required for molten sodium, which limits use to stationary applications. The nominal voltage of an NaS cell is 2 V. The technology is considered suitable as an energy buffer for mitigating power intermittency in renewable electricity resources, such as solar and wind. The high operating temperature is also a concern because of the fire hazard involved.

### 9.1.2 Battery Terminology

A battery module is formed from series-connected cells sealed into one unit. Battery modules are mechanically and electrically assembled to form a battery pack. In large-scale systems, battery packs are grouped together to form a battery bank. A battery management system is generally required to regulate the battery system operation and protect it from damage if the capacity becomes significant; multiple cells in complex configurations can exhibit mismatches, which can be unsafe. The important terms relating to battery voltage are described in the following:

- *Nominal voltage*: can refer to the cell, module, or pack levels, and is the voltage reference for system rating and design. When batteries are used in practical systems, the terminal voltage is generally different from the nominal voltage. The terminal voltage depends on the instant load condition, state of charge, and temperature.
- *Cut-off voltage*: the least allowable voltage to discharge the battery. For rechargeable batteries, any discharge operation may result in damage when the terminal voltage is lower than the cut-off limit.
- *Open-circuit voltage*: measured when no charge or discharge is taking place. It is commonly considered as an indicator of battery capacity. Compared to the nominal voltage, a high value indicates high remaining SOC. However, the absolute value also depends on the temperature.
- *Float voltage*: voltage level for the battery charger to maintain a trickle charge when the battery has been fully charged. The voltage level is generally defined to maintain the battery capacity against discharge and avoid overcharging the battery.

The terms for energy and capacity are as follows:

- *Nominal battery capacity* is generally defined as the total amp-hours available. If a battery capacity is 1 Ah, without considering power loss, it indicates that the nominal capacity can be fully discharged in 1 h if the discharge current is 1 A. On the other hand, in theory, the battery can be fully charged from empty when a current of 1 A is applied for 1 h.
- *C-rate* is the rate at which a battery is charged or discharged relative to its rated capacity. If a battery capacity is 1 Ah, a 1C discharge rate means that the discharge current is 1 A. A C/4 charge rate indicates the charge current is 0.25 A. In theory, the time to fully charge from empty is 4 h when C/4 is applied.
- *State of charge (SOC)*: is an expression of the present battery capacity as a percentage of the rated capacity.
- *Depth of discharge (DOD)* refers to the percentage of battery capacity that has been discharged over the rated capacity.
- *Nominal energy* is an important term to define the energy capacity of batteries. It can be derived from the nominal voltage (V) and capacity (Ah). The measurement unit is Wh or kWh. Its value is important to size standalone PV systems with consideration of the load profile.
- *E-rate* is the rate at which a battery is charged or discharged relative to its nominal energy.

Other important terms are:

- *Charge cycle* is defined as the process of charging a rechargeable battery to a high capacity and discharging to a low capacity. In a PV power system, it is usually counted day by day since the charge happens during daytime and discharge is at nighttime.
- *Deep cycle* for a rechargeable battery is when it is charged to more than 80% of the SOC and then discharged to less than 20% of the SOC. Since the cycle life depends on the DOD, frequent deep-cycle operation generally causes fast aging and a short life span.
- *Recommended charge current* is the ideal current at which the battery is initially charged (to roughly 70% of SOC) under a constant charging scheme before transitioning to constant voltage charging. Temperature should be always considered when determining the recommended charge current.
- *Recommended charge voltage* is the voltage at which the battery is allowed to be charged up to the full capacity. The cycle charge includes both the regulation of current and voltage. Temperature is generally required to precisely determine the recommended charge voltage.
- *Cycle life* is the number of discharge-charge cycles the battery can experience before it fails to meet specific performance criteria. The evaluation and estimation of cycle life should be based on specific charge and discharge conditions, such as the charge rate, discharge rate, DOD, temperature, and humidity. It is generally considered that the higher the DOD per cycle, the lower the cycle life.

### 9.1.3 Charging Methods

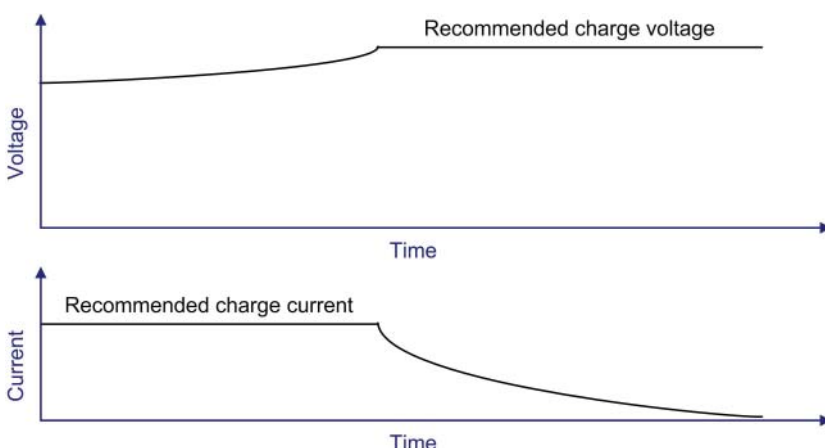
Charging is a process to restore a discharged battery to the required capacity. It is important to use a proper charging method and maintain proper charge cycles for long battery lifetime. Battery charging methods are in three categories:

- cycle charging
- compensating charging
- float charging.

The standard cycle charge usually starts with a constant current, and then a constant voltage. Cycle charging is designed to charge the battery from a low percentage of SOC to a higher level or full charge. It starts with a constant-current charge cycle and allows the voltage to rise, as illustrated in Figure 9.6. It is commonly referred to as the bulk stage, since most capacity is recovered during this cycle. The maximum charging current is usually set to prevent any significant temperature rises, which would result in fast aging and early degradation. The C-rate is commonly used as a measure of the charging current. When the voltage reaches the upper level, the charging cycle becomes a constant-voltage operation. This is also referred to as the “absorption stage”. The battery capacity will be recovered to the full level at this stage when the charge current reaches a significantly low level, as shown in Figure 9.6.

Compensating charging is also called trickle charging, and is applied to maintain the battery capacity against self-discharge. Float charging is used where the battery is in parallel connection with the load. In PV power systems, solar power is used to supply the load during the day, while any surplus power is used to charge the battery. A strict charging cycle for constant current is difficult to maintain in the float charging process due to the variation of load conditions. Both trickle and float charging are considered constant-voltage charging methods since the battery voltage must be maintained at a constant level.

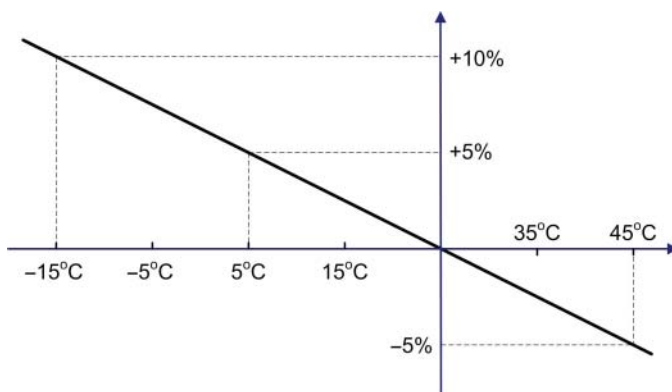
Table 9.4 shows the typical ratings to charge lead-acid batteries. It should be noted that the ratings are for a constant temperature of 25°C and are presented only for reference purposes. Accurate ratings should follow the manufacturer's recommendations, along with consideration of environmental conditions. The setting can be calculated according to the nominal voltage and battery capacity. For a battery module rated as 12 V/100 Ah, to perform cycle charging, the recommended charge current is 40 A and the voltage is 14.4 V.



**Figure 9.6** Cycle charge with constant current and constant voltage: top, charging voltage; bottom, charging current.

**Table 9.4** Typical settings for charging lead-acid batteries.

Charging method	Recommendation
Constant current for cycle charge	Recommended current is 0.4C or lower. The lower the rating, the longer the charging time.
Constant voltage for cycle charge	Recommended voltage is 120% of the nominal voltage.
Trickle charging	Recommended voltage is 115% of the nominal voltage.
Float charging	Recommended voltage is 115% of the nominal voltage.

**Figure 9.7** Charging voltage with temperature compensation.

Ideally, the battery should be stored or operated in a environment in which the ambient temperature is conditioned. High temperatures accelerate aging, while low temperatures constrain capacity. Temperature compensation should be considered for the charging voltage when the battery temperature varies significantly and can be sensed. The objective is to either prevent fast aging if the battery temperature too high or to guarantee sufficient charging when the temperature is lower than required. The general rule is to increase the charging voltage if the temperature is lower than 25°C and decrease it when temperature is higher than 25°C. For lead-acid batteries, it is recommended to have a compensation slope to adjust the charging voltage according to the temperature. Figure 9.7 shows a reference chart for temperature compensation with a slope of  $-0.25\%$  per degree. For example, if the nominal charge voltage is 14.4 V for a 12-V battery module, the charging voltage should be adjusted to 15.8 V if the temperature is 15°C below zero. When the temperature becomes 45°C, the charging voltage is set to 13.7 V according to the compensation curve. It should be noted that different battery manufacturers might recommend different values for temperature compensation.

The settings in Table 9.4 are considered a general reference. Battery temperature is considered as the main factor that affects aging and damage. The charging rating can be more accurately defined and automatically adjusted if the battery temperature can be monitored as it charges. Without temperature sensing, the battery charging cycle is usually defined in a conservative way in order to avoid any unexpected temperature rises that would cause fast aging and damage. Rapid charging can be performed when the

battery temperature is either monitored or regulated. The charging current and voltage can be adaptively adjusted in real time in response to temperature variations.

For example, the charging current for rapid charging can be regulated up to 1C for NiMH batteries when the ambient temperature is higher than 0°C but lower than 40°C, according to the recommendation of Panasonic. The rapid charging should be turned off if one of the following conditions is detected, at which point trickle charging is activated:

- the NiMH cell voltage reaches the extreme level of 1.8 V
- the cell voltage starts to drop by up to 10 mV
- the cell temperature increases too fast; up to 2°C/min
- the cell temperature reaches the upper limit of 40°C
- the rapid charge time is recorded up to 90 min.

Panasonic recommends a two-stage cycle charging for its lithium-ion batteries. It starts with a constant-current charging cycle and the voltage is allowed to rise. When it reaches the upper voltage limit, the charging cycle becomes a constant-voltage operation, which maintains the battery voltage at a constant level. The battery capacity is considered to be fully recovered at this stage. The typical settings for lithium-ion batteries are summarized in Table 9.5. The charge should be stopped if the charge current decreases to 0.1C. It is considered a malfunction if the charging time is longer than 720 min and the current is still higher than 0.1C. Charging should be stopped and an error should be signaled by the charge controller.

If the initial battery voltage is only 80% of the nominal voltage, the battery is usually considered as deep discharged. To avoid any damage caused by rapid charging, a slow charging process should be used, in which the charge current is set to 0.1C or less. It should be noted that the recommended ratings for various charge methods is only a general reference; the manufacturer's recommendation should be always followed because of the variety of different battery technologies.

#### 9.1.4 Battery Mismatches and Balancing Methods

Similar to the construction of PV modules and strings, battery modules and packs are formed from multiple cells in series connection, so as to reach the required voltage level. Ideally, all battery cells in one battery pack are identical and share the same SOC and electrical characteristics. However, mismatches happen along each string since battery cells can be different, for various reasons, such as manufacturing defects, temperature gradients, and uneven aging. Between 1% and 10% of mismatches are due to manufacturing defects (Rehman et al. 2014).

During charging and within one string, a stronger cell gains SOC faster than a weaker one. During discharging, the SOC of the weaker cell decreases faster than the

**Table 9.5** Typical settings for charging lithium-ion batteries.

Charging method	Recommendation
Constant current for cycle charge	Recommended current is up to 0.7C. The lower the rating, the longer the charging time.
Constant voltage for cycle charge	Recommended voltage is 117% of the nominal voltage.
Charge temperature	Between 10°C and 45°C.

### 9.1.6 Battery Selection

It should be noted that NiCd batteries can only be used where there is a simple requirement for steady runtime voltage and reliability. NiCd cells are not as low-cost as their lead-acid counterparts, but the low capacity density prevents their use in the majority of applications. In PV systems, the battery implementation can be either for stationary energy storage or in mobile applications. Lead-acid, NiMH, lithium-ion, and NaS batteries are all widely available for such uses. The following tips can be considered for selecting among them.

- *Lithium-ion technology* is suitable for different scales and applications, has high performance in terms of capacity density, and is becoming cheaper due to recent mass production. Detailed sensing and protection should always be used to guarantee safe operation, especially for systems with significant storage capacity.
- *Lead-acid batteries* can be selected for either vehicular or stationary implementations. Their advantages lie in the maturity of the technology and their low cost. The drawbacks are the low capacity density per unit weight and volume.
- *NaS technology* has potential for large-scale stationary energy storage due to its high operating temperature. However, the supply is limited to a single source, which is different from the other technologies.
- *NiMH batteries* can be used for small-scale PV systems for either vehicular or stationary implementations when the power density is not critical. The technology is generally low cost, but has shorter life cycles, higher self-discharge rates, a memory effect, and is inefficient in comparison with lithium-ion batteries.

## 9.2 Integrating Battery-charge Control with MPPT

Charging is the process of storing solar power in discharged batteries. A suitable charging method should be used to charge them efficiently and prevent any damage. To stop the PV generation from overloading the charging capacity, the charging cycle should be maintained with an MPPT function.

When the voltage and current of the battery reach their charging-cycle limits, MPPT should be stopped in order to reduce PV power generation. Instead, the control action should shift the operating point of the PV generator in the open-circuit voltage direction or into the voltage-source zone. It has been reported that the system dynamics of the voltage-source zone gives better damping performance than the current-source zone (Xiao et al. 2007). The PV I–V curve has been divided into three operating zones: current-source zone, power-source zone, and voltage-source zone, as shown in Figure 6.2. It is recommended to operate the PV output in the power-source and voltage-source zones and to avoid the current-source zone.

Figure 9.28 illustrates the integration of MPPT and cycle-charge control, in terms of constant voltage and constant current regulation. For battery-charging applications, the battery voltage and current are sensed to determine the operation status. If both are under their defined limits, MPPT is used to deliver the highest charging power. If either limit is reached, the control variable moves the operating point away from the MPP, in the direction of the open-circuit voltage. For the case study,  $\pm 1\%$  hysteresis is applied to the regulation for both battery voltage and battery current. The hysteresis error can

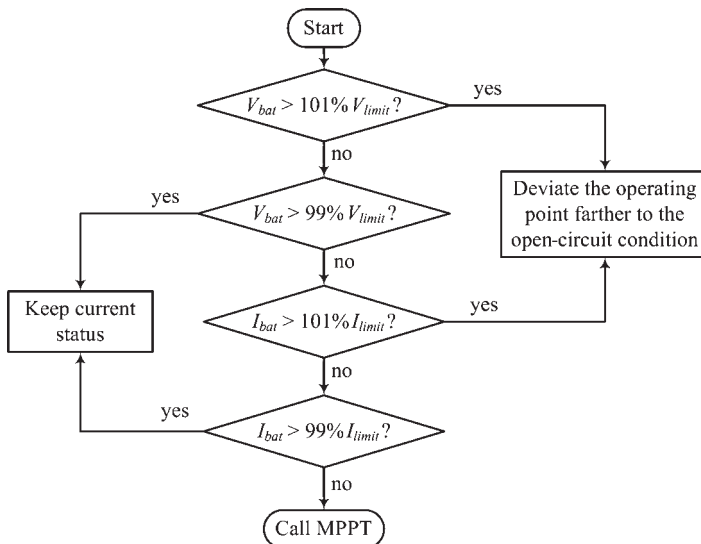


**Figure 9.28** Integration of maximum power point tracking for battery charge control.

be other values depending on the practical requirements. When the sensed voltage and current are within their predefined tolerances, the controller maintains the steady-state condition.

## 9.3 Design of Standalone PV Systems

This section introduces the design, integration, and simulation of standalone PV power systems. The systems may or may not include significant energy storage. “Significant” energy storage means that the storage capacity is sufficient to mitigate the intermittency of PV generation. Switching-mode power supplies contain energy storage units, such as inductors and capacitors, to constrain switching noise, which is considered insignificant in comparison with batteries.

### 9.3.1 Systems without Significant Energy Storage

Most DC loads can be supplied with a certain range of DC voltage. A direct-coupled system is the simplest solution and can be designed to match the PV module with the load demand. An example is used to demonstrate the design procedure. A solar-powered ventilation system is required to provide airflow up to 700 CFM (cubic feet per minute). A cooling fan is selected to meet the airflow requirement, the specifications for which are shown in Table 9.9. A PV module should be selected to match the supply voltage range and the power requirement.

To match the voltage range from 18 to 30 V, as shown in Table 9.9, a PV module is constructed from 48 crystalline solar cells. The size of the solar cells is 6 inches, with a current rating of 7.20 A. A suitable PV module is selected, and the specification is shown in Table 9.10. The rated MPP of the PV module is close to the rated voltage and current required by the cooling fan. The peak power at STC is 170 W, which is slightly lower than

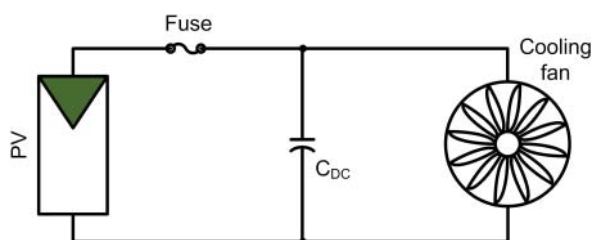
**Table 9.9** Specification of Orion 12HBXC01A cooling fan.

Term	Rating
Model number	NMB F225A4-092-D0530
Nominal voltage	24 V
Nominal current	7.20 A
Voltage range	18–30 V
Rated power	172.8 W
Rated air flow	763 CFM

**Table 9.10** Specification of Invensun i170-48P PV module.

Basic information					
Manufacturer	Model	Cell material	Dimension		
Invensun	i170-48P	Poly-crystalline	1316 mm × 995 mm × 40 mm		
Electrical performance at STC					
Cells	$P_{MPP}$	$I_{MS}$	$V_{MS}$	$I_{SCS}$	$V_{OCS}$
48	170 W	7.14 A	23.81 V	7.72 A	28.8 V
Temperature coefficients					
$\alpha_T$		$\beta_T$		$\gamma_T$	
0.06%/°C		-0.35%/°C		-0.45%/°C	

$\alpha_T$ ,  $\beta_T$ , and  $\gamma_T$  are temperature coefficients for correcting the PV module output current, voltage, and power, respectively.

**Figure 9.29** System diagram of direct coupled PV system for ventilation.

the rated power of the load, 172.8 W. The system can safely operate at 170 W, without being overloaded.

The system is shown in Figure 9.29. A DC-link capacitor gives a start-up current and maintains a steady voltage at the DC link. The fuse is rated as 15 A, in line with the recommendation in the PV module datasheet.

Although direct coupling is the simplest solution, it is very difficult to achieve an exact match between the off-the-shelf load and the PV generator when variation of environmental conditions is a factor. In many cases, the system design is customized for either the load or the PV unit. Simulation for case studies can be conducted only if the I–V

characteristics of the PV module and the load are available. However, the manufacturer of the cooling fan does not provide such information. Experimental testing therefore becomes important.

It should be noted that many cooling fans monitor the input voltage and apply autostart and stop based on the voltage level. If such a function is not supported or does not fit the PV output curve, an additional control circuit should be included to support the start and stop function with a hysteresis loop. In this case, the voltage window of the load is 18–30 V. The voltage threshold for start can be set to 24 V or higher to ensure that the PV module can support enough power at the start point. Without the hysteresis setting, the system can start and stop frequently in the early morning since the irradiance level is not sufficient to support the nominal operating power even though the open-circuit voltage is high enough.

Without power-conditioning circuits, the MPPT function cannot be implemented. This hints that the PV module mostly operates away from the peak power point due to the variation of environmental conditions. Therefore, more and more recent PV systems are including power-conditioning units, to allow use of MPPT and flexibility in design and operation. A direct-coupled system can be redesigned to integrate a dedicated power conditioner.

One important application is proposed by Mascara NT, a French company, which supplies highly efficient off-grid systems for seawater desalination. The concept is simple, since fresh water is only produced when solar power is available. The system stops at night or when the weather is bad. The “storage” is fresh water instead of any electrical format. Even though no significant battery storage is required, power conditioning is included in the conversion stage between the PV section and the load. Reverse osmosis is used for high-efficiency desalination. Solar power drives the pump motor and supplies ancillary devices. A DC bus is formed from multiple PV strings in order to directly supply the desalination unit.

### 9.3.2 Systems with Significant Energy Storage

When energy storage is required, system design generally follows six steps, as shown in Figure 9.30 and described in the following steps:

- 1) The load profile should be clearly specified, including the daily energy consumption and the rated voltage. The energy consumption is measured in Wh or kWh for a 24-h period. The nominal load voltage is the reference for rating the battery pack and solar generation unit voltages.

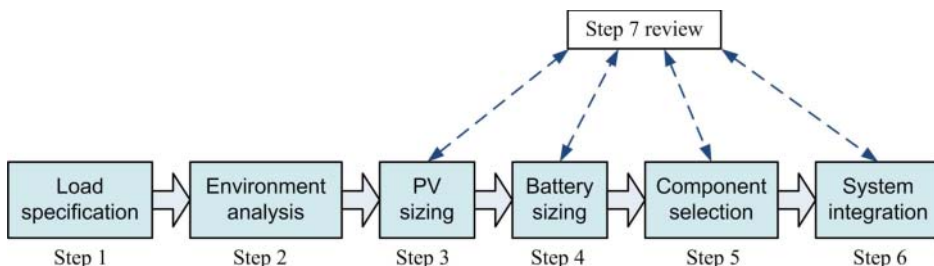


**Figure 9.30** A design procedure for PV-battery systems.

- 2) The location should be thoroughly examined to derive information about the level of solar irradiance and ambient temperatures. It is known that solar irradiance is directly correlated with PV power generation. High temperatures can degrade power generation. It should be noted that the analysis is based on rough estimates since the exact weather cannot be accurately predicted.
- 3) The rule for sizing the PV generation unit is based on the daily load consumption and the lowest solar generation period. PV generation should be more than the load consumption over a 24-h period. The PV generation unit can be slightly oversized to deal with uncertainty.
- 4) The voltage of the battery pack should be specified to match the load voltage rating in order to avoid a high ratio of voltage conversion. The battery capacity should be sufficient to mitigate the power variation between daytime generation and nighttime load consumption. The possibility of a deep charge/discharge cycle – more than 60% – should be minimized since it accelerates battery aging. The capacity of the battery pack should generally be oversized by 20–30% to cope with charge and discharge losses.
- 5) The system should be designed according to the specifications of the load, PV generation unit, and battery pack. DC/DC and/or DC/AC converters might be used according to the load requirement. Protection and disconnect functions should be included. A complete schematic should be presented for review.
- 6) The design document should include a single line diagram of the system structure, showing all component ratings and details.
- 7) The final step is to review the whole system specification and design. The design can be revised if any outstanding issues are raised.

The design process can be demonstrated by an example. The load specification is shown in Table 9.11. The 24-h energy consumption,  $E_{load}$ , is calculated to be 3200 Wh using (9.6). According to the voltage rating, a battery pack rated at 48 V should be used to meet the acceptable voltage-variation range.

$$E_{load} = 140 \times 8 + 130 \times 16 \quad (9.6)$$

Step 2 is to evaluate the environmental conditions at the installation location. The information collected is shown in Table 9.12. It should be noted that it is impossible to predict any weather condition accurately. Extreme weather is not included in this design process due to its unpredictability. Since the highest temperature is not significantly higher than STC, the power degradation caused by high temperatures can be neglected in this example.

**Table 9.11** Specification of DC load.

Term	Rating
Nominal voltage rating	48 V DC
Acceptable voltage range	42–56 V
Averaged power consumption from 9am to 5pm	140 W
Averaged power consumption at other hours	130 W

**Table 9.12** Weather information for PV power generation.

Term	Rating
Average irradiance in 8 h period year round	600 W/m <sup>2</sup>
Low irradiance in 8 h period on rainy days	200 W/m <sup>2</sup>
Average high temperature over year	25.9°C
Average low temperature over year	8.1°C

Step 3 is to size the PV power generator unit. The solar power generation is expected to be sufficient even though the average irradiance is only 200 W/m<sup>2</sup> on rainy or cloudy days. The daily energy generation should be more than 3200 Wh, which is the daily load requirement. The rated power of the PV unit should be calculated from the 8-h generation limit in a 24-h base period, corrected for any estimated losses. The minimum PV power capacity is calculated to be 2500 W, with a 20% loss expected in the power conversion:

$$P_{STC} = \underbrace{\frac{1000}{200}}_{\text{irradiance}} \times \underbrace{3200}_{\text{load}} \times \underbrace{\frac{1}{1 - 20\%}}_{\text{loss}} \times \underbrace{\frac{1}{8}}_{\text{8-hour}} \quad (9.7)$$

Step 4 is to size the battery pack to store excess energy produced by the PV unit and supply the load at night. It is estimated that there will be 16 h without any solar energy input in a 24-h period. According to the load profile, the minimum energy capacity of the battery is 480 Wh, with a cycle between 0% and 100%. It is commonly recommended to operate the battery in a light cycle, from 40 to 90%, for long operational life. Therefore, the nominal energy capacity of the battery pack is rated as 4160 Wh:

$$E_{bat} = \underbrace{\frac{1}{90\% - 40\%}}_{\text{battery cycle}} \times 16 \times 130 \quad (9.8)$$

Based on the requirements for its capacity, the battery capacity in C rate terms can be rated as 87 Ah from

$$C_{bat} = E_{bat} / V_{b-nom} \quad (9.9)$$

where  $V_{b-nom}$  refers to the nominal voltage of 48 V in this case. The battery pack can be formed from four 12-V battery modules in series connection. The BK-10V10T battery modules are used to form the battery pack, since each is rated at 12 V and 90 Ah.

A solar charge controller is used to maintain the battery charging cycle and maximize PV generator output. The FLEXmax 60 used is manufactured by Outback Power Inc. The key specifications are shown in Table 9.13. Further information can be found on the product website at [www.outbackpower.com](http://www.outbackpower.com).

The voltage rating of the PV string should match the input voltage window of the charge controller, which should not be higher than 150 V in cold conditions. The voltage at MPP should be higher than the open-circuit voltage of the battery pack at 100% SOC. In this case, the voltage window is from 56 to 150 V in order to construct the PV string.

**Table 9.13** Key specification of the charge controller–FLEXmax 60.

Term	Rating
Nominal battery voltage	Programmable for 12, 24, 36, 48, or 60 V
Maximum output current	60 A
Maximum input voltage	150 V
Voltage conversion	Step down

**Table 9.14** Specification of PV module Q.PLUS BFR-G4.1.

Basic information					
Manufacturer	Model	Cell material	Dimensions		
Q Cells	Q.Plus BFR-G4.1	Multi-crystalline	1000 mm × 1670 mm × 32 mm		
Electrical performance at STC					
Cells	$P_{MPP}$	$I_{MS}$	$V_{MS}$	$I_{SCS}$	$V_{OCS}$
60	280 W	8.84 A	31.67 V	9.41 A	38.97 V
Temperature coefficients					
$\alpha_T$		$\beta_T$		$\gamma_T$	
0.04%/°C		-0.29%/°C		-0.40%/°C	

$\alpha_T$ ,  $\beta_T$ , and  $\gamma_T$  are the temperature coefficients for correcting the PV module output current, voltage, and power, respectively.

The Q.Plus BFR-G4.1 solar module is selected for this application. It is produced by Hanwha Q Cells GmbH. The key specifications at STC are shown in Table 9.14. Detailed and updated information is found at the product website at [www.q-cells.com](http://www.q-cells.com).

Nine PV modules are required for this application, since each is rated at 280 W. The total power capacity is 2520 W, which is higher than the fundamental requirement of 2500 W at STC. The modules can be configured into three strings, each with a number of PV modules in series ( $N_{series}$ ) of 3. The maximum DC voltage is calculated as the sum of the rated open-circuit voltage of each string, with correction for the lowest expected temperature:

$$V_{pvdc}(\text{max}) = K_T \times 3 \times 38.97 = 116.91 K_T \quad (9.10)$$

where  $K_T$  is the correction factor. The installation location is expected to become as cold as 8.1°C, and  $K_T$  can be as determined from the temperature coefficients listed in Table 9.14. Using (9.11) it can be calculated as 1.17. Therefore, the maximum DC voltage is rated as 137 V, lower than the 150 V required by the charge controller. At the STC, the string voltage at MPP is 95 V. Even though the MPP voltage is lower when the temperature is higher than 25°C, the voltage rating at MPP should be always higher than the minimum requirement of 56 V in order for the step-down voltage conversion that is required by the battery-charge controller.

$$K_T = 1 + \beta_T(8.1 - 25) \quad (9.11)$$

Figure 9.31 is the single line diagram for the standalone system configuration. The specifications of the charge controller and PV module are shown in Tables 9.13 and 9.14. The information about other key components, the battery pack, PV source circuit, DC combiner, DC disconnect, and DC circuit breakers, are summarized in Tables 9.15–9.19 and 9.20, respectively. Together with the climate information for the installation site, the diagram and tables should be included in the final design document. It should be noted that the 48-V battery system requires a higher voltage rating for the circuit components interconnected with the battery voltage bus because of the expected battery voltage variation.

Even though AC loads are common in many standalone systems, these can be equivalent to DC loads since a DC/AC power interface is required to draw DC power from the system. DC/AC conversion systems have been discussed in various books on the subject of power electronics. Therefore the subject is not covered in this book. For a

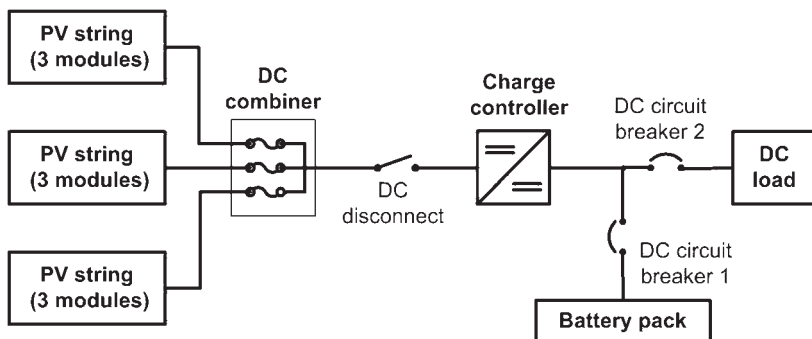


**Figure 9.31** Single line diagram of standalone PV system with battery storage.

**Table 9.15** Battery pack configuration and specification.

Term	Rating or description
Configuration	4 battery modules in series connection
Battery pack voltage rating	48 V
Battery pack nominal capacity	90 Ah
Battery module model	Panasonic BK-10V10T
Battery type	Nickel metal hydride (NiMH)

**Table 9.16** Configuration and specification of PV source circuit.

Term	Rating or description
PV array configuration	3 PV strings in parallel connection
PV string configuration	3 PV modules in series connection
Maximum array voltage rating	137 V
Maximum array current rating	35.3 A

**Table 9.17** Configuration and specification of DC combiner.

Term	Rating or description
Configuration	No less than three inputs
Rating of string protection fuse	15 A
Voltage rating	Not less than 137 V

**Table 9.18** Specification of DC disconnect.

Term	Rating or description
DC disconnect current rating	Not less than 44 A
DC disconnect voltage rating	Not less than 137 V

**Table 9.19** Specification of DC circuit breaker 1.

Term	Rating or description
Amperage rating	90 A
Voltage rating	Not less than 56 V
Configuration	With integrated DC disconnect

PV–battery system, it is always good practice to minimize the use of AC loads due to the loss and complications of DC/AC conversion. More and more modern equipment and appliances are using DC supply.

## 9.4 Equivalent Circuit for Simulation and Case Study

The equivalent circuit for simulation can be derived from the system design in Figure 9.31. Figure 9.32 illustrates the equivalent circuit for analysis and simulation. The simplified Thévenin model is used, and includes the battery pack voltage  $V_{OC}$  and the equivalent series resistance  $R_{bat}$ . The dynamics of the battery link shows interaction with the capacitor,  $C_{BAT}$ , which is the equivalent capacitance across the battery pack. All DC loads are simplified to draw current from the battery link, which is denoted as  $i_{load}$ . A buck converter is the charge controller that transfers the PV power to the battery and supplies the load. The inductor current of the buck converter is denoted  $i_L$ . The circuit dynamics are

$$i_L + i_{bat} = C_{BAT} \frac{dv_{bat}}{dt} + i_{load} \quad (9.12)$$

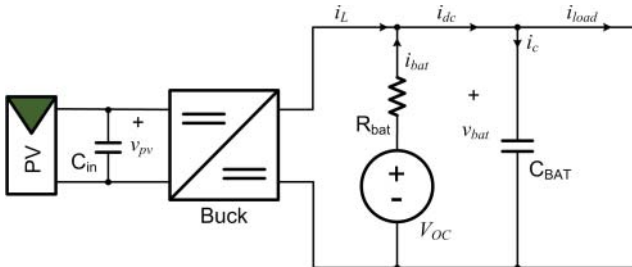
and

$$R_{bat} C_{BAT} \frac{di_{bat}}{dt} + i_{bat} = i_{load} - i_L \quad (9.13)$$

with the assumption of a constant voltage,  $V_{OC}$ , in the short-term steady state.

**Table 9.20** Specification of DC circuit breaker 2.

Term	Rating or description
Amperage rating	5 A
Voltage rating	Not less than 56 V
Configuration	With integrated DC disconnect

**Figure 9.32** Equivalent circuit of standalone PV system with battery storage.

The battery-link dynamics can also be represented by the transfer function:

$$i_{bat}(s) = \frac{i_{load} - i_L}{R_{bat}C_{BATS} + 1} \quad (9.14)$$

In the steady state, the battery current,  $i_{bat}$ , is the error between the load current  $i_{load}$  and the inductor current of the buck converter  $i_L$ . The aggregated capacitance across the battery terminals causes the dynamics at the battery link.

## 9.5 Simulation Model to Integrate Battery-charging with MPPT

MPPT using the HC algorithm was introduced in Section 8.2 and formulated for simulation, as illustrated in Figure 8.6. With the integration of battery-charging cycles, a control flowchart for the PV-powered battery charger can be developed, as shown in Figure 9.28. The Simulink model should integrate the MPPT and the regulation of the battery voltage and current.

Figure 9.33 illustrates the simulation block in Simulink. The bottom section shows the HC operation for tracking the MPP. The MPPT operation can update the control variable only if both the battery voltage and current are within their limits, which are indicated by 0.99Vlimit and 0.99Ilimit. The system is operated in MPPT mode.

If either the battery voltage or current reaches its predefined limit, the system enters the charging-cycle mode. Either the battery voltage or current is regulated to avoid battery overcharging. When the value of either the battery voltage or current is within a 2% tolerance range, the model output Xnew is maintained constant by setting the variation step to zero. However, if either the battery voltage or current reaches their upper limits, denoted 1.01Vlimit and 1.01Ilimit, respectively, the control action will move the

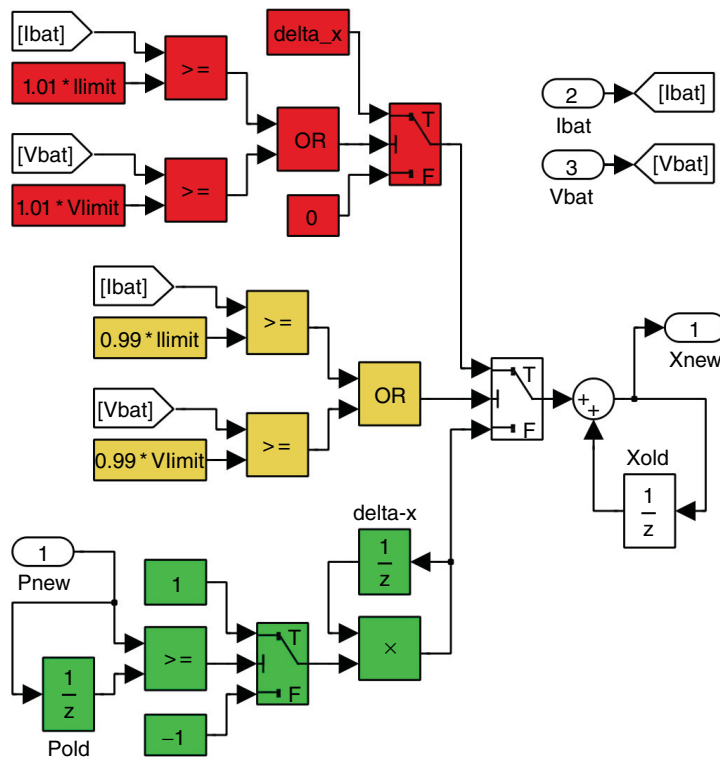


Figure 9.33 Simulink model for integrating MPPT and battery-charging cycles.

operating point in the direction of the open-circuit voltage by updating the value of  $X_{new}$ . In this case,  $X_{new}$  is the PV output voltage. Therefore, increasing its value brings it closer to the open-circuit condition. It should be noted that the 2% tolerance, from 99% to 101%, is just as an example for this case study. Other values can be assigned to maintain the battery voltage and current within a limited range.

## 9.6 Simulation Study of Standalone Systems

A simulation model for the designed system is needed to assess its response to changes of environmental conditions and load variations. The simulation system is based on the case study and design in Section 9.3.2.

### 9.6.1 Simulation of PV Array

The PV cell parameters can be estimated using the specification of the PV module shown in Table 9.14. The PV cell voltage is derived from the module output voltage and the number of cells in series connection. Based on the ideal single-diode model (ISDM), the ideality factor of the PV cell is determined as 1.6882.

The PV array that was developed in Section 9.3.2 has a  $3 \times 3$  configuration of nine PV modules. Therefore, the PV array output characteristics at STC are represented by the

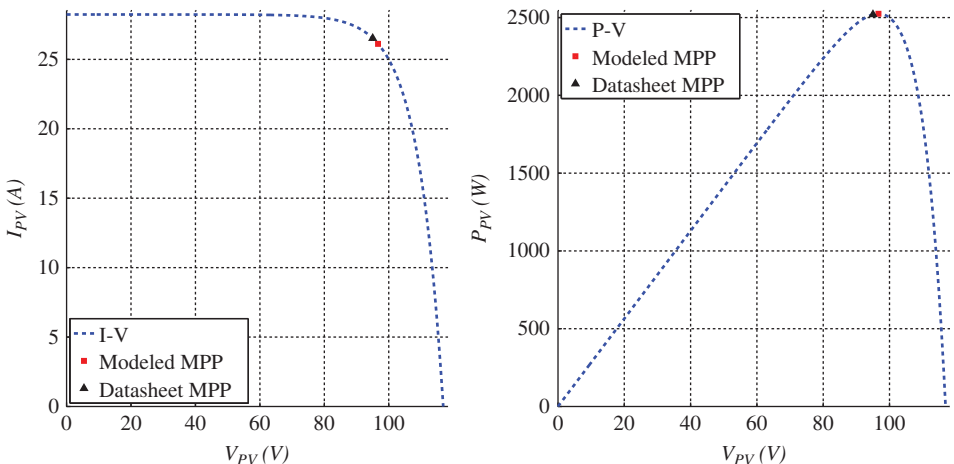


**Figure 9.34** Output characteristics of the  $3 \times 3$  PV array.

I–V and P–V curves shown in Figure 9.34. With balanced operation of nine PV modules, the MPP of the array is indicated as 2525 W and is at (96.66 V, 26.12 A).

### 9.6.2 Short-term Simulation

Figure 9.35 shows the overall model for simulating the standalone system including the PV array, DC/DC buck converter, battery link, and battery pack. The blocks for the solar irradiance, cell temperature, and the load current represent subsystems to be programmed to vary as predefined conditions. It should be noted that the sign of the battery current is defined as positive when it is extracted from the battery pack. Modeling of the buck converter used as the PV-side converter was introduced and developed in Section 5.1.2. The model is capable of capturing the dynamics during each switching cycle. For the case study, the specification of the buck converter is as shown in Table 9.21. The same parameters are used for the medium-term and long-term simulations described in later subsections.

The system control is represented by the blocks for the MPPT charger, PID controller, and PWM generator. The PID controller and PWM generator are those developed in Section 7.8.3. Based on the nominal operating condition and circuit parameters, as shown in Table 9.21, a small-signal model can be derived using the modeling process in Section 6.3.2. The model has a damping factor of 0.26 and an undamped natural frequency of  $1.08 \times 10^3$  rad/s. Affine parameterization is used to design the feedback controller to regulate the PV-side voltage in order to follow the MPP. As a result, the PID controller for the voltage regulation of the PV link is synthesized and expressed as

$$C(s) = -0.0017 - \frac{8.4736}{s} - \frac{6.8485 \times 10^{-6}}{2.8745 \times 10^{-4}s + 1} \quad (9.15)$$

The MPPT charging block is implemented as shown in Figure 9.33. The MPPT parameters are summarized in Table 9.22. The tracking frequency should always be determined by the dynamic analysis of the PV-link voltage-regulation loop. Without the start-stop mechanism, as introduced in Section 8.6, a 1-V ripple is expected to

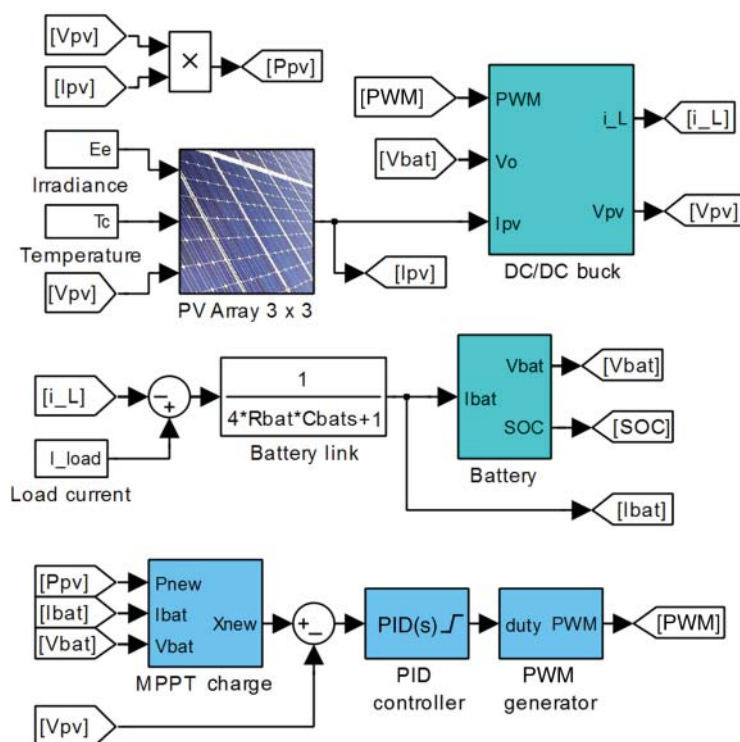


Figure 9.35 Configuration of the standalone PV system with battery storage for short-term simulation.

Table 9.21 Specification of buck converter circuit.

Term	Rating or description
Switching frequency	50 kHz
Inductance	$L = 470 \mu H$
Input capacitor	$C_{in} = 470 \mu F$
Nominal input voltage	95 V
Nominal output voltage	48 V

Table 9.22 Specification of the MPPT algorithm.

Term	Rating or description
MPPT algorithm	Hill-climbing method
MPPT tracking frequency	200 Hz
Perturbation step size	$\Delta V = 1 V$

appear in the PV-link voltage due to the active perturbation of the HC algorithm. The equivalent capacitance across the battery link is set to  $C_{bat} = 33 \mu F$  for the case study.

To avoid battery overcharging, the upper limit of the battery voltage is set to 55 V, which represents the series connection of 40 NiMH cells in the case study. Since a 2% ( $\pm 1\%$ ) tolerance is applied, the band for the voltage limit is between 54.45 and 55.55 V. When the battery voltage is higher than 54.45 V, active tracking of the MPP is stopped and charge control is taken to maintain the battery voltage within the upper limit of the tolerated range.

The simulation model of the buck converter, as shown in Figure 5.6, is computationally intensive due to the fast switching frequency of 50 kHz. The sampling time for simulation should be at a level of nanoseconds to capture the switching dynamics and reveal the detailed transient responses up to the switching frequency. The model is suitable for the total simulation times in seconds in order to prove the design concept of the converter circuit and monitor switching ripples, since the battery voltage is relatively steady over short time periods. The detailed simulation model is inefficient for either medium- or long-term simulations for demonstration of the variation of battery SOC and voltage during charging and discharging. Therefore, the simulation results are neglected for this case study since they have been covered in Section 5.1.2.

### 9.6.3 Medium-term Simulation

The averaged model was introduced in Section 6.3.2. It is based on the assumption that the buck converter is in continuous conduction mode. The expression in (6.17) can be further derived as

$$i_L = \frac{1}{L} \int (dv_{pv} - v_{bat}) dt \quad (9.16a)$$

$$v_{pv} = \frac{1}{C_{in}} \int (i_{pv} - di_L) dt \quad (9.16b)$$

where  $d$  is the switching duty cycle and the control variable. Other variables and parameters refer to the definitions in Figure 9.32.

Figure 9.36 illustrates the simulation blocks for the averaged model of the DC/DC buck converter. The inputs include the duty cycle, the output voltage, and the PV injection current, which are labeled duty,  $V_o$ , and  $I_{pv}$ , respectively. The output variables are the inductor current and the PV terminal voltage. The control variable for the averaged converter model is the value of the duty cycle instead of the PWM pulsed signals.

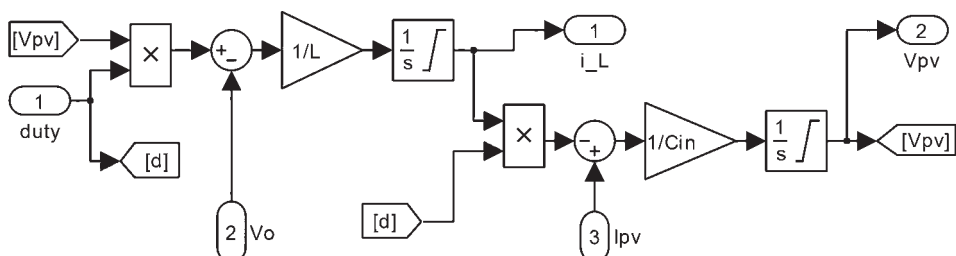


**Figure 9.36** Simulink model of the averaged synthesis of the buck converter.

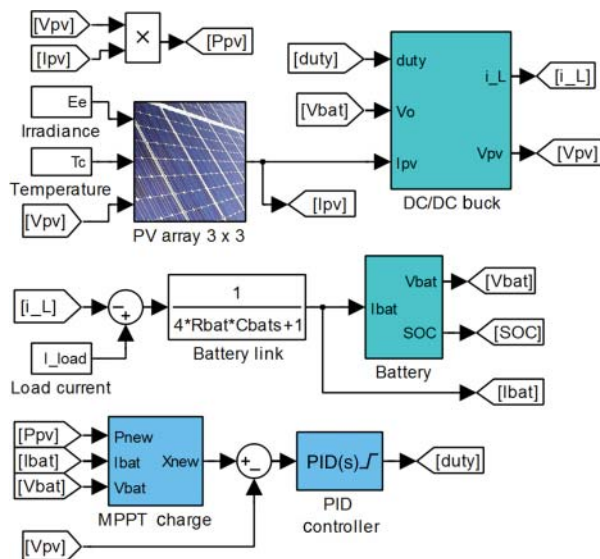


**Figure 9.37** Configuration of standalone PV system with battery storage for medium-term simulations.

The switching ripples will not be expected in the simulated waveform of the PV-link voltage and the inductor current.

Figure 9.37 illustrates the block diagram when the averaged model is used to represent the DC/DC buck converter. The key difference from the switching model in Figure 9.35 is that the input of the DC/DC buck converter model is the value of the duty cycle. The high-frequency PWM signal and switching operation are neglected in the averaged model to improve simulation speeds. The control parameters are kept the same as shown in Tables 9.22 and (9.15). The battery link is represented by the transfer function (9.14). The battery model was as developed in Section 9.1.5 and shown in Figure 9.18.

The simulation result of the case study is illustrated in Figure 9.38. The initial SOC of the battery pack was set to be 50%. A load current of 2.8 A was constantly extracted from the battery link. Before 0.2 s, the irradiance was  $400 \text{ W/m}^2$  and the cell temperature was  $25^\circ\text{C}$ . Since the battery voltage is lower than the limit of 54.45 V, the MPP is tracked at 0.09 s during the start-up period and maintained by the steady-state tracking operation. The voltage ripple caused by the active perturbation of the HC algorithm is noticeable. The SOC gradually increases in response to the charging current. At 0.2 s, the solar irradiance steps up from 400 to  $800 \text{ W/m}^2$ . The PV output power significantly increases, causing an increase of the charging current. The increase of the SOC becomes faster than before. Since the SOC is still relatively low, the battery voltage is still below the upper limit. The MPPT operates continuously so as to inject the highest power into the battery link.

Figure 9.39 illustrates the simulated waveform for another case study. The initial SOC of the battery pack is set to be 80%. Again, a constant load current of 2.8 A is extracted from the battery link. Before 0.2 s, the irradiance is  $400 \text{ W/m}^2$  and the cell temperature is  $25^\circ\text{C}$ . Since the battery voltage is lower than the limit of 54.45 V, the MPP is tracked at 0.09 s and is maintained by the steady-state tracking operation for the highest solar

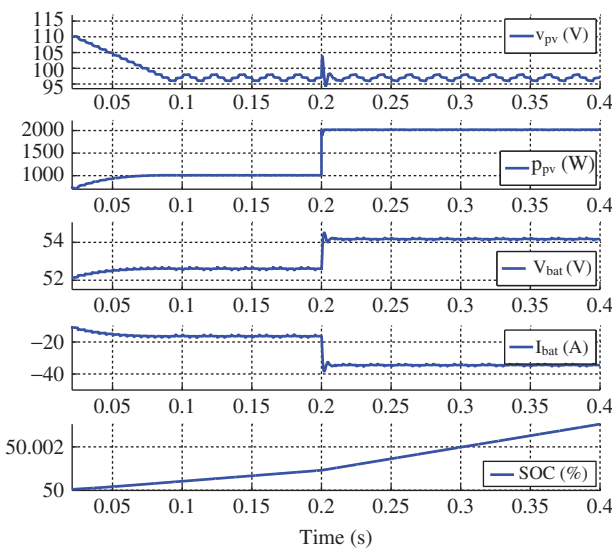


**Figure 9.38** Simulated waveforms showing maximum power point tracking for battery charging.

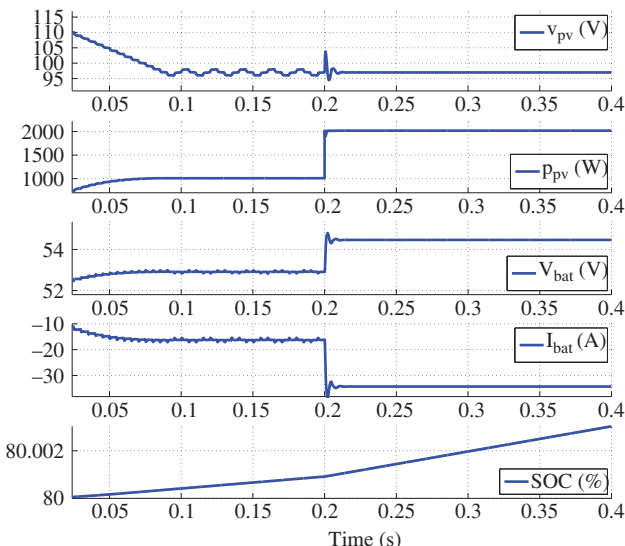


**Figure 9.39** Simulated waveforms showing the transition from maximum power point tracking to battery voltage regulation.

energy harvest. The SOC gradually increases in response to the charging current. At 0.2 s, the solar irradiance steps up from 400 to 800 W/m<sup>2</sup>. The PV output power is significantly increased, causing the increase of the charging current, which is represented as negative in value. Since the SOC is at a relatively high level, the battery voltage reaches the predefined limit due to the equivalent resistance of the battery pack. The active tracking for MPP is stopped, as can be seen from the disappearance of the tracking ripple.

The charging control maintains the battery voltage within the upper limit range. The charging continues, and the SOC increases within the simulation time period of 0.4 s.

Figure 9.40 shows the simulated waveform for the third case study. The initial SOC is 80%, and the load current is a constant 2.8 A. Before 0.2 s, the irradiance is  $800 \text{ W/m}^2$  and the cell temperature is  $25^\circ\text{C}$ . Since the battery voltage reaches the limit of 54.45 V, the system uses battery voltage regulation to maintain the charging cycle. The PV output voltage is maintained at a level higher than the voltage of the MPP in order to maintain low output power. At 0.2 s, the solar irradiance steps down from  $800 \text{ W/m}^2$  to  $400 \text{ W/m}^2$ . The PV output power significantly decreases, causing a decrease of the charging current. Since the battery voltage becomes lower than the limit of 54.45 V, active MPPT is started. It is noticeable that the MPPT operation lowers the PV output voltage to a lower level for the highest power output under an irradiance level of  $400 \text{ W/m}^2$ . The ripple appears again on the waveform of the PV-link voltage. This is caused by the perturbation operation of the HC-based MPPT.

A sudden load change can cause a disturbance to the battery current. It might trigger a transition between MPPT and battery voltage regulation. The variation can also represent a change of the PV output power. Therefore, a case study for load variation is not presented in this section.

The voltage-regulation loop of the buck converter exhibits the highest frequency at the kilohertz level. This requires the simulation sampling time to be at the microsecond level in order to capture the fastest dynamics. For this reason, the averaged model is not efficient for simulation of long-term operations, where there are significant changes of battery SOC and voltage in response to changes in environmental conditions and load. Simulations might result in significant demands for memory and computing speed, which is impractical on standard personal computers.

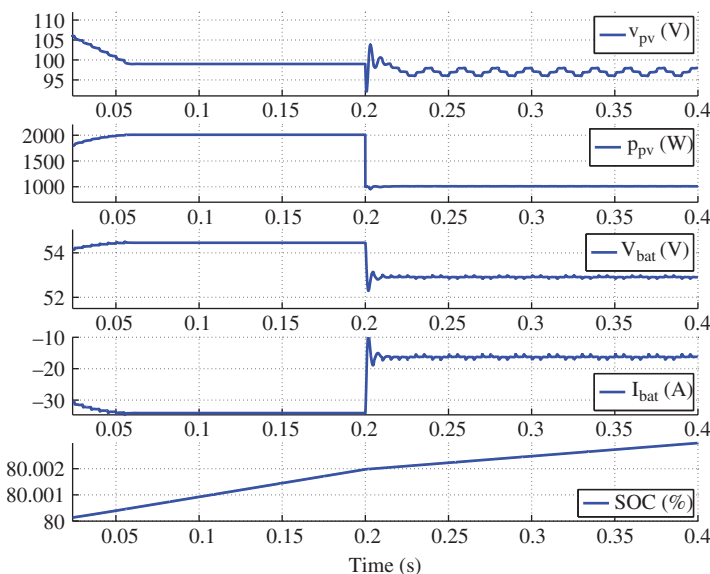


**Figure 9.40** Simulated waveforms showing the transition from the battery voltage regulation to maximum power point tracking.

### 9.6.4 Long-term Simulations

The computer configuration for the simulation cases in this book is shown in Table 9.23. This is considered as a suitable platform to test the simulation efficiency.

It commonly takes hours to charge a battery from low capacity to full. For a long-term simulation, the fast dynamics of the buck converter and the battery link can be neglected. The equilibrium of the buck converter from input to output in continuous conduction mode without the consideration of losses can be expressed as

$$i_L = \frac{i_{pv}}{d} \quad (9.17a)$$

$$d = \frac{V_{bat}}{v_{pv}} \quad (9.17b)$$

where  $d$  is the switching duty cycle and the control variable. Other variables and parameters refer to the definitions in Figure 9.32. The dynamics caused by the capacitor, inductor, and switching operation are ignored.

The model of the standalone PV system with battery storage for long-term simulation can be constructed as shown in Figure 9.41. The model simply shows an energy correlation between the PV array and the battery pack. The buck converter is represented by (9.17). The voltage of the PV link is the direct output of the MPPT charge controller with the assumption that the PV array voltage follows the command much faster than the MPPT dynamics. The control functions for MPPT and the regulation of the battery voltage and current are the same as for the short- and medium-term simulations. The highest frequency in the simulation model becomes the MPPT frequency, which is 200 Hz. Therefore, the sampling frequency for simulation can be set to 2 kHz in order to simulate the system efficiently.

Figure 9.42 shows the simulated waveform for a two-hour system operation. The initial SOC of the battery pack is set to be 50%. Again, the load current is 2.8 A, constantly extracted from the battery link. For 40 min, the irradiance is 400 W/m<sup>2</sup> and the cell temperature is 25°C. Since the battery voltage is lower than the limit of 54.45 V, the MPP is tracked and maintained for the highest solar energy harvest. A voltage ripple appears in the waveform of the PV-link voltage,  $v_{pv}$  due to the perturbation of the HC algorithm. The SOC gradually increases in response to the charging current.

After 40 min, the solar irradiance changes from 400 to 800 W/m<sup>2</sup>. The PV output power significantly increases, causing an increase of the charging current. Since the SOC is at a medium level, the battery voltage is still below the voltage limit. Therefore, MPPT operates for 38 min and gives a fast increase of the SOC. After 68 min, active MPPT is stopped because the battery voltage rises to a level of 54.45 V. The system

**Table 9.23** Specification of the simulation computer.

Term	Specifications
Computer model	Dell Precision T1650
Operating system	Windows 10 Pro, 64-bit
Processor	Single Intel® i7-3770 core, 3.4 GHz
Installed memory (RAM)	16 GB

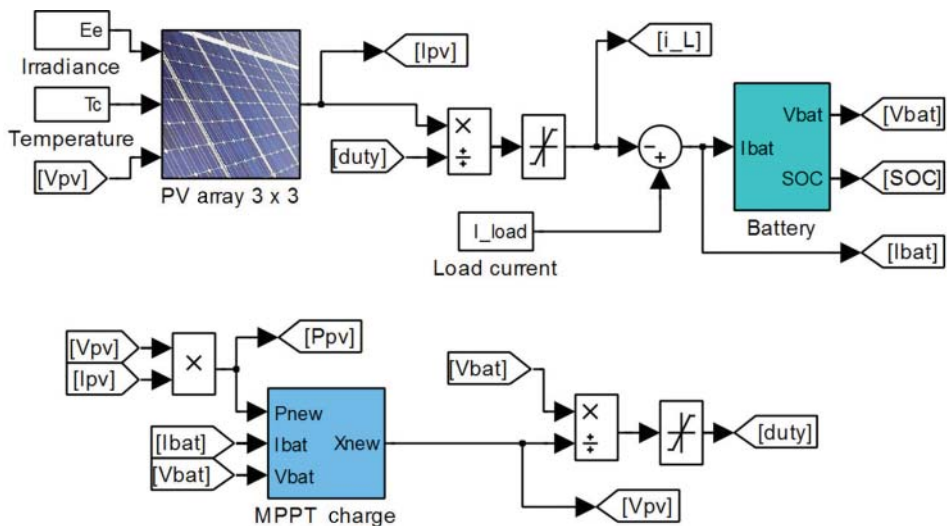


Figure 9.41 Configuration of standalone PV system with battery storage for long-term simulation.

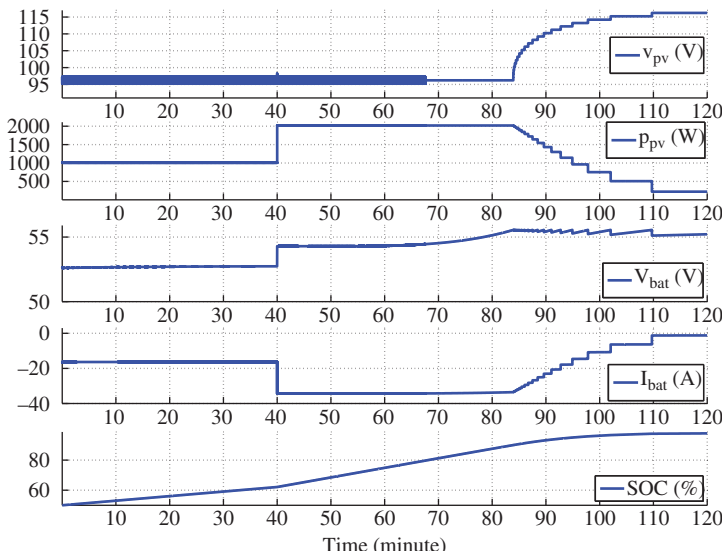
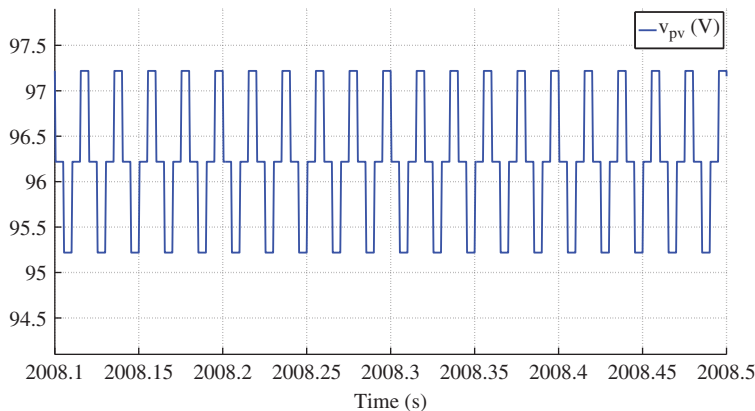
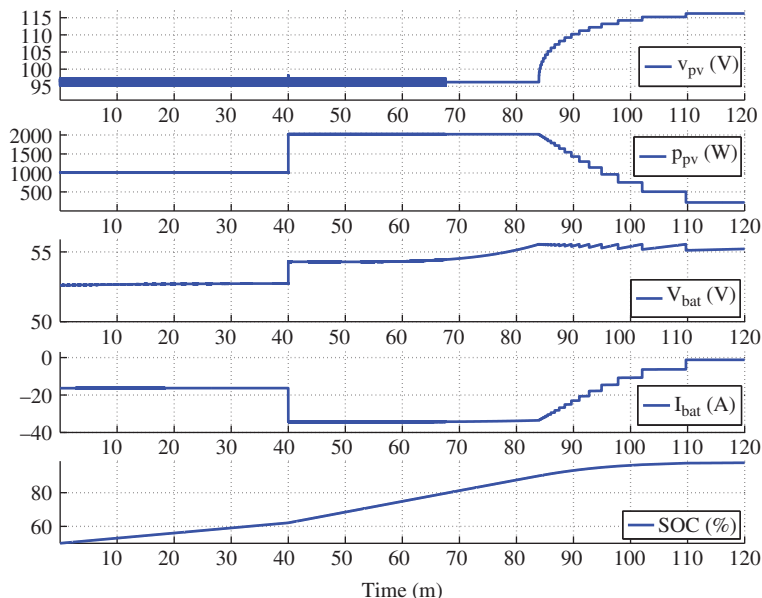


Figure 9.42 Simulated waveforms showing the two-hour operation.

is maintained at the same charge condition until the battery voltage reaches the upper level of 55.55 V. After 84 min, the charge controller takes action to increase the PV-link voltage from the MPP. The deviation of the MPP lowers the PV output power and the charge current, even though the PV array is potentially capable of reaching the higher power level. The battery voltage is regulated for continuous charging until the battery is fully charged, which can be sensed by a reduction of the battery charging current. PV generation is maintained to supply the load power consumption. Using the simplified model, the total simulation time is 7 min for two hours of system operation showing



**Figure 9.43** Simulated waveform of the PV-link voltage, illustrating the details of MPPT.



**Figure 9.44** Simulated waveforms for the two-hour operation.

the detailed operation of the MPPT algorithm and charging cycle regulation. Figure 9.43 shows a zoom-in on the waveform of the PV-link voltage,  $v_{pv}$ . It reveals the perturbation details around the MPP in the early stages due to the operation of the HC algorithm.

In the simulation model, as shown in Figure 9.41, the highest frequency is represented by the HC algorithm, which is in discrete-time format. In contrast to simulations to capture continuous signals, this allows the sampling frequency to be set at up to twice the frequency, which is 400 Hz. For the same two-hour period of operation discussed above, the simulation time is reduced to 63 s, rather than the 7 min in the previous study. The simulation result is shown in Figure 9.44, which is visually identical to the waveform in Figure 9.42, which reflects the cycle charge and MPPT operation.

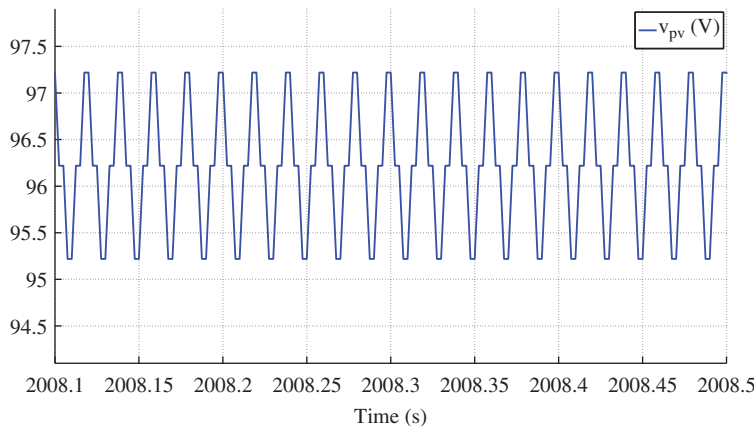


**Figure 9.45** Simulated waveform of the PV-link voltage illustrating the MPPT detail.

Figure 9.45 is a zoom-in on the waveform of the PV-link voltage,  $v_{pv}$ . It clearly shows the perturbation around the MPP due to the operation of the HC algorithm, but the details are not as accurate as the waveform in Figure 9.43. If the waveform details are not critical, the reduced sampling frequency can significantly improve the simulation efficiency for long-term simulation studies.

#### 9.6.5 Very-long-term Simulations

The proposed method is capable of simulating even longer-term operations with the simplified model and a reduced sampling frequency. When environmental data, such as irradiance and temperature, are available, the simulation can be used to predict the PV power system output in voltage and current terms. Using the same environmental data as the study by Xiao et al. (2013), the long-term simulation can be extended to eight-hour operation.

Figure 9.46 shows the simulated waveforms for the irradiance, cell temperature, PV-link voltage, battery voltage, PV output power, battery current, and battery SOC. It took 7.5 min to simulate the eight hours of system operation. The simulation result can be explained as follows:

- The irradiance increases from the early morning to its highest point in the middle of the day and decreases in the afternoon. The temperature also changes to its highest point at the middle of the day and decreases to lower level in the evening. The temperature variation affects the PV-link voltage representing the MPP, which is high at low temperatures and low at high temperatures. The solar irradiance significantly affects the PV output power.
- The initial SOC of the battery pack after the overnight discharge is 30%. The battery voltage is relatively low at the start point.
- MPPT operates at the beginning of the system control operation so as to inject the highest available power into the battery link. Ripples appear in the waveform of the PV-link voltage, indicating the active perturbation from the HC-based MPPT algorithm. The simulation shows that the system tracks the MPP at each moment and regulates the PV string voltage to follow the MPP.

- The control mode is switched to battery voltage regulation after the first 3.1 h of operation, until the battery voltage reaches the first upper limit of 54.45 V. The PV output and charge current continuously increase to respond to variations in solar irradiance.
- The system is maintained in the steady state for 15 min while the battery voltage is between 54.45 V and 55.55 V. The MPP of the PV array is no longer tracked during this period.
- Battery voltage regulation starts when the battery voltage reaches the upper limit of 55.55 V. The PV-link voltage is controlled to rise and deviate from the MPP. The PV output power and charge current are reduced by the deviation of the MPP, even though the PV array has the potential for higher power output.
- The regulation of the battery voltage is maintained for another 3 h until the solar irradiance drops to a low level in the late afternoon. The PV array output is regulated to maintain the load requirement and the float charge of the battery pack. The SOC is maintained at 100%.
- In the last hour of operation, the irradiance is close to zero. The battery is switched from charge to discharge mode. The load current is at the predefined value of 2.8 A. The battery voltage and SOC decrease accordingly. The operating mode will last until the next morning when solar radiation becomes available.

The simulation of the eight hours of operation shows the major drawback of stand-alone systems. The system is significantly oversized to accommodate bad weather conditions and low irradiation. However, solar energy is simply wasted on sunny days, as shown in this case study. The simulation result shows that the system takes the full power generation from the PV array for the first three hours. Then the control action curbs the PV power output in order to maintain constant voltage for the battery pack. Therefore, grid-connected systems represent a great advantage since the electrical network can usually absorb the PV power without limiting the generation.

## 9.7 Summary

Energy storage has high potential to mitigate the intermittent power generation of renewable resources. Several battery technologies were introduced at the beginning of this chapter, including those based on lead, nickel, lithium, and sodium–sulfur. The important terms for battery technologies were also introduced. Each technology has unique characteristics for practical applications. Therefore, the selection of the battery was briefly discussed.

Battery technology is still not ideal for widespread use since batteries can be expensive and have limited lifetimes, serious environmental problems, and safety concerns. Lead-acid batteries use sulfuric acid and lead, which are hazardous. Other materials used in batteries, such as nickel, lithium, cadmium, alkalis, and mercury can also contaminate soil and water. Furthermore, fire incidents involving both lithium-ion and NaS batteries raise safety concerns when these technologies are used in high-power-density batteries. Sensing and protection circuits should be carefully designed to guarantee the safe operation of battery power systems.

Battery mismatch and equalization were introduced due to their importance for reliable and long-lifetime operations. A new classification was presented in order to provide

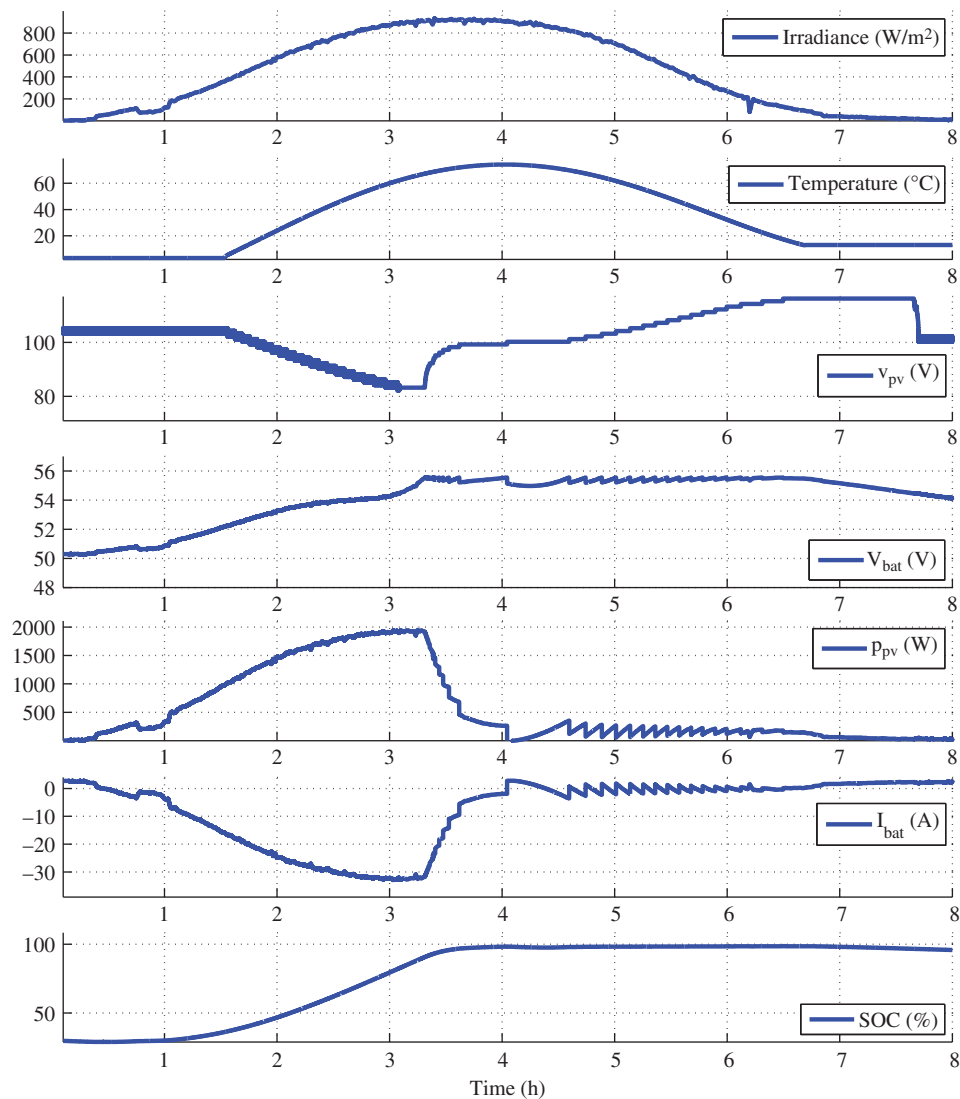


**Figure 9.46** Simulation of eight-hour operation of standalone system.

a clear framework for understanding existing methodologies for battery balancing. Even though the case study for equalization was demonstrated mainly at cell level, the same principles can be applied to balance battery modules.

In general, battery modeling is difficult since the parameters are nonlinear and time-variant with many factors, such as the SOC, temperature, age, and frequency. One important development in this chapter concerning battery characteristics and modeling is equivalent circuits at different complication levels. Practical simulation models with the flexibility to represent the battery voltage and the state of charge (SOC) and the option to represent self-discharge were described. Simulations based on Thévenin circuits were built in Simulink and demonstrated for practical implementation. A practical

NiMH battery pack was used to demonstrate the analysis, modeling, simulation, and verification.

The design process of standalone PV systems was discussed. Since most standalone systems contain battery storage, the integration of battery charging and MPPT is described. The algorithm is simple and easy to implement. The design cases for the standalone system with and without battery storage were introduced separately. The direct-coupled system without massive storage represents the simplest standalone PV system, but has significant disadvantages. The typical system is coupled with battery storage and power conditioning to mitigate the intermittent power generation and ensure a steady power supply overnight.

Hybrid system design is not covered, due to the complications for dedicated applications. The knowledge of battery and standalone systems that has been presented in this chapter is useful to design efficient, safe, and reliable hybrid systems.

The simulation of a standalone system is based on one practical design example. The Simulink models for the controller and power interface are developed at different levels for the simulation study: short term, medium term, long term, and very long term. The simulation objective should be always defined clearly to avoid complexity in modeling and inefficiency in simulation. It is always difficult to develop an efficient model, which can simulate not only the long-term changes, but also the transient details of fast dynamics. A simulation of eight hours of system operation shows MPPT, battery voltage regulation, and variation of SOC in response to changes in solar irradiance and cell temperature. The case study neglects the fast dynamics of the switching and PV voltage regulation. The dynamics at the battery link are also ignored for the very-long-term simulation. Without loss of generality, the simulation models are also presented to capture the fast dynamics, including fast switching in the DC/DC converter, but only for short-term simulations due to computational constraints.

## Problems

- 9.1** It is recommended to duplicate the simulation results presented in this chapter. The process is valuable in becoming familiar with the principles of system specification, design, component selection, simulation modeling, system protection, system integration, and verification.
- 9.2** Use any available simulation tool to construct a battery model based on the presented Thévenin circuits.
- 9.3** Find a practical battery module or cell to derive the model parameters.
- 9.4** Verify the simulation model output with the product data.
- 9.5** Design a PV–battery system for standalone applications.
  - a) Construct the simulation model to represent the system operation, including the blocks for the PV, battery, MPPT charge controller, and power interface.
  - b) Simulate the circuit over a short time, to reflect any transient responses that can be caused by sudden changes of load or solar irradiance.